

**INSTABILITIES, NUCLEATION, AND CRITICAL BEHAVIOR
IN NONEQUILIBRIUM DRIVEN FLUIDS**

THEORY AND SIMULATION



Institute 'Carlos I' for Theoretical and Computational Physics
and Depto. de Electromagnetismo y Física de la Materia
Universidad de Granada, Spain

**INSTABILITIES, NUCLEATION, AND CRITICAL BEHAVIOR
IN NONEQUILIBRIUM DRIVEN FLUIDS**

THEORY AND SIMULATION

MANUEL DÍEZ MINGUITO

email: mdiez@onsager.ugr.es

web: <http://cahn.ugr.es/~mdiez>

Advisor: Prof. Dr. Joaquín Marro

Ph.D. Thesis
Granada, September 2006

To Linda

[...] debemos nosotros tener correctamente
una explicación sobre los fenómenos celestes,
qué principio determina las trayectorias del sol y la luna
y qué fuerza rige a cada cosa en la tierra.

Lucrecio. *De rerum natura*.

Acknowledgments

Esta etapa de mi vida se cierra con dos nacimientos: en marzo, mi hija Cora y ahora, esta tesis. Mientras que las sensaciones que me produce el primero quedan en familia, debo expresar aquí mi agradecimiento a quienes han contribuido al segundo.

En primer lugar quiero agradecer a Joaquín Marro, mi profesor, tutor y mentor, todo el apoyo incondicional que me ofreció desde el principio, sabiendo siempre qué era lo mejor para mí en cada momento. A Pedro Garrido le agradezco todo el tiempo dedicado, su modo tan especial de motivar, las muchas dudas resueltas y las planteadas también, y su franqueza. Parte de este trabajo se la debo a la intuición de Paco de los Santos, mi compañero de despacho con el que he compartido muy buenos ratos y charlas sinceras y de cuyo humor inteligente he disfrutado. Asimismo agradezco a Miguel Ángel Muñoz, para mí un modelo a seguir, su interés, apoyo y consejo en momentos muy oportunos. Y al resto de los componentes del grupo de Física Estadística: Omar, mi compañero de viaje durante estos últimos cuatro años, siempre cordial, altruista y dispuesto, David Navidad, Jesús Cortés, Pablo Hurtado, Abdelfattah Achahbar, Antonio L. Lacomba, Joaquín Torres, Don Jesús Biel y Paco Ramos. Sin el ambiente de trabajo y camaradería presente en el grupo, sencillamente esta tesis no hubiera llegado a buen puerto.

Siento una especial gratitud tanto a nivel profesional como personal hacia Baruch Meerson. Aún me sorprenden su compromiso y dedicación, sus sinceros consejos, así como su cariño y cercanía, los cuales me ayudaron a creer en esta tesis y están más allá de todo elogio. Tampoco podré olvidar el excelente recibimiento que me brindaron él y su esposa en esa ciudad maravillosa que es Jerusalén.

Durante estos años he tenido dos buenos colaboradores en Thorsten Pöschel y Thomas Schwager, a los que les agradezco su interés y la doblemente buena acogida dispensada en Berlín.

Qué importantes han sido los amigos, siempre presentes, de los que hay poco que decir y mucho que agradecer. En este periplo he tenido la gran suerte de conocer a Juan Antonio, igualmente miembro del grupo. Con él he compartido innumerables charlas, preocupaciones, confidencias, confianza, amistad. Gracias. A mis ya viejos amigos: Fernando, que también sabe lo que es hacer una tesis luchando día a día a tocapiños, le debo su experiencia y su apoyo en momentos difíciles; a Miguel, para mí más que un amigo, por la ilusión y el tiempo

que juntos invertimos en tantos proyectos; a Jesús, por su ejemplar honradez y fidelidad, y al resto de los miembros del equipo.

A mis padres, que lo han dado todo por mí. A Gabi, Holger y Christoph, por su continuo interés y cariño.

A Cora, porque a pesar de haber demorado la redacción de este trabajo me ha alegrado la vida. Y finalmente a Linda, mi esposa y mi guía, a quien le dedico esta tesis. Gracias por todo, lo decible y lo indecible.

Granada, a 17 de Septiembre de 2006.

Contents

Acknowledgments	ix
1 General Introduction	1
1.1 Overview	7
Part I Driven Diffusive Fluids	11
2 Introduction	13
3 Lennard–Jones and Lattice models of driven fluids	19
3.1 Driven Lattice Gas	19
3.2 Driven Lennard-Jones fluid	22
3.3 Driven Lattice Gas with extended dynamics	24
3.3.1 Correlations and Structure Factor	24
3.3.2 Critical behavior	27
3.4 Conclusions	33
4 Anisotropic phenomena in nonequilibrium fluids	35
4.1 Motivation	35
4.2 The model	37
4.3 Main results	39
4.3.1 Phase segregation kinetics	39
4.3.2 Structure of the steady state	43
4.3.3 Transport properties	45
4.3.4 Coexistence curve	46
4.4 Conclusions	49
Part II Driven Granular Gases	53
5 Introduction	55

6	Phase separation of a driven granular gas in annular geometry	61
6.1	Introduction	62
6.2	Particles in an annulus and granular hydrostatics	63
6.2.1	The density equation	63
6.2.2	Annular state	65
6.2.3	Phase separation	67
6.3	Molecular Dynamics Simulations	70
6.3.1	Method	70
6.3.2	Steady States	71
6.3.3	Azimuthal Density Spectrum	73
6.4	Conclusions	76
7	Close-packed granular clusters	79
7.1	Introduction	79
7.2	Event-driven molecular dynamics simulations	80
7.3	Hydrostatic theory	82
7.4	Macro-particle fluctuations	88
7.5	Conclusions	89
	Part III Appendices	93
	A Equilibrium properties of the Lattice Gas	95
	B Interfacial stability of Driven Lattice Gases for $E \rightarrow \infty$	99
	C Mesoscopic equation for the DLG with extended dynamics	105
	D Hydrodynamics for three-dimensional granular gases	109
	Part IV Conclusions	115
	Conclusions and future work	117
	Published work	125
	Bibliography	127
	Resumen en Español	139

List of Figures

1.1	Complexity of the macroscopic behavior	3
2.1	Typical configurations in the stationary regime of the DLG for a 128×128 half-filled lattice	14
3.1	Typical steady state configurations of the DLJF subject to a horizontal field	21
3.2	Schematic phase diagrams for the DLG, NDLG, and DLJF	23
3.3	Triangular anisotropies observed at early times of the DLG and DLJF	24
3.4	Schematic comparison of the sites a particle may occupy for nearest-neighbor and next-nearest-neighbor hops	25
3.5	Surface plots of the two-point correlations and structure factor above criticality for the DLG with NN and NNN couplings	25
3.6	Parallel and transverse components of the two-point correlation function above criticality for the DLG with NN and NNN interactions	26
3.7	Parallel and transverse components of the structure factor above criticality for the DLG with NN and NNN interactions	27
3.8	Log-log plot of the rescaled order parameter m for different sizes	29
3.9	Log-log plot of the rescaled susceptibility χ for different sizes	29
3.10	Scaling plot of the rescaled fourth Binder cumulant b for different sizes	30
4.1	Off-lattice models in the realm of computer simulation of fluids	36
4.2	Schematic representation of the region which is accessible to a given particle as a consequence of a trial move	38
4.3	Typical steady-state configurations for equilibrium ($E = 0$) and large field limit ($E \rightarrow \infty$)	40
4.4	Typical configurations for $E = 0$ and $E \rightarrow \infty$ as time proceeds during relaxation from a disordered state	41
4.5	Time evolution of the enthalpy or excess of energy per particle for different temperatures	42
4.6	Details of the structure in the low- T , solid phase	43

4.7	Degree of anisotropy (main graph), radial (lower inset) and azimuthal (upper inset) distribution functions	44
4.8	Transverse-to-the-field current profiles below criticality: comparison between lattice and off-lattice models	46
4.9	Temperature dependence of the mean energy and normalized net current for large field limit	47
4.10	Density profiles transverse to the field for different temperatures	47
4.11	Liquid-vapor coexistence curve and the associated critical indexes obtained from the density profiles	49
6.1	The normalized density profiles obtained from simulations and hydrostatics	66
6.2	Main Graph: The marginal stability curves $k = k(f)$ at fixed aspect ratios Ω for different values of the heat loss parameter Λ . Inset: The dependence of k_{\max} on $\Lambda^{1/2}$	67
6.3	Two-dimensional projections of the phase diagram: Marginal stability and negative compressibility curves	68
6.4	The scaled steady state granular pressure P versus the grain area fraction f at fixed Ω , and the spinodal interval	70
6.5	Typical steady state snapshots	71
6.6	Typical steady state snapshots and the temporal evolution of the COM and of the squared amplitude of the fundamental Fourier mode	72
6.7	The normalized probability distribution functions at a different number of particles	74
6.8	The Ω - f phase diagram for $\Lambda = 81.09$ obtained from molecular dynamics simulations and hydrodynamics	76
6.9	The marginal stability lines for our main setting and for an alternative setting	77
7.1	Snapshots and magnifications of the close-packed cluster	81
7.2	Scaled density n/n_c : Comparison between hydrostatics and event-driven simulations	84
7.3	Maximum scaled density n_{\max}/n_c : Comparison between hydrostatics and event-driven simulations	86
7.4	Marginal stability curve (main graph) and eigenfunctions associated to the linear eigenvalue problem (inset)	87
7.5	Probability distribution functions of the center of mass of the macro-particle	88
7.6	Scaled standard deviation of the center of mass position	90
A.1	Spontaneous magnetization and order parameter critical exponent for the Ising model with NN and NNN couplings	96
A.2	Surface plots of the two-point correlations and structure factor above criticality for the equilibrium lattice gas with NN and NNN interactions	97

A.3	Projections of the two-point correlations and structure factor above criticality for the equilibrium lattice gas	98
B.1	Schematic diagram of the accessible sites for a particle in the α DLG model	101
B.2	The α -dependence of the order parameter m in the α DLG	102
B.3	Order parameter critical exponent for the second order phase transition which occurs in the α DLG	103
D.1	Perspective sketch of the three-dimensional experimental <i>set-up</i>	110
D.2	Scaled temperature and density profiles as predicted by granular hydrostatic theory in three dimensions	112
D.3	Marginal stability curve $m = m(f)$ (main graph) and eigenfunctions $\Gamma_m(\mathbf{r})$ (inset)	113
D.4	Complejidad del comportamiento macroscópico	141

List of Tables

4.1	Critical parameters	48
6.1	The averaged squared relative amplitudes $\langle A_k^2(t) \rangle / \alpha_0^2$ for the first three modes $k = 1, 2$ and 3	75

Chapter 1

General Introduction

Nature has a hierarchical structure, with time, length, and energy scales ranging from the *microscopic* to the *macroscopic*. Surprisingly, it is often possible to discuss these levels independently, e.g., in the case of molecular fluids. The macroscopic level, i.e. the world directly perceived at our human senses, is described hydrodynamically. That is, by *continuous* (or piecewise continuous) functions of the spatial coordinates \mathbf{r} and time t (hydrodynamic *fields*). As a result, the great disciplines of macroscopic physics, such as fluid mechanics, elasticity, acoustics, electromagnetism, are field theories. These fields are determined by integro-differential equations involving unknown functions of \mathbf{r} and t . The microscopic level is described as a collection of a very large number of constituents, such as atoms, molecules, or other more complex entities interacting with each other through well-defined electro-mechanical forces¹. Their evolution with time is provided by the laws of quantum mechanics, but in many cases classical mechanics results a good approximation.

If there is a clear scale separation between microscopic and macroscopic, then an intermediate scale can be introduced. Such a level of description is referred to as the *mesoscopic* level. It is a coarse-grained representation to capture the physics of microscopic models on the large length and time scales, which is described by stochastic partial differential equations [1, 2]. By concreteness, the *mesoscopic* description of the system in question, whose dynamics is on the average governed by the laws of macroscopic time evolution, is a result of building up of microscopic fluctuations. This approach aims at understanding the slowly-varying long wavelength, low frequency properties of many-body systems and form the basis of the field theoretical analyses of critical phenomena. In the literature it is common include in this intermediate scale the kinetic description of gases, e.g., Boltzmann equation. Thus, this level is also referred to as the

¹The difference between *microscopic* and *macroscopic* levels is essentially relative. The key concept here is the large number of constituents, not their small size. For instance, a galaxy (macroscopic) is a *object* composed by a large number of stars (microscopic), a colony of organisms is a large set of individuals, a gas comprised by a large number of molecules, etc.

kinetic level². This is in fact a reduced microscopic level, described by one-particle coarse-grained distribution functions and the asymptotic, irreversible kinetic equations.

The three different levels of description³ are, in principle, equivalent approaches of the same reality. Nevertheless, the form of the laws derived at these three levels are so different from each other that there soon appeared a stringent need for an explanation of hydrodynamics in terms of the microscopic evolution of the underlying collection of constituents. The bridges between them are provided by *Statistical Mechanics*. Statistical mechanics aims to derive macroscopic behavior of matter originated in the cooperative behavior of interacting (microscopic) individual entities. Some of the phenomena are simple synergetic effects of the actions of individuals, e.g., the pressure exerted by a molecular gas on the walls of its container and thousands of fireflies flashing in synchrony; while others are paradigms of emergent behavior, having no direct counterpart in the properties or dynamics of individual constituents, e.g., the transition from laminar to turbulent flows in fluids and the one million of atoms which give rise to the program of life: the deoxyribonucleic acid or DNA for short. In the latter cases, the behavior of the constituents become singular, but very different from what they would exhibit in the absence of the others.

The most successful achievement of statistical mechanics is *Ensemble Theory* [3], which yields the connection between the macroscopic properties of *equilibrium* systems from the laws governing the microscopic interactions of the individual particles. It is said that a certain system stay at equilibrium when it is isolated, shows no hysteresis, and reaches a steady state (all its macroscopic properties are fixed) [4]. In that case, the macroscopic properties are expressed in terms of *thermodynamic* variables. Indeed, the *thermodynamics* is in this sense a kind of hydrodynamic description, which consists only of laws and relations between thermodynamic quantities. From the mathematical point of view, ensemble theory can be completely axiomatized. This provides us, at least in principle, analytic expressions for these thermodynamic quantities allowing us to derive all the relevant macroscopic information of the thermal system in question⁴, e.g., the free energy, equation of state, etc.

In nature, by contrast, equilibrium systems are an exception (even an idealization) rather than the rule: *non-equilibrium* phenomena are overwhelmingly more abundant. Galaxies, human beings, chemical reactions, geophysical flows, carriers in semiconductor devices, financial stock markets, ratchet-effect transport, traffic flow on a highway, to cite just a few, are (many-body) systems

²Formally, both stochastic differential equations and kinetic equations may belong to the same level, although they involve different (mesoscopic) length and time scales.

³There may be larger scale structures (e.g., the Karman vortex train) produced by a large scale fluid dynamics, but we do not pay attention to such large scales.

⁴Once the microscopic Hamiltonian (say \mathcal{H}) of the system is specified the “canonical” stationary probability distribution \mathcal{P} is known in terms of the Boltzmann factor $\mathcal{P} = e^{-\mathcal{H}/k_B T}/Z$, where Z is the partition function, k_B is the Boltzmann’s constant, and T the temperature. Thus, averages over such a distribution of time-independent observables can be computed. The remaining difficulties are merely technical.



Figure 1.1: Complexity arises at all levels. Some amazing examples are the following. Upper left: river networks in Yemen (source NASA). Upper right: aeolian patterns in Colorado, USA (photo by Bob Bauer). Lower left: tornado as a rotating geophysical flow. Lower right: *oscillons* in a colloidal suspension[5].

under nonequilibrium conditions⁵. Out-of-equilibrium systems are characterized by not being closed, i.e., by having an exchange of energy, particles, and/or information with their environment. In general, the state of a nonequilibrium system is not determined solely by external constraints, but also depends upon its history (hysteretic systems). Consequently, this gives rise to the enormous complexity of our world which occurs to all levels of description [6] and manifests in pattern formation, absorbing states, self-organization, chaos, ageing, avalanches, morphogenesis, oscillations, fractals, etc [7, 8, 9, 10]. All these amazing and complicated phenomena are associated to *instabilities*⁶, which are variously described as nonequilibrium phase transitions [7, 11, 12, 13], bifurcations or synergetics, with the aim of connecting microscopics with the coherent structures observed.

However, most of studies of nonequilibrium systems adopt a macroscopic (phenomenological) point of view. In fact, little is known in general on why are there such an interesting structures or how this complexity arises from interac-

⁵Nonequilibrium phenomena are also encountered whenever systems are relaxing towards an equilibrium steady state. Nevertheless, in most of cases these can be understood in terms of equilibrium concepts.

⁶Nonequilibrium instabilities are attended by ordering phenomena analogous to those of equilibrium statistical mechanics; one may therefore refer to *nonequilibrium phase transitions* [11]. Although nonequilibrium phase transitions represent a more varied picture than their equilibrium counterparts.

tion at a microscopic level. Consequently, no theory exists and the development of a solid theoretical background is nowadays in an early stage compared with equilibrium, where the ensemble theory holds successfully. As a matter of fact, the key point of difference between equilibrium and nonequilibrium statistical mechanics is that whereas in the former case the stationary probability distribution is known, out of equilibrium one must find the time-dependent distribution, which obey a general evolution equation, i.e., a *master equation*. In most of solvable cases—which in fact are just a few—, this can be done only approximately. One can only provide some unified view when the systems are *not too far*⁷ from equilibrium [14], where the system can be treated perturbatively around the equilibrium state and studied using linear response theory. Nevertheless, our attention here lies at systems far from equilibrium where such schemes break down.

Within the framework given above, the main subject of this thesis rests on the study—at different levels of description—of instabilities in systems which are driven, i.e., maintained far from equilibrium by an external forcing. We focus here on two main classes, namely, driven–diffusive fluids and driven granular gases.

The first family (*driven–diffusive fluids*⁸) corresponds to systems which are⁹ coupled to two reservoirs of energy in such a way that there is a steady energy flow through the system. Clearly, this definition comprises a bunch of very varied systems. We restrict ourselves to systems in which a (non-zero) current of particles (whose number is a conserved quantity) is set up through the system, there is spatial anisotropies associated with an external driving field, and eventually a nonequilibrium steady state is reached. The simplest example seems to be a resistor gaining energy from a battery and losing it to the atmosphere. But even for this reduced class of systems the stationary probability distribution is unknown.

The basic motivation behind the introduction of *driven–diffusive fluids* corresponds to a need of unravel the key ingredients of nonequilibrium behavior. A reasonable approach consist in investigating systems as simple as possible, which aim for capture the microscopic essentials yielding to the complicate, macroscopic nonequilibrium ordering. These microscopic models are usually oversimplified representations of real systems, and consider entities as particles interacting via simple rules. Between them, *lattice* models—which are based in discretization of space into lattice sites— have played a important role due to the fact that they sometimes allow for exact results, and allow one to isolate the

⁷Nevertheless, a precise definition of *not too far* is rather difficult to give; the borderline is rather unclear.

⁸We should mention here that in the literature these systems are commonly referred as driven–diffusive *systems* instead of driven–diffusive *fluids*, which is adopted in this thesis. As we shall describe in some detail in Chapter 3, we reserve the former denomination for a mean–field mesoscopic description.

⁹Following Schmittmann & Zia in Ref. [15].

specific features of a system. In addition, lattice models allow us to obtain the intuition one needs in order to develop the appropriate theoretical tools and, from an experimental point of view, are easier to be implemented in a computer. Such an approach has given rise to a lively research activity in the last decade [11, 15, 16, 17, 18, 19, 20] and a bunch of emerging techniques may now be applied to lattice systems, including nonequilibrium statistical *field theory*. A general amazing result from these studies is that lattice models often capture some essentials of social organisms [21, 22, 23], formation of river networks [24], epidemics [25], glasses, electrical circuits, traffic [26, 27], hydrodynamics, colloids and foams, enzyme biology [28], living organisms [29], and markets [30], for example. In particular, lattice models have succeeded in understanding (equilibrium) phase transitions and critical phenomena [16, 31, 32] due, in many aspects, to renormalization group methods [33, 34].

The central result in (equilibrium) critical phenomena is *universality*, i.e., the behavior of disparate systems in the vicinity of critical points are determined solely by basic features —dimensionality, range of forces, symmetries, etc.— and does not seem to depend to any great extent on the particular system [33, 35, 36]. One can therefore hope to assign all systems to classes each of them being identified by a set of critical indices (exponents and some amplitude ratios). How much of these concepts apply to nonequilibrium phase transitions are only just emerging, and one expects lattice models to be equally important here. These issues are considered in Chapter 3, in which a particular driven-diffusive lattice model, prototype for nonequilibrium phase transitions, is investigated. However, a well-known disadvantage of lattice models is that when they are compared directly with experiment result too crude. This has to be understood in the sense that they often do not account for important features of the corresponding nonequilibrium phase diagram, such as structural, morphological, and even critical properties. Furthermore, theoreticians often tend to consider them as prototypical models for certain behavior, a fact which is in many cases not justified. This will be discussed in Chapter 4, where we introduce a novel, *realistic* model for computer simulation of anisotropic fluids.

The second class of systems we consider in this thesis concerns *driven granular gases*. A granular material is a large conglomerate of discrete macroscopic¹⁰ (classical) particles. Examples, which occur at very different length scales, may range from powders to intergalactic dust clouds; they include sand, concrete, rice, volcanic flows, Saturn ring's, and many others (for a review, see [37]). They have important applications in industrial sectors as pharmaceutical, construction and civil engineering, chemical, food and agricultural, etc. On a larger scale, they are also relevant in understanding many geological and astrophysical processes. In addition, they are closely related to a broader class of systems, such as foams, colloids and glasses. The collective behavior of an assembly of granular particles exhibits an impressive variety of phenomena¹¹ which include

¹⁰In the sense that they are directly perceived at our human eyes.

¹¹The size range of phenomena goes from $\approx 10^{-6}$ m in powders, to $\approx 10^3$ m in deserts, up

a plethora of pattern forming instabilities [38, 39, 40, 41], clustering [42, 43, 44], flows and jamming in hoppers [45], avalanches and slides [46], mixing and segregation [47], convection and heaping [48, 49], eruptions [50, 51], to cite just a few. Clearly, their relevancy is beyond any doubt, and understanding their properties is not only an urgent industrial need, but also an important challenge for physicists.

Since grains have a macroscopic size, friction and restitutional losses from collisions give rise to dissipative interactions —kinetic energy is continually transferred into heat—. Although the dominant interactions depend on particle size. The relevant energy scale for a typical, say, rice grain of length $l \approx 5\text{mm}$ and mass m is its potential energy mgl , where g is the gravitational acceleration. For much smaller grain sizes other kind of interactions may become important¹². Hence, in granular materials the thermal energy $k_B T$ is irrelevant, i.e. $k_B T \ll mgl$. This implies that dynamical effects outweigh entropy considerations [37] and, therefore, neither equilibrium statistical–mechanics nor thermodynamics arguments are useful. Furthermore, due to the fact that granulates are comprised by a finite number of particles¹³ usually there is a strong effect of fluctuations and, therefore, statistics may be dominated by *rare events*. Other important effects involve the interstitial fluid, e.g. air or water, although in many situations one can ignore it with confidence and consider the grain–grain interactions alone. In this thesis (specifically in Part II) we will restrict ourselves to *dry* granular systems, where the interaction between particles take place mainly via contact forces.

However, in spite of the simple (classical) features which characterize them, granular materials behave in a rather unconventional way: their phases —solid, liquid, and gas— have complex–collective properties that distinguish them from molecular fluids and solids. As a result, their statistics and dynamics are poorly understood. In fact, from a theoretical point of view, these systems are still only understood in terms of predictions of a general nature and many open questions remain. Linear elasticity does not apply for granular *solids*, which are highly hysteretic, show static stress indeterminacy, and possess static yield shear stress. The interlocking of grains leads to force chains, jamming, dilation on shearing, etc. *Liquids* are viscous, show avalanches (possess a critical slope), size segregation in mixtures, shear bands (narrow regions separating blocks moving with different velocities), pattern formation. *Gases*, which can only persist with continuous energy supply, are highly compressible, show clustering, long range correlations, inelastic collapse in computational models, non-maxwellian distribution functions, pattern formation, and lack of scale separation between macroscopic scales and microscopic ones. All of this phenomenology makes difficult to cast them in the framework of the classical three different phases of

to $\approx 10^{20}$ m in planetary rings.

¹²For instance, it may occur charging and surface coating for $d \approx 0.1$, or magnetization and surface adhesion for $d \approx 0.01$.

¹³In contrast with molecular systems $N \ll N_A$, where N_A is the Avogadro number. Nevertheless, in certain cases a few thousands or even hundreds of particles are enough to allow for statistical approaches.

matter. Some of the interesting open issues and controversies that we address in Chapters 6 and 7 are: What are the statistical properties of granular systems, how do granular phase changes occur, and what are the optimum continuum models and when do they apply. In particular, we focus on the continuum description of clustering, symmetry breaking, and phase separation instabilities in granular gases. As we shall see, these instabilities provide sensitive tests to models of granular flows and contribute to the understanding of pattern formation far from equilibrium.

1.1 Overview

We investigate in this thesis the two aforementioned classes of systems, which have become of paramount importance in the last years. The study is divided into four parts. The Part I, which comprises Chapters 2, 3 and 4, is devoted to *driven-diffusive fluids*. Part II deals with *driven granular gases*, and consists of Chapters 5, 6 and 7. Part III includes the Appendix A, B, C, and D. Finally, we close (Part IV) with a detailed summary and the main conclusions.

The first part begin in **Chapter 2** by introducing the *driven lattice gas* — prototype for nonequilibrium anisotropic phase transitions—. This model may be viewed as an oversimplification of certain traffic and flow problems. The particles interact via a local anisotropic rule, which induces a preferential hopping along one direction, so that a net current sets in if allowed by boundary conditions. We discuss some of its already known properties and controversies. We shall describe in greater detail the computational and field-theoretical methods employed in Chapters 3 and 4.

One of the most important questions we can ask about any model is whether the behavior that it displays is universal. In **Chapter 3** we address this question and study the phase segregation process in the prototypical lattice (microscopic) model introduced in Chapter 2. The emphasis in our study is on the influence of dynamic details on the resulting (non-equilibrium) steady state, although we also pay some attention to kinetic aspects. In particular, we shall discuss on the similarities and differences between the *driven lattice gas* and related lattice and off-lattice models, from a simulational and theoretical point of view. The comparison between them allows us to discuss some exceptional, hardly realistic features of the original *driven lattice gas*. In addition, we test the validity of the two competing mesoscopic (Langevin-type) approaches on describing the critical behavior of these models.

We introduce in **Chapter 4** a novel, *realistic* off-lattice driven fluid for anisotropic behavior. We describe short-time kinetic and steady-state properties of the non-equilibrium phases, namely, solid, liquid and gas anisotropic phases. This is a computationally-convenient model which exhibits a net current and striped structures at low temperature, thus resembling many situations

in nature. We here focus on both critical behavior and some details of the nucleation process. Concerning the critical behavior, we discuss on the role of symmetries on computer and field-theoretical modeling of non-equilibrium fluids. In addition, some important comparisons with experiments are drawn.

Chapter 5 serves as an introduction to Part II, which is devoted to driven granular gases. We briefly outline the current situation with regard to research on granular gases. In particular, we discuss on the applicability of a hydrodynamic theory to granular flows. We also present the basic ingredients of the studied models and the computer simulation methods.

In **Chapter 6** we address phase separation instability of a monodisperse gas of inelastically colliding hard disks confined in a two-dimensional annulus, the inner circle of which represents a “thermal wall”. Our main objectives are to characterize the instability and compute the phase diagram by using granular hydrodynamics—we employed for hydrodynamics Enskog-type constitutive relations, which are derived from first principles—and event driven molecular dynamics simulations. We also discuss on clustering and symmetry-breaking instabilities. By focusing on the annular geometry, we hope to motivate experimental studies of the granular phase separation which may be advantageous in this geometry.

This **Chapter 7** addresses granular hydrodynamics and fluctuations in a simple two-dimensional granular system under conditions when existing hydrodynamic descriptions break down because of large density, *not* large inelasticity. We study a model system of inelastically colliding hard disks inside a circular box, driven by a thermal wall in which a dense granular cluster behave like a *macro-particle*. Some features of the macro-particle are well described by the stationary solution of granular hydrostatic equations by using phenomenological constitutive relations. Hydrostatic predictions are tested by comparing with molecular dynamics simulations. We are able to develop an effective Langevin description for the macro-particle, confined by a harmonic potential and driven by a delta-correlated noise. We are also concerned about whether the crystal structure depends on the geometry.

The Part III is comprised by four appendices: **Appendix A** is devoted to the most important properties of the *Lattice Gas*¹⁴, which is the equilibrium counterpart of the *driven lattice gas* studied in Chapter 3; in **Appendix B** we introduce a model which aim at characterizing the stability of the interface in driven lattice models; **Appendix C** details some field theoretical derivations performed in Chapter 3 concerning Langevin-type equations; and in **Appendix D** we propose a set of constitutive relations for the hydrostatic description of three-dimensional granular gases.

¹⁴The *lattice gas* is the conserved version of the Ising model [32, 52]. As a result, they are isomorphic.

Finally, after the appendices, we present in Part IV our main conclusions, summing up our original contributions and pointing out the future work that should be addressed. We also enclose the list of publications associated to the work developed along this thesis.

Part I

Driven Diffusive Fluids

Chapter 2

Introduction

As outlined in the general introduction (Chapter 1), the first part of this thesis is devoted to the study of nonequilibrium phase transitions in *Driven Diffusive Fluids*. This is a broad class of nonequilibrium systems which are characterized to be coupled to two reservoirs of energy. The one injects energy continuously whereas the other subtracts it in such a way that a nonequilibrium steady state is reached asymptotically. Studies of these systems have generally focused on lattice systems, i.e., simplified models based on a discretization of space and in considering interacting particles that move according to simple local rules. This is because a general formalism analogous to equilibrium statistical mechanics is lacking even for nonequilibrium steady states. The way to overcome this drawback is to develop and study simple models —while retaining the essence of the difficulties of nonequilibrium states— capable to capture the essential behavior.

Within this context, one of most relevant models is the one devised by Katz, Lebowitz and Spohn¹ [53]. Motivated by both the theoretical interest in nonequilibrium steady states and the physics of fast ionic conductors [11], they introduced a minor modification to a well-known system in equilibrium statistical mechanics: the Ising model [32, 52]. It consists of particles —instead of spins— diffusing on a lattice, subject to an excluded volume constraint and an attractive nearest neighbor interaction. The particles, whose total number remains conserved, are driven by an external (constant) field E , settled on a thermal bath at temperature T . We shall refer henceforth to this model as the *Driven Lattice Gas* (DLG) [11, 15]. The dynamics in the DLG is according to Metropolis [54] transition probabilities per unit time. Consequently, for periodic boundary conditions (and for any non-zero driving field), the result is a net current of particles that generates heat which is absorbed by the thermal bath. As E is increased, the system reaches saturation, i.e., particles cannot jump against the field. Eventually, anisotropic phase segregation occurs in the DLG for low enough bath temperatures: a striped liquid (rich particle) phase,

¹Sometimes is referred to as the KLS model, after the initials of its inventors.

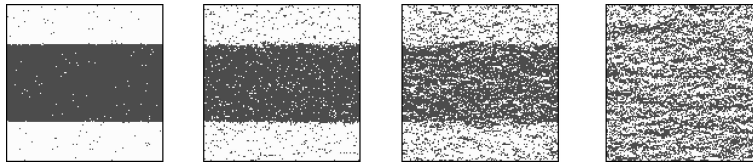


Figure 2.1: Typical configurations in the stationary regime of the DLG for a 128×128 half-filled ($\rho = 1/2$) lattice and (from left to right) $T = 0.70$, $T = 0.95$, $T = 1.30$, and $T = 1.50$. The temperatures are rescaled according with the equilibrium lattice gas critical temperature (see Appendix A): $T_{\text{Ons}} = 2.269$ in energy units. The value of the field is $E = 1000$, which is effectively infinite at all temperatures.

which coexists with its vapor (poor particle) phase, percolates along the field direction. However, for high enough temperatures a disordered phase appears, characterized by a gas-like state. As a matter of fact, for two dimensional half-filled lattices the DLG undergoes a second-order phase transition; otherwise the transition is of first-order. Its phase behavior is best illustrated by ‘snapshots’ of typical configurations generated by *Monte Carlo* (MC) simulations [55], as in Fig. 2.1.

In spite of a deceptively simple definition, the steady states observed exhibit a rich and counterintuitive behavior, with many interesting features such as the violation of the fluctuation-dissipation theorem, a singular structure factor, and slow decay of spatial correlations. But perhaps its most striking, counterintuitive feature is that a strong field raises the critical temperature above the equilibrium lattice gas² critical temperature. We shall discuss these features in greater detail in Chapters 3 and 4. The DLG has been also useful to model, for instance, ionic currents [11, 56], traffic and pedestrians flows [57, 58], water-in-oil microemulsions [59], electrophoresis experiments [60], etc (see Ref. [15] and references therein.) Moreover, the highly anisotropic configurations exhibited by the DLG resembles actual driven systems. Many natural systems exhibit spatial striped patterns on macroscopic scales [7, 12]. These are often caused by transport of matter or charge induced by a drive which leads to heterogeneous ordering. Such phenomenology occurs during segregation in driven sheared systems [61, 62, 63], in flowing fluids [64], and during phase separation in colloidal [65], granular [66, 67], and liquid-liquid [68] mixtures. Further examples are ripples shaped by the wind in sand deserts [69, 70], the lanes and trails formed by living organisms (animals and/or pedestrians) and vehicle traffic [27, 29], and the anisotropies observed in high temperature superconductors [71, 72] and in two-dimensional electron gases [73, 74].

As a result, this model system became the theoreticians’ prototype for anisotropic behavior, and is nowadays the most thoroughly studied system showing an anisotropic nonequilibrium phase transition.

²See Appendix A for a quick review of the lattice gas properties.

In Chapters 3 and 4 we report on novel findings on this and other related models by describing different realizations observed in (Metropolis) MC simulations. In particular, we study to what extent the DLG features are universal, or in other words, how robust is its behavior. The clue is that the DLG is, in a sense, pathological. We also devise a novel driven fluid for anisotropic phenomena, which we believe is not only of theoretical importance, but also relevant for experimentalists. In addition to MC techniques, field-theoretical Langevin-type approaches on the DLG are also developed. But before deep further on these matters, we shall describe in greater detail the computational and field-theoretical methods employed in these chapters.

In statistical mechanics, *Monte Carlo*³ simulations [55] play a major role on the study of phase transitions and critical phenomena. Any MC algorithm generates stochastic trajectories in the system's phase space, in such a way that the properties of the system are derived from averages over the different trajectories. To be specific, for systems both in and far from equilibrium, MC simulations involve long sequences of configurations, which evolve from one \mathbf{c} to another \mathbf{c}' according to a defined transition probability per unit time (*rate*), namely, $w(\mathbf{c} \rightarrow \mathbf{c}')$. Once initial transients have decayed stationary observables can be computed as configurational averages. For systems under equilibrium conditions, such an average over configurations is referred to as the *ensemble* average. In such a case, and if the *ergodic hypothesis* [3] is assumed, ensemble averages are equivalent to time averages⁴.

The acceptance rules for transitions between configurations are chosen such that these configurations occur with a frequency prescribed by the desired probability distribution. For equilibrium systems, this must be the “canonical” stationary Gibbs distribution $\mathcal{P}_0 = e^{-\mathcal{H}/k_B T}/Z$, where \mathcal{H} is the Hamiltonian, Z is the partition function, k_B is the Boltzmann's constant, and T the temperature. Since our interest here is in nonequilibrium behavior, we will need to specify how a given configuration \mathbf{c} evolves into a new one, \mathbf{c}' , that is, $w(\mathbf{c} \rightarrow \mathbf{c}')$. As a consequence, we must deal with a time-dependent probability distribution function $\mathcal{P}(\mathbf{c}, t)$, which obeys a *master equation* [1, 2]

$$\partial_t \mathcal{P}(\mathbf{c}, t) = \sum_{\mathbf{c}'} \{ \mathcal{P}(\mathbf{c}', t) w(\mathbf{c}' \rightarrow \mathbf{c}) - \mathcal{P}(\mathbf{c}, t) w(\mathbf{c} \rightarrow \mathbf{c}') \}. \quad (2.1)$$

Its stationary solution, $\mathcal{P}(\mathbf{c})$, controls all the time-independent properties. To ensure that the desired equilibrium distribution \mathcal{P}_0 is reproduced, one chooses

³More precisely, one should refer it as the *Monte Carlo importance sampling* algorithm [54, 55]. The nickname “Monte Carlo” comes from the fact that this technique entails a large sequence of random numbers.

⁴In fact, if MC simulations mimic configurational averages, Molecular Dynamics is a scheme for studying the natural time evolution (time averages) of a certain system. For thermalized (or equilibrated) systems differences between both techniques should disappear in the *thermodynamic limit*. Chapters 6 and 7 deal with Molecular Dynamic simulations, which are briefly described in Chapter 5.

rates which satisfy the *detailed balance* condition, namely

$$\frac{w(\mathbf{c}' \rightarrow \mathbf{c})}{w(\mathbf{c} \rightarrow \mathbf{c}')} = \frac{\mathcal{P}_0(\mathbf{c})}{\mathcal{P}_0(\mathbf{c}')} . \quad (2.2)$$

This ensures that the bracket in Eq. (2.1) vanishes. The important point here is that the ratio $\mathcal{P}_0(\mathbf{c})/\mathcal{P}_0(\mathbf{c}') = e^{-\Delta\mathcal{H}/k_B T}$, where $\Delta\mathcal{H} = \mathcal{H}(\mathbf{c}') - \mathcal{H}(\mathbf{c})$. One may thus choose rates of the form $w(\mathbf{c} \rightarrow \mathbf{c}') = f(\Delta\mathcal{H}/k_B T)$, with an appropriate f satisfying

$$f(-x)/f(x) = e^x . \quad (2.3)$$

Some choices for f are the Kawasaki rate $f(x) = 2(1 + e^x)^{-1}$ [75], the van Beijeren & Schulman rate $f(x) = e^{-x/2}$ [76], and the Metropolis rate $f(x) = \min\{1, e^{-x}\}$ [54]. All of our simulations in Part I concern the Metropolis rate.

The most simple way of driving a system (as in the DLG case) into a nonequilibrium steady state is to impose rates that violates detailed balance. A straightforward extension of $\Delta\mathcal{H} = \mathcal{H}(\mathbf{c}') - \mathcal{H}(\mathbf{c})$ in Eq (2.2) is to include the work done by the field, i.e., to define the total energy difference of the for $\Delta\mathcal{H} + E\mathbf{x}$, with \mathbf{x} the particle displacement in the field direction. This rate with the property Eq. (2.3) satisfies the detailed balance condition *locally* but not globally so that microscopic reversibility of the process as in equilibrium is not guaranteed. This scheme is adopted in the DLG which (together with toroidal boundary conditions) yields the system towards a nonequilibrium steady state.

It is worth notice that there are recent computational *coarse-grained* methods, e.g., *Dissipative Particle Dynamics* (DPD) and *Brownian Dynamics* (BD) (see for instance [77]), for fluid dynamics which may have several advantages over conventional computational dynamics methods. The DPD method —first proposed by Hoogerbrugge and Koelman [78] using heuristic arguments, and properly formalized by Español and Warren [79]— is a useful technique when studying the mesoscopic structure of complex liquids. BD is a technique that resembles DPD but each (mesoscopic) particle feels a random force and a drag force relative to a fixed background⁵. However, as we stressed in Chapter 1, we are interested in how the macroscopic behavior emerges from *microscopic* (atomistic) interactions rather than in modeling the dynamics of fluids from a *mesoscopic* point of view.

Statistical field theories are a complementary approach to the understanding of nonequilibrium ordering in the DLG and in related models. These approaches often pose great conceptual and computational challenges in themselves, but we will focus here on critical properties and renormalization group notions through the Langevin equation [1, 2]. This is a stochastic partial differential equation, which corresponds to a mesoscopic (coarse-grained) description of the system, and it is thought to describe low-frequency, small-wave number phenomena (such as critical properties). It takes into account only the relevant symmetries

⁵The important difference between BD and DPD is that BD does not satisfy Newton's third law and hence is does not conserve momentum. As a consequence, BD cannot reproduce hydrodynamic behavior.

for the problem under study and lets the fast degrees of freedom that we forget about in the coarse-grained description to act as noise. The Langevin equation for a field ϕ takes the following form [1, 2]

$$\frac{\partial\phi(\mathbf{r}, t)}{\partial t} = F[\phi] + G[\phi]\xi(\mathbf{r}, t), \quad (2.4)$$

where ξ is a random variable which represents a uncorrelated Gaussian white noise. F and G , which are determined in general from symmetry considerations, are analytic functionals of ϕ . In fact, these functionals include every analytic term consistent with the symmetries of the microscopic system. In principle, F and G can be determined phenomenologically through experiments and/or symmetry arguments. Other difficult procedure which is seldom carried out is the coarse-graining operation that produces the Langevin equation from the microscopic model, which follows, say, a master equation as Eq. (2.1). We adopt the latter procedure (we extend the scheme devised in Ref. [80]) in the Chapter 3 and in greater detail in the Appendix C.

Chapter 3

Lennard–Jones and Lattice models of driven fluids

The present chapter describes Monte Carlo (MC) simulations and field theoretical calculations that aim at illustrating how slight modifications of dynamics at the microscopic level may influence, even quantitatively, the resulting (nonequilibrium) steady state. With this aim, we take as a reference the *driven lattice gas* (DLG), which we described qualitatively in the previous chapter. We present and study related lattice and off-lattice microscopic models in which particles, as in the DLG, interact via a local anisotropic rule. The rule induces preferential hopping along one direction, so that a net current sets in if allowed by boundary conditions. In particular, we shall discuss on the similarities and differences between the DLG and its continuous counterpart, namely, a Lennard–Jones analogue in which the particles’ coordinates vary continuously. A comparison between the two models allows us to discuss some exceptional, hardly realistic features of the original discrete system — which has been considered a prototype for nonequilibrium anisotropic phase transitions.

3.1 Driven Lattice Gas

The *driven lattice gas* [53] is a nonequilibrium extension of the Ising model with conserved dynamics. The DLG consists of a d -dimensional square lattice gas in which pair of particles interact via an attractive and short-range Ising-like Hamiltonian,

$$H = -4 \sum_{\langle j, \mathbf{k} \rangle} \sigma_j \sigma_{\mathbf{k}} . \quad (3.1)$$

Here $\sigma_{\mathbf{k}}$ is the lattice occupation number at site $\mathbf{k} \in \mathbb{Z}^d$, and the sum runs over all the nearest-neighbor (NN) sites¹. Each lattice site has two possible states, namely, a particle ($\sigma_{\mathbf{k}} = 1$) or a hole ($\sigma_{\mathbf{k}} = 0$) may occupy each site \mathbf{k} . Cell

¹For $d = 2$, this corresponds with a lattice’s connectivity 4.

dimensions for the lattice are chosen so that the NN distance (*bond length*) was unity: $|\mathbf{j}-\mathbf{k}| = 1$. A configuration is given by $\sigma \equiv \{\sigma_{\mathbf{k}}; \mathbf{k} \in \mathbf{d}\text{-dimensional lattice}\}$. We shall restrict ourselves to two-dimensional $L_{\parallel} \times L_{\perp}$ lattices, that is, $\mathbf{d} = 2$. Dynamics is induced by the competition between a heat bath at temperature T and an external driving field \mathbf{E} which favors particle hops along one of the principal lattice directions, say horizontally (\hat{x} direction), as if the particles were positively charged. Consequently, for periodic boundary conditions, a nontrivial nonequilibrium steady state is set in asymptotically. This is formalized through a master equation similar to Eq. (2.1), where the transition probabilities per unit time $w(\sigma \rightarrow \sigma')$ are the Metropolis ones, namely,

$$w(\sigma \rightarrow \sigma') = \min \left\{ 1, e^{-(\Delta H + \mathbf{E} \cdot \delta)/(k_B T)} \right\}. \quad (3.2)$$

Where $\mathbf{E} \cdot \delta$ denotes the dot product between the field \mathbf{E} (oriented along \hat{x} direction) and δ , which is the attempted particle displacement, i.e., $\delta = (\mathbf{j} - \mathbf{k})(\sigma_{\mathbf{j}} - \sigma_{\mathbf{k}})$; and $\Delta H = H(\sigma') - H(\sigma)$. To be precise, $w(\sigma \rightarrow \sigma')$ stands for the *rate* for the particle-hole exchange $\sigma_{\mathbf{k}} \rightleftharpoons \sigma_{\mathbf{j}}$ when the configuration is σ ; the particle density $\rho = N/(L_{\parallel}L_{\perp})$ remains constant during the time evolution. The exchange $\sigma_{\mathbf{k}} \rightleftharpoons \sigma_{\mathbf{j}}$ corresponds to a particle jumping to a NN hole if $\sigma_{\mathbf{k}} \neq \sigma_{\mathbf{j}}$; we assume $w(\sigma \rightarrow \sigma') = 0$ otherwise, i.e., only NN particle-hole exchanges are allowed. This bias breaks detailed balance and establishes a nonequilibrium steady state. Typical configurations in the stationary regime of the DLG are shown in Fig. 2.1.

MC simulations by the biased *Metropolis* rate in Eq. (3.2) reveal that, as in equilibrium, the DLG undergoes a second order phase transition. At high enough temperature, the system is in a disordered state while, below a critical point (at $T \leq T_E$, where $E = |\mathbf{E}|$) it orders displaying anisotropic phase segregation. That is, an striped rich–particle phase then coexists with its gas. It is also found that, for a lattice half filled of particles, the critical temperature T_E monotonically increases with E from the Onsager value² $T_0 = T_{\text{Ons}} = 2.269 \text{ Jk}_B^{-1}$ to $T_{\infty} \simeq 1.4 T_{\text{Ons}}$. This limit ($E \rightarrow \infty$) corresponds to a *nonequilibrium* critical point. As a matter of fact, it was numerically shown to belong to a universality class other than the Onsager one, e.g., MC data indicates $\beta_{\text{DLG}} \simeq 0.33$ (instead of the Ising value $\beta = 1/8$ in two dimensions) for the order parameter critical exponent [11, 81, 82]. Typical configurations for the DLG in the large field limit were shown in Fig. 2.1.

Statistical field theory is a complementary approach to the understanding of nonequilibrium ordering in the DLG. The derivation of a general mesoscopic description is still an open issue, however. Two different approaches have been proposed. The *driven diffusive system* (DDS) [15, 83, 84], which is a *phenomenological* Langevin-type equation aimed at capturing all the relevant symmetries, predicts that the current will induce a predominant mean–field behavior and, in particular, $\beta_{\text{DDS}} = 1/2$. The *anisotropic diffusive system* (ADS) [80], which

²See Appendix A.

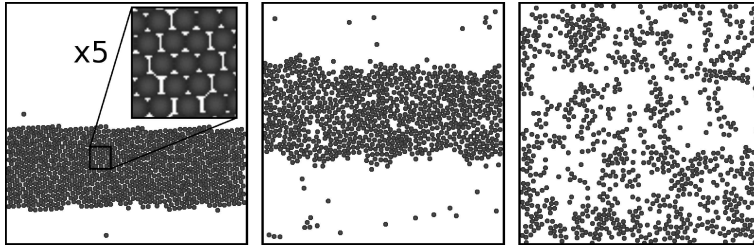


Figure 3.1: Typical configurations during the stationary regime of the DLJF subject to a horizontal field of intensity $E^* = 1$. These graphs, which are for $N = 900$ particles and density $\rho^* = 0.30$, illustrate, from left to right, (i) coexistence of a solid and its vapor (the configuration shown is for temperature $T^* = 0.20$), (ii) liquid–vapor coexistence ($T^* = 0.35$), and (iii) a disordered, fluid phase ($T^* = 0.50$). The left–most graph shows a detail of the solid strip. The particles, which move in a square box of side $\sqrt{N/\rho^*}$, are given here an arbitrary size, namely, diameter = 1.1σ .

follows after a coarse graining of the master equation, rules out the relevance of the current and leads to the above–indicated MC critical exponent for $E \rightarrow \infty$. However, the ADS approach reduces to the DDS for finite E , a fact which is hard to be fitted to MC data. In any case, field theoretical studies have constantly demanded further numerical efforts, and the DLG is nowadays the most thoroughly studied system showing an anisotropic nonequilibrium phase transitions. The topic is not exhausted, however. On the contrary, there remain unresolved matters such as the above mentioned issues concerning critical and mesoscopic behaviors, and the fact that T_E increases with E , which is counterintuitive [86, 85]. Another significant question concerns the observation of triangular anisotropies at early times after a rapid MC quench from the homogenous state (as if $T = \infty$) to $T < T_E$. The triangles happen to point against the field, which is contrary to the prediction from the DDS continuum equation [87].

In this chapter we present a description of driven systems with continuous variation of the particles’ spatial coordinates —instead of the discrete variations in the DLG— aiming for a new effort towards better understanding basic features of the DLG and its (and related) nonequilibrium phase transitions. This will provide a more realistic scheme for computer simulation of anisotropic fluids. Our strategy to set up the model is to follow as closely as possible the DLG. That is, we analyze an off–lattice representation of the DLG, namely, a microscopically *continuum* with the same symmetries. Investigating these questions happens to clarify the puzzling situation indicated above concerning the outstanding behavior of the DLG.

3.2 Driven Lennard-Jones fluid

Consider a *fluid* consisting of N point-like particles in a two-dimensional $L \times L$ ($L \equiv L_{\parallel} = L_{\perp}$) box with periodic (toroidal) boundary conditions. Interactions are according to a *truncated and shifted Lennard–Jones (LJ) 12-6 potential*³ [88]:

$$V(r_{ij}) = \begin{cases} V_{\text{LJ}}(r_{ij}) - V_{\text{LJ}}(r_c), & \text{if } r_{ij} < r_c \\ 0, & \text{if } r_{ij} \geq r_c, \end{cases} \quad (3.3)$$

where

$$V_{\text{LJ}}(r) = 4\epsilon [(\sigma/r)^{12} - (\sigma/r)^6] \quad (3.4)$$

is the full LJ potential. Here, $r_{ij} = |\mathbf{r}_i - \mathbf{r}_j|$ is the relative distance between particles i and j , ϵ and σ are our energy and length units, respectively, and r_c is the *cut-off* that we shall fix at $r_c = 2.5\sigma$. The choice of this potential obeys to our strategy to set up the model following as close as possible the DLG (see Eq. (3.1)). In fact, the potential defined in Eq. (3.3) is only one of the multiple possibilities for an attractive short-ranged potential⁴. The preferential hopping will be implemented as in the lattice, i.e., by adding a driving field to the potential energy. Consequently, the familiar energy balance which enters in Eq. (3.2) is (assuming $k_B \equiv 1$ hereafter) $H(\mathbf{c}) = \sum_{i < j} V(r_{ij})$, where (*continuum*) configurations \mathbf{c} are here $\mathbf{c} \equiv \{\mathbf{r}_1, \dots, \mathbf{r}_N\}$. The particle attempted displacement is therefore $\delta = \mathbf{r}'_i - \mathbf{r}_i$. Lacking a lattice, the field is the only source of anisotropy, and any trial move should only be constrained by a maximum displacement in the radial direction. That is, we take $0 < |\delta| < \delta_{\text{max}}$, where $\delta_{\text{max}} = 0.5\sigma$ in our simulations. We express the relevant quantities in terms of our energy ϵ and length σ scales, i.e., we introduce reduced units⁵. From these basic units, the temperature T , length L , number density $\rho = N/L^2$, internal energy U , and field E variables will be reduced respectively according to

$$T^* = T/\epsilon, \quad L^* = L/\sigma, \quad \rho^* = \rho\sigma^2, \quad U^* = U/\epsilon, \quad \text{and } E^* = E\sigma/\epsilon, \quad (3.5)$$

where $*$ denotes reduced units. This model thus reduces for $E \rightarrow 0$ to the well-known *truncated and shifted LJ fluid*, one of the most studied models in the computer simulation of fluids [88, 89].

We studied this *driven LJ fluid* (DLJF) in the computer by the MC method using an extended “canonical ensemble”, namely, fixed values for N , ρ^* , T^* , and E^* . Simulations involved up to $N = 10^4$ particles with parameters ranging as follows: $0.5 \leq E^* \leq 1.5$, $0.20 \leq \rho^* \leq 0.60$, $0.15 \leq T^* \leq 0.55$. The typical configurations one observes are illustrated in Fig. 3.1. As its equilibrium counterpart, the DLJF exhibits three different phases (at least): vapor, liquid, and solid (sort

³Often termed Weeks-Chandler-Andersen potential.

⁴It has been shown that the LJ potential provides accurate results for a variety of fluids, e.g., Argon [88].

⁵This is very convenient in molecular simulations, and, most importantly, if we do not use reduced units, we might miss the equivalence between corresponding states (*law of corresponding state*).

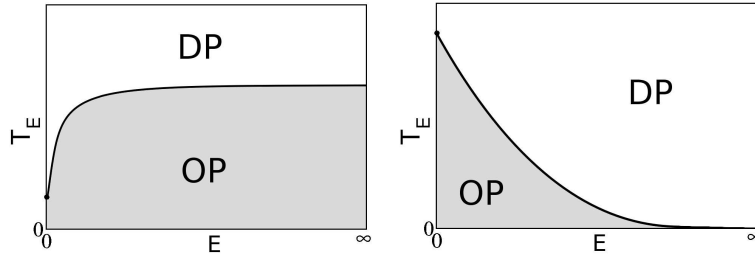


Figure 3.2: Schematic phase diagrams for the three models, as defined in the main text of this Chapter, showing ordered or striped (OP) and disordered (DP) phases. The left graph is for the DLG, for which $T_0 = T_{\text{Ons}}$. The graph on the right is valid for both the NDLG, i.e., the DLG with next-nearest-neighbor (NNN) hops, for which $T_0 = 2.32 T_{\text{Ons}}$, and the DLJF, for which $T_0^* = 0.459$ [89].

of close-packing phase; see the left-most graph in Fig. 3.1). At intermediate densities and low enough T^* , vapor and a condensed phase segregate from each other. The condensed droplet (see Fig. 3.1) is not near circular as it generally occurs in equilibrium, but strip-like extending along the field direction. A detailed study of each of these phases will be reported in Chapter 4 for a related system.

A main observation is that the DLJF closely resembles the DLG in that both depict a particle current and the corresponding anisotropic interface. However, they differ in an essential feature, as illustrated by Fig. 3.2. That is, contrary to the DLG, for which the critical temperature T_E increases with E , the DLJF shows a transition temperature T_E which decreases with increasing E . The latter behavior was expectable. In fact, as E is increased, the effect of the potential energy in the balance Eq. (3.2) becomes weaker and, consequently, the cohesive forces between particles tend to become negligible. Therefore, unlike for the DLG, there is no phase transition for a large enough field, and $T_E \rightarrow 0$ for $E \rightarrow \infty$ in the DLJF. Confirming this, typical configurations in this case are fully homogeneous for any T under a sufficiently large field E . One may think of variations of the DLJF for which $T_{E \rightarrow \infty} = \text{const} > 0$ (see Chapter 4), but the present one follows more closely the DLG microscopic strategy based on Eq. (3.2).

Concerning the early process of kinetic ordering, one observes triangular anisotropies in the DLJF that point along the field direction. That is, the early-time anisotropies in the off-lattice case (right graph in Fig. 3.3) are similar to the ones observed in mesoscopic approaches (as, for instance, the DDS approach), and so they point along the field, contrary to the ones observed in the discrete DLG (left graph in Fig. 3.3).

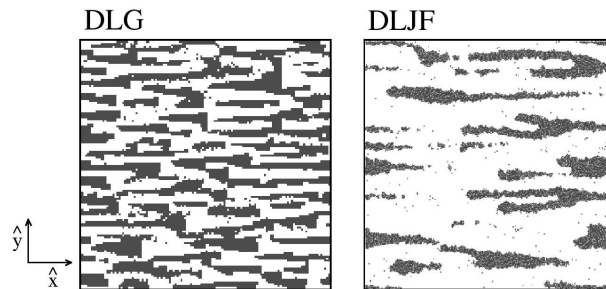


Figure 3.3: Triangular anisotropies as observed at early times for $E = 1$ in computer simulations of the lattice (left) and the off-lattice (right) models defined in the main text. The field points along the \hat{x} direction. The DLG configuration is for $t = 6 \times 10^4$ MC steps in a 128×128 lattice with $N = 7372$ particles and $T = 0.4T_{\text{Onsager}}$. The DLJF configuration is for $t = 1.5 \times 10^5$ MC steps, $N = 10^4$ particles, $\rho^* = 0.20$ and $T^* = 0.23$.

3.3 Driven Lattice Gas with extended dynamics

The above observations altogether suggest a unique exceptionality of the DLG behavior. This is to be associated with the fact that a driven particle is geometrically restrained in the DLG. In order to show this, we studied the lattice with an infinite drive extending the hopping to next-nearest-neighbors (NNN) [90, 91, 92]. That is, we extend interactions and accessible sites to the NNN. Thus, the sum in Eq. (3.1) involves the eight next-nearest neighbors instead of the four nearest neighbors of the standard DLG. In this case, the particle-hole exchange $\sigma_{\mathbf{k}} \leftrightarrow \sigma_{\mathbf{j}}$ corresponds to a particle hop to a NNN hole if $\sigma_{\mathbf{k}} \neq \sigma_{\mathbf{j}}$. As illustrated in Fig. 3.4, this introduces further relevant directions in the lattice, so that the resulting model, to be named here NDLG, is expected to behave closer to the DLJF. This is confirmed. For example, one observes in the discrete NDLG that, as in the continuum DLJF, T_E decreases with increasing E —though from $T_0 = 2.32 T_{\text{Ons}}$ in this case⁶—. This is illustrated in Fig. 3.2. Specifically, we discuss on this difference between the DLG and the NDLG in Appendix B, in where we define an intermediate model which capture both situations.

3.3.1 Correlations and Structure Factor

There is also interesting information in the two-point correlation function and (equal-time) structure factor. The former, which measures the degree of order of the lattice, is defined for a half-filled lattice as

$$C(\mathbf{i}) = \langle \sigma_{\mathbf{j}} \sigma_{\mathbf{i}+\mathbf{j}} \rangle - 1/4, \quad (3.6)$$

⁶For the Ising model with NNN interactions, one can derive easily theoretical estimates for the critical temperature [94].

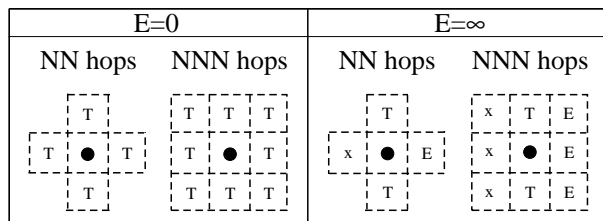


Figure 3.4: Schematic comparison of the accessible sites a particle (at the center, marked with a dot) has for nearest-neighbors (NN) and next-nearest-neighbors (NNN) hops at equilibrium (left) and in the presence of a large horizontal field (right). The particle-hole exchange between neighbors may be forbidden (x), depend only on the potential energy (T), or occur with probability 1 (E).

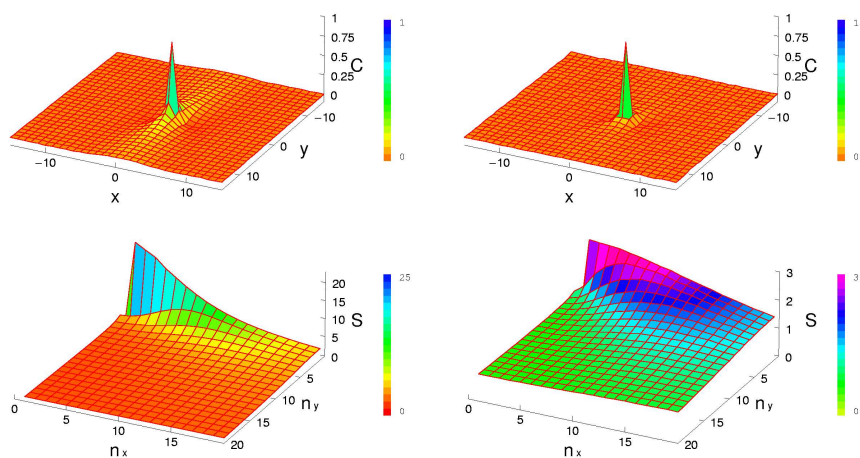


Figure 3.5: Surface plots of the two-point correlation (upper row) and the structure factor (lower row). These are for the DLG (left column) and NDLG (right column) on a $L_{\parallel} \times L_{\perp} = 128 \times 128$ lattice in the large field limit $E = \infty$. Temperatures are $T/T_{\text{Ons}} = 1.58$ and $T/T_{\text{Ons}} = 1.00$ for the DLG and the NDLG, respectively. Notice the change of color code with each plot.

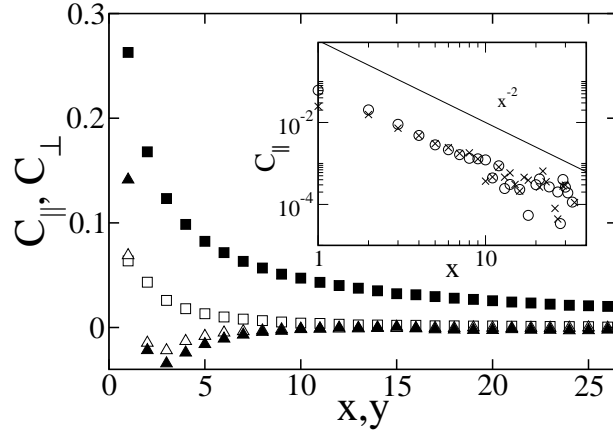


Figure 3.6: Parallel (squares) and transverse (triangles) components of the two-point correlation function above criticality for the DLG on a 128×128 lattice with NN hops/interactions (filled symbols) at $T = 1.58$ and NNN hops/interactions (empty symbols) at $T = 1$. Temperatures normalized to T_{Ons} . The inset shows the x^{-2} power law decay in C_{\parallel} for both discrete cases: DLG (\circ) and NDLG (\times).

where the steady average $\langle \dots \rangle$ involves averaging over \mathbf{j} . Translational invariance is assumed. The structure factor, which is the Fourier transform of the two-point correlation function, can be written in terms of the occupation variables as

$$S(\kappa) = \frac{1}{L^2} \left\langle \left| \sum_{\mathbf{r}} \sigma_{\mathbf{r}} e^{i\kappa \cdot \mathbf{r}} \right|^2 \right\rangle, \quad (3.7)$$

where κ is a wave vector which has components $\kappa_{x,y} = 2\pi n_{x,y}/L$ with $n_{x,y} = 0, 1, \dots, L-1$. This is very useful to distinguish disordered configurations from inhomogeneous one. To avoid complications due to inhomogeneous ordered phases, we compute for both the DLG and NDLG two-body correlations and structure factors above criticality. We show in Fig. 3.5 the surface plots of C and its Fourier transform S for both dynamics. Analysis of the components (shown in Fig. 3.6) along the field, $C_{\parallel} \equiv C(x, 0)$, and transverse to it, $C_{\perp} \equiv C(0, y)$, shows that correlations are qualitatively similar for the DLG and the NDLG —although somewhat weaker along the field for NNN hops. That is, allowing for a particle to surpass its forward neighbor does not modify correlations. In fact, both the DLG and the NDLG display generic slow decay of two-point correlations⁷ [95]. It is generally accepted [15] that the key ingredients which yield power-law decays are (i) a conserved dynamics, (ii) a non-equilibrium steady state, and (iii) spatial anisotropy associated with the dynamics. The

⁷This is in stark contrast with their equilibrium counterparts, the lattice gas (see Appendix A), in which correlations decay exponentially (except at the critical point). The latter is a common feature of all the systems at thermal equilibrium.

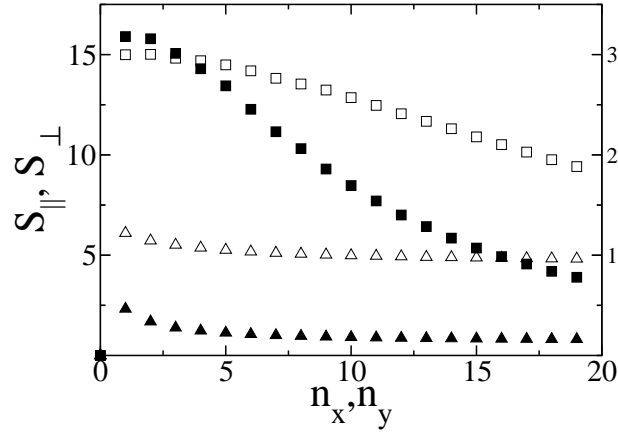


Figure 3.7: Parallel (squares) and transverse (triangles) components of the structure factor above criticality for the DLG on a 128×128 lattice for the DLG (filled symbols, left scale) at $T = 1.58$ and for the NDLG (empty symbols, right scale) at $T = 1$. Temperatures normalized to T_{Onsager} . Here, $n_{x,y} = 128 \kappa_{x,y} / 2\pi$.

first ingredient alone (as in equilibrium) cannot lead to generic power laws due to the validity of the *fluctuation dissipation theorem*. The role of the second ingredient is to lift the theorem's constraint, so that the power laws are now generic. The role of the third one is more subtle, necessary only for producing power laws in the two-body correlations.

The power-law behavior⁸ translates into a discontinuity of the structure factor, namely, $\lim_{\kappa_x \rightarrow 0} S_{\parallel} \neq \lim_{\kappa_y \rightarrow 0} S_{\perp}$, where $S_{\parallel} \equiv S(\kappa_x, 0)$ and $S_{\perp} \equiv S(0, \kappa_y)$. This is clearly confirmed in Fig. 3.7 for both NN and NNN hops/interactions. Notice that this singularity, which do not appear under equilibrium conditions, is an indication of the dependence of the nonequilibrium steady state on the (anisotropic) dynamic.

3.3.2 Critical behavior

As outlined in Section 3.1, the derivation of a general mesoscopic description is still an issue under contention. In order to shed more light on the field theoretical description of driven fluids, we try to derive a Langevin-type equation for the NDLG. To this end, firstly, we compute the order parameter critical exponent by means of standard finite size scaling techniques. Secondly, we derive the Langevin equation, which aim at describe the NDLG critical properties, by using the ADS approach [80]. We also discuss the viability of other approaches, e.g., the DDS approach.

⁸Together with the Ising symmetry violation by $E \neq 0$.

MC simulations

Assuming a half-filled lattice⁹ we perform finite size scaling analysis for the NDLG by following the scheme proposed in [15] consistent with the ADS theory [81]. The order parameter is chosen as the structure factor

$$m = S(0, 2\pi/L_{\perp}), \quad (3.8)$$

(as suggested in [96, 97, 98]), which carries the intrinsic anisotropies of the system. In order to perform systematic anisotropic finite size scaling we considered system sizes 80×40 , 25×50 , 45×30 , and 125×50 . These aspect ratios satisfy $L_{\parallel}^{\nu_{\perp}/\nu_{\parallel}} = 0.22 \times L_{\perp}$, where $\nu_{\perp}/\nu_{\parallel} \approx 1/2$ consistent with the ADS anisotropic spatial scaling [96, 97, 98]. A strong enough field is needed to avoid crossovers from the equilibrium regime. Notice also that, as we showed above for the NDLG, a saturating field suppresses the ordering, that is, $T_E = 0$ when $E \rightarrow \infty$. Therefore we choose an intermediate value for the field $E = 12$. The corresponding critical temperature is determined by using the Binder's fourth cumulant method [99], which is $T_{12} = 1.45 \pm 0.01$. The obtained critical value T_{12} was employed for the finite size scaling analysis.

Fig. 3.8 show the scaled order parameter m upon the distance to the critical point λ , for three different sizes of L_{\parallel} . The former is rescaled by $L_{\parallel}^{\beta/\nu_{\parallel}}$ whereas the latter is rescaled by $L_{\parallel}^{1/\nu_{\parallel}}$. The number of MC steps considered for each temperature was 160 millions. A perfect data collapse between the different system sizes is obtained by fixing $\nu_{\parallel} \approx 1.25$, $\gamma \approx 1.22$ and $\beta \approx 0.33$, where ν_{\parallel} , γ , and β are the corresponding critical exponents. Notice that these values are precisely the same for the DLG (with NN hops/interactions) [81]. As shown in Fig. 3.8, the asymptotic lines fit nicely with $\beta \approx 0.33$ (upper line), and $-\gamma/2 \approx -0.61$ (lower line).

We have also computed the susceptibility, defined as the relative fluctuations of the order parameter. This reads

$$\chi = \frac{L_{\parallel}}{\sin \pi/L_{\perp}} (\langle m^2 \rangle - \langle m \rangle^2) \quad (3.9)$$

The rescaled susceptibility is shown in Fig. 3.9. The best collapse is obtained with the same values as before. Plotting the dimensionless Binder cumulant b as a function of the rescaled distance to the critical point with $\nu_{\parallel} \approx 1.25$, again, nearly perfect collapse is obtained for all system sizes (as depicted in Fig. 3.10).

This set of MC results support that both the DLG and the NDLG belong to the same universality class, i.e., both dynamics yield the same critical indexes. In particular, it follows that the critical properties remains unchanged when extending hops and interactions from the nearest-neighbors to the next-nearest-neighbors.

⁹By following simple symmetry arguments, the critical density is $N/L_{\perp}L_{\parallel} = 1/2$.

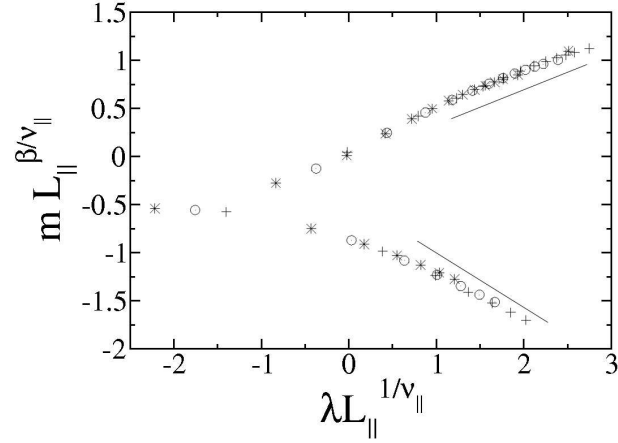


Figure 3.8: Log-log plot of the order parameter rescaled by $L_{\parallel}^{\beta/\nu_{\parallel}}$ vs. $\lambda L_{\parallel}^{1/\nu_{\parallel}}$, for different sizes: (+) 125×50 , (*) 45×30 , and (o) 80×40 . The upper straight line is for $\beta = 1/3$, whereas the lower one indicates $\gamma = 0.3$.

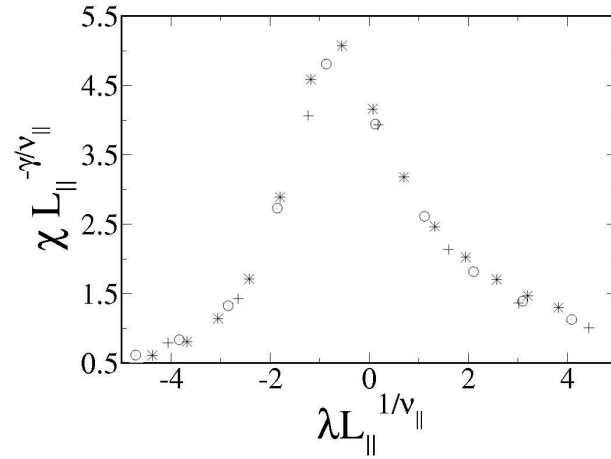


Figure 3.9: Log-log plot of the susceptibility rescaled by $L_{\parallel}^{-\gamma/\nu_{\parallel}}$ vs. $\lambda L_{\parallel}^{1/\nu_{\parallel}}$. Symbols are as in Fig. 3.8.

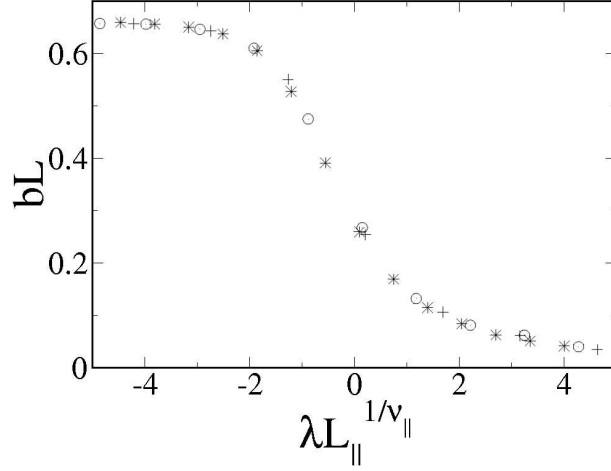


Figure 3.10: Scaling plot of the fourth Binder cumulant b vs. $\lambda L_{\parallel}^{1/\nu_{\parallel}}$. Symbols are as in Fig. 3.8.

Mesoscopic description

The ADS approach has been employed successfully to describe the critical behavior of the DLG [80]. The resulting Langevin-type equation, derived from a coarse-graining process from the DLG master (microscopic) equation sets up the anisotropy as the main nonequilibrium ingredient and leads to the right critical exponent in the large field limit ($\beta \approx 1/3$). The associated Langevin equation for the coarse-grained density $\phi(\mathbf{r}, t)$ reads

$$\partial_t \phi(\mathbf{r}, t) = -\nabla_{\perp}^4 \phi + (\tau + \alpha) \nabla_{\perp}^2 \phi + \frac{g}{3!} \nabla_{\perp}^2 \phi^3 + \frac{\alpha}{2} \nabla_{\parallel}^2 \phi + \xi(\mathbf{r}, t) \quad (3.10)$$

Here, the last term ξ stands for a Gaussian white noise, i.e., $\langle \xi(\mathbf{r}, t) \rangle = 0$ and $\langle \xi(\mathbf{r}, t) \xi(\mathbf{r}', t') \rangle = \delta(\mathbf{r} - \mathbf{r}') \delta(t - t')$, representing the fast degrees of freedom, and τ , α and g are model parameters.

This approach is certainly valuable because it represents a detailed connection between microscopic dynamics and their mesoscopic descriptions. Therefore, this important feature suggests that its validity can be extended to describe the critical behavior of the NDLG, which was studied by computational means in the previous subsection. Such a description include the microscopic details of diagonal dynamics which, in particular, should allow us to distinguish between the DLG and the NDLG. This is in contrast of other more heuristic approaches, as the DDS [15, 83, 84], which aim for the main symmetries of the DLG. The DDS approach is the natural extension of the conserved ϕ^4 theory for the Ising equilibrium model [100]. The most relevant prediction of the DDS is the mean field behavior $\beta = 1/2$, which conflicts with MC simulations. This is not surprising, because the DLG behavior is more complicated than its equilibrium counterpart, in which the symmetries and the influence of the dynamics is well

established. The same situation occurs when extending dynamics to the NNN: the DDS (heuristic) scheme leads again to the mean-field order parameter critical exponent. As a matter of fact, the DDS approach can not account for the diagonal (microscopic) degrees of freedom. Therefore, the DDS Langevin equation does not describe the NDLG critical properties.

The question is whether the ADS approach describes properly the critical behavior observed in the NDLG. This is addressed in this section.

Next, we outline the derivation of a Langevin equation for the NDLG by following the scheme proposed in [80]. (this derivation can be found in greater detail in Appendix C).

Let us define a density variable $\phi(\mathbf{r}, t)$ averaged in a region of volume v over which the original microscopic occupation variable ($\sigma_{\mathbf{k}}$ in Eq. (3.1)) were averaged. The system evolves from a (coarse-grained) configuration γ to another γ' by choosing randomly a particle at point \mathbf{r} and exchanging it with one of its next nearest neighbors in the direction μ [80]. Notice that, in contrast with the previous ADS approach for the DLG with NN interactions, now μ involves the known parallel \parallel and transversal \perp directions as well as the two additional directions which allow for the diagonal jumps \nearrow and \searrow . If v is large enough, then ϕ can be considered a continuum function of \mathbf{r} so we have

$$\gamma' = \{ \phi + v^{-1} \nabla_{\mu} \delta(\mathbf{r}' - \mathbf{r}), \text{ where } \phi \in \gamma \} \quad (3.11)$$

The distribution $P(\gamma, t)$ accounts for the statistical weight of each configuration γ at time t and evolves according to the following Markovian master equation [1]

$$\partial_t P(\gamma, t) = \sum_{\mu=\{\parallel, \perp, \nearrow, \searrow\}} \int d\eta f(\eta) \int d\mathbf{r} [\Omega(\gamma \rightarrow \gamma') P(\gamma, t) - \Omega(\gamma' \rightarrow \gamma) P(\gamma', t)] \quad (3.12)$$

where $\Omega(\gamma \rightarrow \gamma')$ stands for the transition probability per unit time (transition rate) from γ to γ' and $f(\eta)$ is an even function which account for the amount of mass attempted to be displaced. That is, Eq. (3.11)–(3.12) represent a process in which a configuration γ is exchanged with the infinitesimal neighbor of \mathbf{r} (γ') in the μ direction. As usual, the transition rates are taken to be a product of a function of the entropy times the same function of the difference between the configurations plus a term due to the effect of the driving field [33], namely,

$$\Omega(\gamma \rightarrow \gamma') = D(\Delta S(\eta)) \cdot D(\Delta H(\eta) + H_{\epsilon}). \quad (3.13)$$

Here, $H_{\epsilon} = \eta \mu \cdot \epsilon (1 - \phi^2) + \mathcal{O}(v^{-1})$, and D is a function satisfying detailed balance. Importantly, in the Langevin-type equations framework, ϵ represents a coarse-grained field acting upon a given configuration η . Indeed, the detailed dependence of the mesoscopic coefficients on the microscopic field introduced in Eq. (3.2) remain still as an open issue [11]. This constraint ensures that the limiting case of $\epsilon = 0$ the steady state solution of the master equation is the canonical one, i.e. $P(\gamma, t = \infty)|_{\epsilon=0} = e^{-H[\phi]}$. At a mesoscopic level, the

equivalent to Eq. (3.1) is the standard ϕ^4 (Ginzburg–Landau) Hamiltonian, and following a similar procedure as here the equilibrium Langevin equation is the so called *model B* [100]. The structure of the free energy consist of two contributions: a entropic and a energetic one which are given by, respectively

$$\begin{aligned} S(\eta) &= v \int d\mathbf{r} \left(\frac{\mathbf{a}}{2} \phi^2 + \frac{\mathbf{g}}{4!} \phi^4 \right) \\ H(\eta) &= v \int d\mathbf{r} \left(\frac{1}{2} (\nabla\phi)^2 + \frac{\tau}{2} \right). \end{aligned} \quad (3.14)$$

Here \mathbf{a} and \mathbf{g} are entropic coefficients whereas the parameter τ comes from the energetic contribution. From Eq. (3.12) a Fokker–Planck equation is derived by means of a Kramers–Moyal [1] expansion. The derivation is similar to the one in Ref. [80], but taking into account the transversal degrees of freedom for the NDLG. After using standard techniques in the theory of stochastic processes [1] we derive from the Fokker–Planck equation its stochastically equivalent Langevin equation using the Ito prescription, which reads

$$\partial_t \phi(\mathbf{r}, t) = \sum_{\mu} \nabla_{\mu} \left[p(\lambda_{\mu}^S, \lambda_{\mu}^H + \lambda_{\mu}^{\varepsilon}) + q(\lambda_{\mu}^S, \lambda_{\mu}^H + \lambda_{\mu}^{\varepsilon})^{1/2} \xi_{\mu}(\mathbf{r}, t) \right]. \quad (3.15)$$

where

$$\begin{aligned} \lambda_{\mu}^{\varepsilon} &= \mu \cdot \varepsilon (1 - \phi^2), \\ \lambda_{\mu}^X &= - \left(\nabla_{\mu} \frac{\delta}{\delta\phi} \right) X, \\ p(z_1, z_2) &= \int d\mathbf{r} \eta f(\eta) D(\eta z_1) D(\eta z_2), \\ q(z_1, z_2) &= \int d\mathbf{r} \eta^2 f(\eta) D(\eta z_1) D(\eta z_2). \end{aligned} \quad (3.16)$$

The time has been rescaled by v^{-1} and $\xi_{\mu}(\mathbf{r}, t)$ is a delta–correlated Gaussian white noise in the μ direction. After some algebra, the terms depending on both diagonal components $/$ and \backslash can be split into the two parallel and transversal to the field components. We now focus on the critical region and discard irrelevant terms in the renormalization group sense by naive power counting. We perform the following anisotropic scale transformations:

$$\begin{aligned} t &\rightarrow \tau^{-z} t, \\ r_{\perp} &\rightarrow \tau^{-1} r_{\perp}, \\ r_{\parallel} &\rightarrow \tau^{-s} r_{\parallel}, \\ \phi &\rightarrow \tau^{\delta} \phi. \end{aligned} \quad (3.17)$$

Expanding the Langevin equation Eq. (3.15) around $\tau = 0$ keeping only the more relevant terms, we found that the leading terms of the theory are $\nabla_{\perp}^4 \phi$ and $\nabla_{\parallel}^2 \phi$ which, together with imposing invariance of the time scale, the transverse

spatial interaction, and the transverse noise, under scale transformations, lead to $s = 2$, $\delta = (s + d - 3)/2$, and $z = 4$. According to this and after some cumbersome algebra, the Langevin equation for finite (coarse-grained) driving field contains a large bunch of field-dependent terms. Similarly to what occurs in the ADS approach for the DLG, just taking a large enough value of the field most of those terms vanish. By doing this, one is led to the following Langevin equation

$$\partial_t \phi(\mathbf{r}, t) = -\nabla_{\perp}^4 \phi + (\tau + \frac{3}{2}\alpha) \nabla_{\perp}^2 \phi + \frac{g}{4} \nabla_{\perp}^2 \phi^3 + \alpha \nabla_{\parallel}^2 \phi + \xi(\mathbf{r}, t) \quad (3.18)$$

The resulting equation resemble the one for NN interactions (see Eq. (3.10)), although in Eq. (3.18) appears additional prefactors of entropic nature. This is consistent with the fact that the model with the extended dynamics, i.e., the NDLG, possesses more neighbors than the DLG. The present equation for NNN interactions contains all the same symmetries as Eq. (3.10) and both lead to the same critical behavior. The value of the order parameter critical exponent that follows from a renormalization group analysis of Eq. (3.18) is $\beta = 1/3$, which is consistent with the observed in the MC simulations described above.

3.4 Conclusions

The above observations show that the nature of correlations is not enough to determine the phase diagram. There are already indications of this from the study of equilibrium systems, and also from other nonequilibrium models. That is, one may have a qualitatively different phase diagram but essentially the same two-point correlations by modifying the microscopic dynamics. It follows, in particular, that the exceptional behavior of the DLG cannot be understood just by invoking the two-point correlation function $C(\mathbf{i})$ —or, equivalently, the structure factor $S(\kappa)$ — or crude arguments concerning symmetries. The fact that particles are constrained to travel precisely along the two principal lattice directions in the DLG is the cause for its singular behavior. Or in other words, the lattice geometry acts more efficiently in the DLG as an ordering agent than the field itself, which occurs rarely in actual cooperative transport in fluids. This means that the ordering in the DLG is a *geometric* effect rather than *dynamic*. Allowing jumping along intermediate directions, as in both the NDLG and the DLJF, modifies essentially the phase diagram but not features —such as power-law correlations— that seem intrinsic of the nonequilibrium nature of the phenomenon. This special arrangement of particles is also lacking, for instance, when other orientations of the driving field [101] are considered. This also would explain certain irregular configurations observed in three dimensions [11], since this constraint is also lifted in the $d = 3$ case.

Rutenberg and Yeung [92] also performed quenching experiments for variations of the DLG¹⁰. They showed, in particular, that minor modifications in the

¹⁰They allow for NNN hops, but the Hamiltonian only involves the NN interactions.

DLG dynamics may lead to an inversion of the triangular anisotropies during the formation of clusters which finally condense into strips. Our observations above prove that such nonuniversal behavior goes beyond kinetics, namely, it also applies to the stationary state.

The unique exceptionality of the DLG has some important consequences. One is that this model involves features that are not frequent in nature. There are situations in which a drive induces stripes but not necessarily DLG behavior [61]. The fact that a particle impedes the freedom of the one behind to move along \hat{x} for a large enough field may only occur very seldom in cooperative transport in fluids. The NDLG is more realistic in this sense. In any case, the great effort devoted to the DLG during two decades has revealed important properties of both nonequilibrium steady states and anisotropic phase transitions. On the other hand, it ensues that, due to its uniqueness, the DLG does not have a simple *off-lattice* analog. This is because the ordering agent in the DLG is more the lattice geometry than the field itself. The fact that one needs to be very careful when modeling nonequilibrium phenomena —one may induce both a wrong critical behavior and an spurious phase diagram— ensues again in this example. This seems not to be so dramatic in equilibrium where, for example, the lattice gas is a useful oversimplification of a LJ fluid.

Concerning criticality, according to our observations we found that the *anisotropic diffusive system* approach include the microscopic details of transverse dynamics which, in particular, allow one to distinguish between the DLG and the NDLG. This is in contrast with other, more heuristic approaches, e.g., the *driven diffusive system*. The ADS approach lead to the right order parameter critical exponent given by MC simulations. We analyzed the order parameter, magnetization, and the fourth Binder cumulant in order to compute the critical exponents. By using anisotropic finite size scaling we have shown that, in spite of structural differences between them, both models belong to the same universality class, which is characterized by an order parameter critical exponent $\beta \approx 1/3$.

Consequently, their critical properties do not depend on this particular extension of the dynamics. There are other nonequilibrium models in which the corresponding critical behavior changes by such an extension of the dynamic from NN to NNN. This is, for instance, the case of a closely related lattice system (with NN *exclusion* under a driving field) devised by Dickman [93]: Extending the dynamics to NNN [91], the nature of the order–disorder transition which takes place in this model changes dramatically. We shall discuss further on this model in the next chapter.

Finally, we remark that in the novel fluid model introduced in this chapter, the particle ‘infinite freedom’ is realistic, as it is also the LJ potential. It may contain some of the essential physics in a class of nonequilibrium anisotropic phenomena and phase transitions. On the other hand, the model is simple enough to be useful in computer simulations, and it is endowed of even–simpler and functional lattice analogs such as the NDLG. In the following chapter (Chapter 4) we shall develop in greater detail this matter.

Chapter 4

Prototypical model for anisotropic phenomena in nonequilibrium fluids

In this chapter, we describe short-time kinetic and steady-state properties of the non-equilibrium phases, namely, (mono- and polycrystalline) solid, liquid and gas anisotropic phases in a novel driven Lennard-Jones fluid. This is a computationally-convenient model which exhibits a net current and striped structures at low temperature, thus resembling many situations in nature. We here focus on both critical behavior and some details of the early nucleation process, by far less studied than later regimes. In spite of the anisotropy of the late-time “spinodal decomposition” process, earlier nucleation seems to proceed by *Smoluchowski coagulation* and *Ostwald ripening*, which are known to account for nucleation in equilibrium, isotropic lattice systems and actual fluids. On the other hand, a detailed analysis of the system critical behavior rises some intriguing questions on the role of symmetries; this concerns the computer and field-theoretical modeling of nonequilibrium fluids.

4.1 Motivation

The microscopic mechanism of stripe formation in particular materials is still not clear¹. Hence, lacking theory for the “thermodynamic” instabilities causing the observed striped structures, one tries to link them to the microscopic dynamics of suitable model systems. As we explained in the previous chapters, the *driven lattice gas* (DLG) [53], namely, a model system in which particles diffuse under an external driving field, has been up to now a theoretical prototype of anisotropic behavior [11, 15, 20]. This model was shown in Chapter 3 to be un-

¹For instance, in high-temperature superconductors [102], questions such as whether or not the Coulomb interactions are important in these kind of materials remain unresolved.

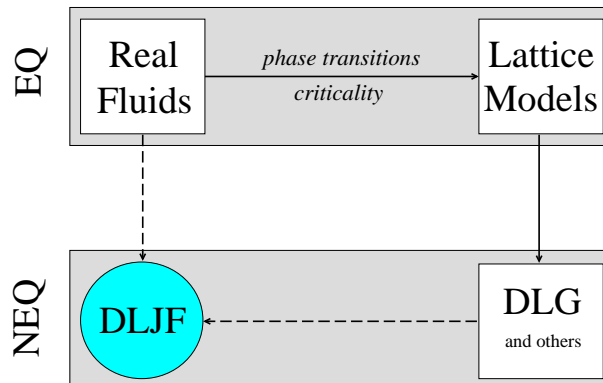


Figure 4.1: The place of our novel off-lattice models (as, for instance, the DLJF introduced in the previous chapter) in the realm of computer simulation of fluids.

realistic in some essential sense, however. Particle moves in the DLG are along the principal lattice directions, and any site can hold one particle at most, so that a particle impedes the one behind to jump freely along the direction which is favored to model the action of the field. Consequently, the lattice geometry acts more efficiently in the DLG as an ordering agent than the field itself, which occurs rarely —never so dramatically— in actual cooperative transport in fluids. In fact, actual situations may in principle be more closely modeled by means of continuum models, and this peculiarity of the DLG implies that it lacks a natural off-lattice extension.

Here we present and analyze numerically a novel nonequilibrium off-lattice, *Lennard–Jones* (LJ) system which is a candidate to portray some of the anisotropic behavior in nature². The model, which involves a driving field of intensity E , reduces to the celebrated (equilibrium) LJ *fluid* [88, 89] as $E \rightarrow 0$. For any $E > 0$, however, it exhibits currents and anisotropic phases as in many observations out of equilibrium. In particular, as the DLG, our model in two dimensions shows striped steady states below a critical point. We also observe critical behavior consistent with the equilibrium universality class. This is rather unexpected in view of the criticality reported both for the DLG. On the other hand, concerning the early-time relaxation before well-defined stripes form by spinodal decomposition, we first observe —as in previous studies of relaxation towards equilibrium— effective diffusion of small droplets, which is followed by monatomic diffusion probably competing with more complex processes. It is very likely that our observations here concerning nucleation, coexistence, criticality, and phases morphology hold also in a number of actual systems.

Before going further is worthy to mention that the off-lattice models³ devised along this thesis fills a void in the physics of nonequilibrium fluids. This

²This is in fact a related model to the *driven Lennard–Jones fluid* (DLJF) introduced in the previous Chapter.

³Here we include the DLJF model defined in Chapter 3.

is schematized in Fig. 4.1. As we explained in Chapter 1, lattice models are very convenient, simplified models which often capture the main ingredients of equilibrium systems, particularly, close to the critical points. For instance, the *lattice gas* may be a useful representation of, e.g., a Lennard-Jones fluid. However, rather surprisingly, nonequilibrium critical phenomena are by far much more studied in nonequilibrium extensions of lattice models than in their *continuum* counterparts. In this chapter, we provide a more *realistic*—without loss the efficiency of lattice models—, convenient model for the study of nonequilibrium phase transitions in fluids as well as give simple procedures to extend the study of actual fluids to the nonequilibrium realm.

In section 4.2 we define the off-lattice model, and section 4.3 is devoted to the main results as follows. § 4.3.1 describes the early-time segregation process as monitored by the excess energy, which measures the droplets surface. § 4.3.2 describes some structural properties of the steady state, namely, the radial and azimuthal distribution functions, and the degree of anisotropy. § 4.3.3 depicts some transport properties. And § 4.3.4 is devoted to an accurate estimate of the liquid–vapor coexistence curve and the associated critical parameters. Finally, Section 4.4 contains the main conclusions and final comments.

4.2 The model

Consider N particles of equal mass (set henceforth to unity) in a d -dimensional square box, L^d , with periodic boundary conditions. Interactions are via the truncated and shifted pair potential [88] (already defined in Chapter 3; see Eq. (3.3)):

$$\phi(\mathbf{r}) = \begin{cases} \phi_{\text{LJ}}(\mathbf{r}) - \phi_{\text{LJ}}(\mathbf{r}_c) & \text{if } r < r_c \\ 0 & \text{if } r \geq r_c, \end{cases} \quad (4.1)$$

where

$$\phi_{\text{LJ}}(\mathbf{r}) = 4\epsilon [(\sigma/r)^{12} - (\sigma/r)^6] \quad (4.2)$$

is the full LJ potential, r stands for the interparticle distance, and r_c is a *cut-off* that we set $r_c = 2.5\sigma$. The parameters σ and ϵ are, respectively, the characteristic length and energy—that we use in the following to reduce units as in Eq. (3.5).

Time evolution is by microscopic dynamics according to the transition probability per unit time (*rate*):

$$\omega^{(\text{E})}(\eta \rightarrow \eta') = \chi^{(\text{E})} \times \min \left\{ 1, e^{-\Delta\Phi/\Gamma} \right\}. \quad (4.3)$$

Here, $\chi^{(\text{E})}$, which is a nonequilibrium extension of the Metropolis rate [54], reads

$$\chi^{(\text{E})} = \frac{1}{2} [1 + \tanh(\mathbf{E}\hat{\mathbf{x}} \cdot \delta)], \quad (4.4)$$

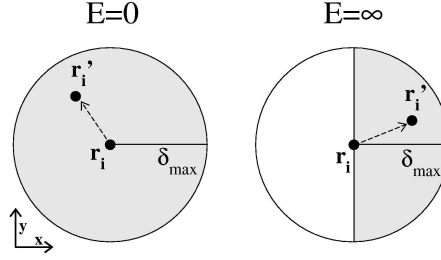


Figure 4.2: Schematic representation of the region (grey) which is accessible to a given particle as a consequence of a trial move for $E = 0$ (left-hand side) and $E = \infty$ (right-hand side), assuming the “infinite” field points \hat{x} , horizontally.

E is the intensity of a uniform external field along the horizontal direction, say \hat{x} , $\eta \equiv \{\mathbf{r}_1, \dots, \mathbf{r}_N\}$ stands for any configuration of energy

$$\Phi(\eta) = \sum_{i < j} \phi(|\mathbf{r}_i - \mathbf{r}_j|), \quad (4.5)$$

where \mathbf{r}_i is the position of particle i that can be anywhere in the d -torus, η' equals η except for the displacement of a single particle by $\delta = \mathbf{r}'_i - \mathbf{r}_i$, and $\Delta\Phi \equiv \Phi(\eta') - \Phi(\eta)$ is the cost of such displacement.

It is to be remarked that $\chi^{(E)}$, as defined in (4.4), contains a drive bias (see Fig. 4.2) such that the rate (4.3) lacks invariance under the elementary transitions $\eta \leftrightarrow \eta'$. Consequently, unlike in equilibrium, there is no detailed balance for toroidal boundary conditions if $E > 0$.

Here we describe the results from a series of Monte Carlo (MC) simulations. In order to reduce unnecessary interparticle distance calculations, we used a standard neighbor-list algorithm [88]. Our simulations concern fixed values of N , with $N \leq 10^4$, particle density $\rho = N/L^d$ within the range $\rho \in [0.2, 0.6]$, and temperature $T \in [10^{-2}, 10^5]$. Following the fact that most studies of striped structures, e.g., many of the ones are mentioned in the Chapter 2, concern two dimensions—in particular, the DLG critical behavior is only known with some confidence for $d = 2$ [11, 81, 82]—we restricted ourselves to a two dimensional torus. We fixed the maximum particle displacement is $\delta_{\max} = 0.5$ in our simulations as shown in Fig. 4.2. We deal below with steady-state averages over 10^6 configurations, and kinetic or time averages over 40 or more independent runs.

The distribution of displacements δ is uniform, except that the new particle position \mathbf{r}'_i is (most often in our simulations) sampled only from within the half-forward semi-circle of radius δ_{\max} centered at \mathbf{r}_i , as illustrated on the right-hand graph of Fig. 4.2. This is because the *infinite-field* limit, $E \rightarrow \infty$, turns out to be most relevant, and this means, in practice, that any displacement contrary to the field is forbidden. This choice eliminates from the analysis one parameter and, more importantly, it happens to match a physically relevant case. As a matter of fact, simulations reveal that any external field $E > 0$ induces a flux of particles

along \hat{x} —which crosses the system with toroidal boundary conditions— that monotonically increases with E , and eventually saturates to a maximum. This is a realistic stationary condition in which the thermal bath absorbs the excess of energy dissipated by the drive. Our simulations here concern only $E = \infty$ in order to maximize the nonequilibrium effects⁴.

4.3 Main results

Figure 4.3 illustrates late-time configurations, i.e., the ones that typically characterize the steady state, as the temperature T is varied. These graphs already suggest that the system undergoes an order-disorder phase transition at some temperature T_E . This happens to be of second order for any $E > 0$, as in the equilibrium case $E = 0$. We also observe that T_E decreases monotonically with increasing E , and that it reaches a well-defined minimum, T_∞ , as $E \rightarrow \infty$.

Figure 4.3 also shows that, at low enough temperature, an anisotropic interface forms between the condensed phase and its vapor; this extends along \hat{x} throughout the system at intermediate densities.

4.3.1 Phase segregation kinetics

Skipping microscopic details, the kinetics of phase segregation at late times looks qualitatively similar to the one in other nonequilibrium cases, including the DLG [103] and both molecular-dynamic [104] and Cahn-Hilliard [105] representations of sheared fluids, while it essentially differs from the one in the corresponding equilibrium system. This is illustrated in Fig. 4.4. One observes, in particular, condensation of many stripes—as in the graph for $t = 10^5$ in Fig. 4.4— into a single one—as in the first three graphs at the bottom row in Fig. 4.3. This process corresponds to an anisotropic version of the so-called *spinodal decomposition* [106], which is mainly characterized by a tendency towards minimizing the interface surface as well as by the existence of a unique relevant length, e.g., the stripe width [103]. We focus here on a detailed study of the early-time separation process instead of the late regime, which has already been studied for both equilibrium [107, 108] and nonequilibrium cases, including the DLG [103, 109]. This is because detailed descriptions of early nonequilibrium nucleation are rare as compared to studies of the segregation process near completion.

Following an instantaneous quench from a disordered state into $T < T_\infty$, one observes in our case that small clusters form, and then some grow at the expenses of the smaller ones but rather independently of the growth of other clusters of comparable size. This corresponds to times $t < 10^5$ in Fig. 4.4, i.e., before many well-defined stripes form. We monitored in this regime the *excess energy* or *enthalpy*, $H(t)$, measured as the difference between the averaged internal energy at time $t > 0$ and its stationary value. This reflects more accurately the

⁴We are interested in the far-from-equilibrium effects induced by the external driving field rather than in weak deviations from equilibrium.

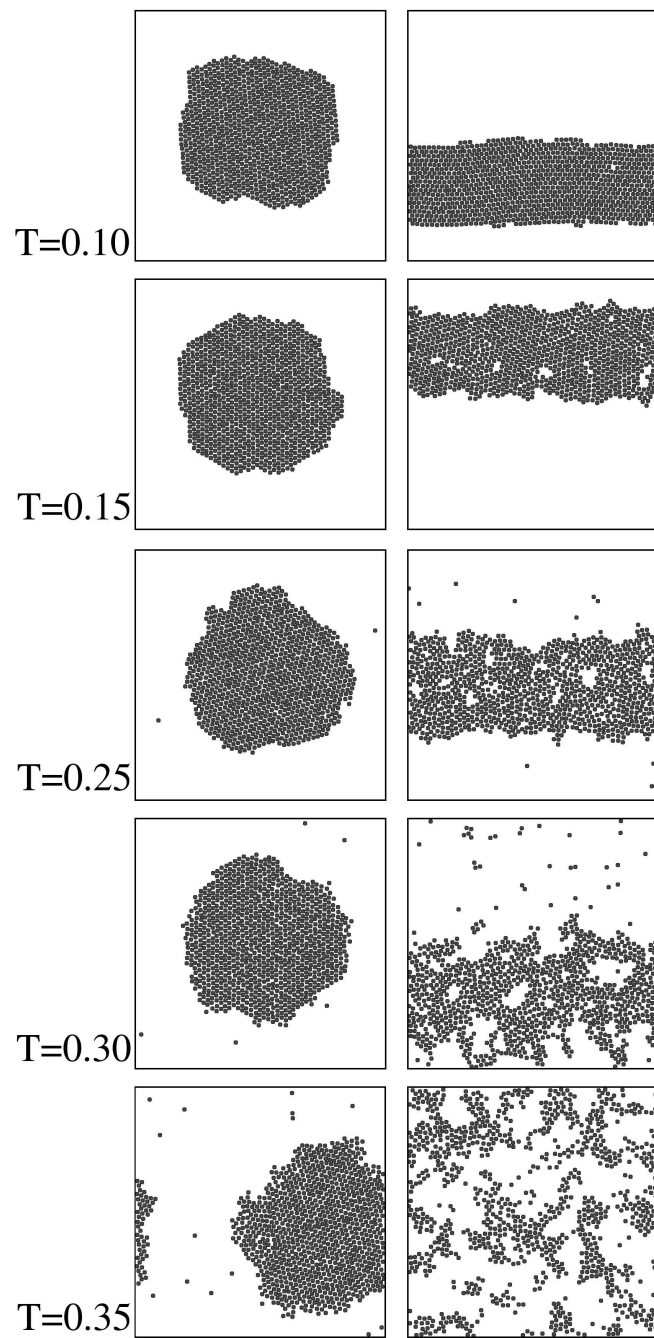


Figure 4.3: Typical steady-state configurations for $E = 0$ (left column) and $E \rightarrow \infty$ (right column) at different temperatures as indicated. This is for $N = 1000$ and $\rho = 0.30$. The field is oriented along the horizontal direction.

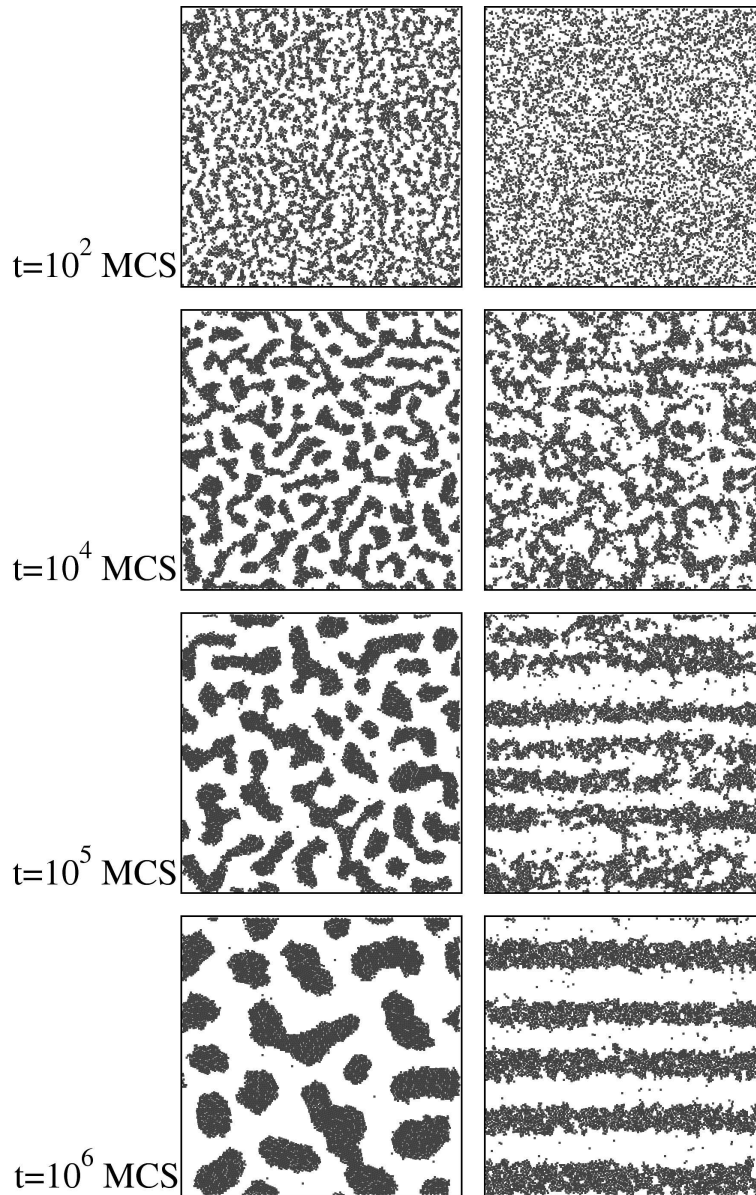


Figure 4.4: Typical configurations for $E = 0$ (top row) and $E \rightarrow \infty$ (bottom row) as time proceeds during relaxation from a disordered state (as for $T \rightarrow \infty$) at $t = 0$. The time here is proportional to the MC steps (MCS) as indicated. This is for $N = 7500$, $\rho = 0.35$, and $T = 0.275$, below the corresponding transition temperature.

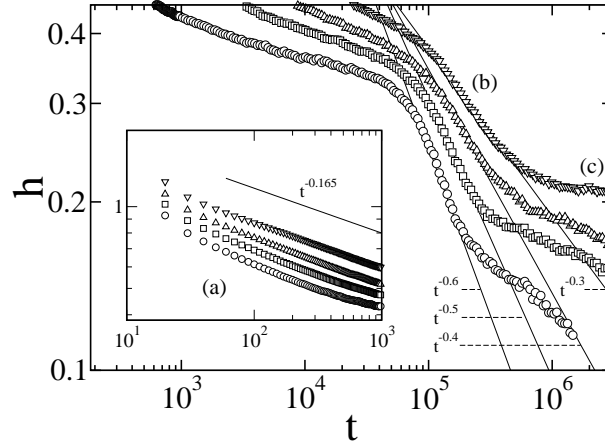


Figure 4.5: Time evolution of the enthalpy per particle for $N = 7500$, $\rho = 0.35$ and, from top to bottom, $T = 0.200$, 0.225 , 0.250 , and 0.275 . Straight lines are a guide to the eye; the slope of each line is indicated. The inset shows the detail at early times. (For clarity of presentation, the main graph includes a rescaling of the time corresponding to the data for $T = 0.250$, 0.225 and 0.200 by factors 2, 3 and 3, respectively.)

growth of the condensed droplets than its size or radius, which are difficult to be estimated during the early stages [110, 111]. In addition to its theoretical importance, the excess of energy may be relevant for experimentalists. This is because $H(t)$ may be determined in microcalorimetric experiments [112].

The time development of the enthalpy density $h(t) = H(t)/N$ is depicted in Fig. 4.5. This reveals some well-defined regimes at early times.

The first regime, (a) in the inset of Fig. 4.5, follows a power law $t^{-\theta}$ with $\theta \approx 1/6$ —which corresponds to the line shown in the graph— independently of the temperature investigated. This is the behavior predicted by the *Smoluchowski coagulation* or effective cluster diffusion [99]. The same behavior was observed in computer simulations for $E = 0$ and also reported to hold in actual experiments on binary mixtures [110, 112]. Surprisingly, this suggests the early dominance of a rather stochastic mechanism, in which the small clusters rapidly nucleate, which is practically independent of the field, i.e., it is not affected in practice by the drive. It is also noticeable that, in contrast with simulations on lattice gases in which this regime is rather noisy, a slope $t^{-1/6}$ appears clearly in Fig. 4.5. The indication of some temperature dependence in equilibrium [111], which is not evident here, might correspond to the distinction between *deep* and *shallow quenches* made in Ref. [110] that we have not investigated out of equilibrium.

At later times, there is a second regime, (b) in Fig. 4.5, in which the anisotropic clusters merge into filaments and, finally, stripes. We observe in this regime that θ varies between 0.3 and 0.6 with increasing T . *Ostwald ripening* [113], consisting of monomers diffusion, predicts $\theta = 1/3$ for fluids at thermal

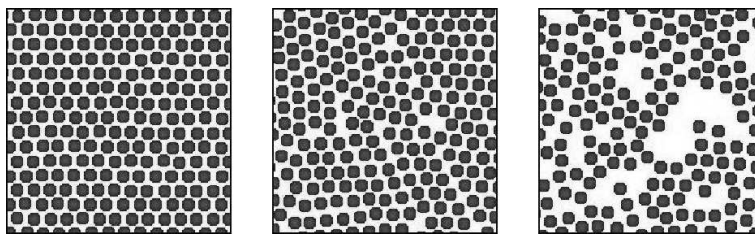


Figure 4.6: Details of the structure in the low- T , solid phase as obtained by zooming into configurations such as the ones in Fig. 4.3. This is for $T = 0.05$, 0.12 , and 0.25 , from left to right, respectively.

equilibrium. The situation here in our nonequilibrium is more complicate: it is likely that regime (b) describes a crossover from a situation which is dominated by monomers at low enough temperature to the emergence of other mechanisms [108, 114] which might be competing as T is increased.

Finally, one observes a regime, (c) in Fig. 4.5, which corresponds to the beginning of spinodal decomposition.

4.3.2 Structure of the steady state

Concerning the local structure in the stationary regime, for any $E > 0$, the anisotropic condensate changes from a solidlike hexagonal packing of particles at low temperature (e.g., $T = 0.10$ in Fig. 4.3), to a polycrystalline or perhaps glass-like structure with domains which show a varied morphology at, e.g., $T = 0.12$. The latter phase further transforms, with increasing temperature, into a fluid-like structure at, e.g., $T = 0.30$ and, finally, into a disordered, gaseous state.

More specifically, the typical situation we observe at low temperature is illustrated in Fig. 4.6. At sufficiently low temperature, $T = 0.05$ in the example, the whole condensed phase orders according to a perfect hexagon with one of its main directions along the field direction \hat{x} . This is observed in approximately 90% of the configurations that we generated at $T = 0.05$, while all the hexagon axes are slanted with respect to \hat{x} in the other 10% cases. As the system is heated up, the stripe looks still solid at $T = 0.12$ but, as illustrated by the second graph in Fig. 4.6, one observes in this case several coexisting hexagonal domains with different orientations. The separation between domains is by line defects and/or vacancies. Interesting enough, as it will be shown later on, both the system energy and the particle current are practically independent of temperature up to, say $T = 0.12$. The hexagonal ordering finally disappears in the third graph of Fig. 4.6, which is for $T = 0.25$; this case corresponds to a fluid phase according to the criterion below.

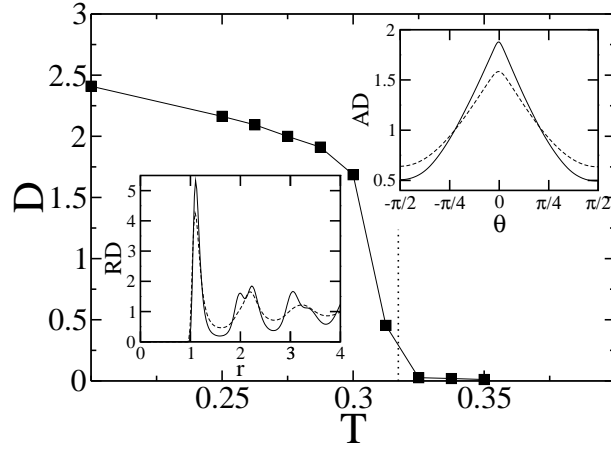


Figure 4.7: Data from simulations for $N = 7000$ and $\rho = 0.35$. The main graph shows the degree of anisotropy, as defined in the main text, versus temperature. The vertical dotted line denotes the transition temperature. The lower (upper) inset shows the radial (azimuthal) distribution at $T = 0.20$, full line, and $T = 0.30$, dashed line.

A close look to the structure is provided by the radial distribution (RD),

$$g(r) = \rho^{-2} \left\langle \sum_{i < j} \delta(\mathbf{r}_i - \mathbf{r}_j) \right\rangle, \quad (4.6)$$

i.e., the probability of finding a pair of particles a distance r apart, relative to the case of a random spatial distribution at same density. This is shown in the lower inset of Fig. 4.7. At fixed T , the driven fluid is less structured than its equilibrium counterpart, suggesting that the field favors disorder. This is already evident in Fig. 4.3, and it also follows from the fact that the critical temperature decreases with increasing E .

Further information on the essential anisotropy of the problem is beared by the azimuthal distribution (AD), which accounts for the long range ordering. This is defined

$$\alpha(\theta) = N^{-2} \left\langle \sum_{i < j} \delta(\theta - \theta_{ij}) \right\rangle, \quad (4.7)$$

where $\theta_{ij} \in [0, 2\pi)$ is the angle between the line connecting particles i and j and the field direction \hat{x} . Except at equilibrium, where this is uniform, the AD is $\pi/2$ -periodic with maxima at $k\pi$ and minima at $k\pi/2$, where k is an integer. This means that the field favors long-range longitudinal ordering instead of order along other directions. This is consistent with the observations in which the orientations of the hexagons in the solidlike phase are parallel to the field direction. The AD is depicted in the upper inset of Fig. 4.7.

We also monitored the *degree of anisotropy*, defined as the distance D

$$D = \int_0^{2\pi} d\theta |\alpha(\theta) - 1|, \quad (4.8)$$

which measures the deviation from the equilibrium, isotropic case, for which $\alpha(\theta) = 1$, independent of θ . The function (4.8), which is depicted in the main graph of Fig. 4.7, reveals the existence of anisotropy even above the transition temperature. This shows the persistence of nontrivial two-point correlations at high temperatures which has been demonstrated for other nonequilibrium models [95].

4.3.3 Transport properties

The current is highly sensitive to the anisotropy. The most relevant information is carried by the transverse-to-the-field current profile j_{\perp} , which shows the differences between the two coexisting phases (Fig. 4.8). Above criticality, where the system is homogeneous, the current profile is flat on the average. Otherwise, the condensed phase shows up a higher current (lower mean velocity) than its mirror phase, which shows up a lower current (higher mean velocity). Both the transversal current and velocity profiles are shown in Fig. 4.8. The current and the density vary in a strongly correlated manner: the high current phase corresponds to the condensed (high density) phase, whereas the low current phase corresponds to the vapor (low density) phase. This is expectable due to the fact that there are many carriers in the condensed phase which allow for higher current than in the vapor phase. However, the mobility of the carriers is much larger in the vapor phase. The maximal current occurs in the interface, where there is still a considerable amount of carriers but they are less bounded than in the particles well inside the *bulk* and, therefore, the field drives easily those particles. This enhanced current effect along the interface is more prominent in driven lattice models (notice the large peak in the current profile in Fig. 4.8). Thus, these are clear cases of interfacially driven transport [115]. Moreover in both lattice cases, DLG and NDLG (already studied in Chapter 3), there is no difference between the current displayed by the coexisting phases because of the particle-hole symmetry. Such a symmetry is derived from the Ising-like Hamiltonian in Eq. (3.1) and it is absent in the off-lattice case.

Regarding the comparison between off-lattice and lattice transport properties, Fig. 4.9 shows the net current j , defined as the mean displacement per MC step per particle, as a function of temperature. Saturation is only reached at $j_{\max} = 4\delta_{\max}/3\pi$ when $T \rightarrow \infty$. The current approaches its maximal value logarithmically, i.e., slower than the exponential behavior predicted by the Arrhenius law. The way this limit is approached is illustrated in the inset of Fig. 4.9. The sudden rising of the current as T is increased can be interpreted as a transition from a poor-conductor (low-temperature) phase to a rich-conductor (high-temperature) phase, which is reminiscent of ionic currents [11]. This behavior of the current also occurs in the DLG. Revealing the persistence of

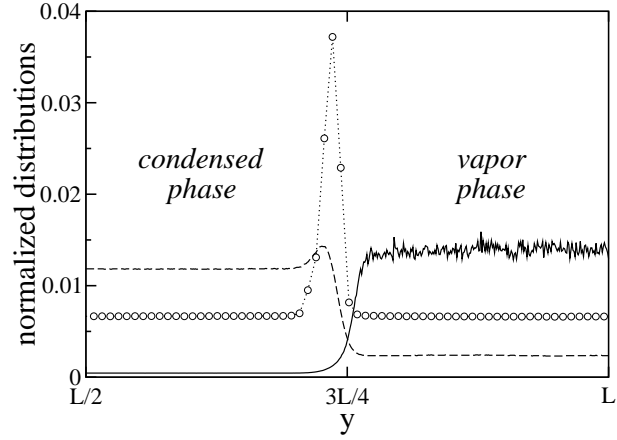


Figure 4.8: . Transverse-to-the-field current profiles below criticality. The shaded (full) line corresponds to the current (velocity) profile of the off-lattice model. For comparison we also show the current profile of the DLG (circle-dotted line). Since each distribution is symmetric with respect to the system center of mass (located here at $L/2$) we only show their right half parts.

correlations, the current is nonzero for any, even low T , though it is small, and roughly independent of T , in the solid phase.

An insight of the transition points between the different phases is obtained from the temperature dependence of the mean potential energy per particle $f = N^{-1} \langle \Phi(\eta) \rangle$ and from the net current j . In particular, one may estimate the transition point as the condensed strip changes from solid to liquid ($T \approx 0.15$) and finally changes to a fully disordered state ($T \approx 0.31$), i.e., disordered state. This is shown in Fig. 4.9 which exhibits well-defined changes of slope in both magnitudes when the phases transform. Notice also that the mean energy behaves linearly with temperature for $T \in (0.12, 0.3)$ in the liquid phase.

4.3.4 Coexistence curve

One of the main issues concerning the steady state is the liquid-vapor coexistence curve and the associated critical behavior. The (nonequilibrium) coexistence curve may be determined from the density profile transverse to the field. This is illustrated in Fig. 4.10.

At high enough temperature—in fact, already at $T = 0.35$ in this case for which the transition temperature is slightly above 0.3—the local density is roughly constant around the mean system density, $\rho = 0.35$ in Fig. 4.10. As T is lowered, the profile accurately describes the existence of a single stripe of condensed phase of density ρ_+ which coexists with its vapor of density ρ_- ($\rho_- \leq \rho_+$). The interface becomes thinner and smother, and ρ_+ increases while ρ_- decreases, as T is decreased.

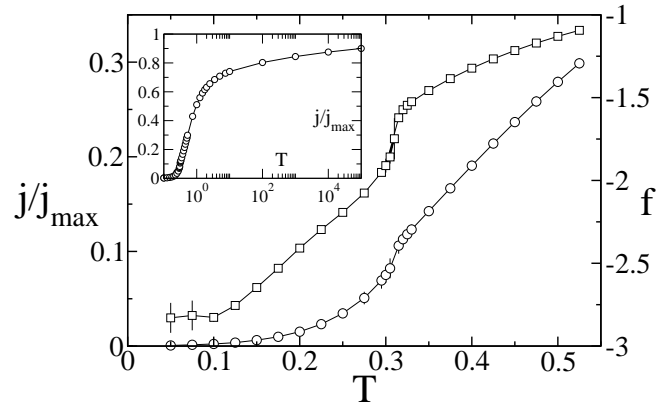


Figure 4.9: Temperature dependence of the mean energy (squares; the scale is on the right axis) and normalized net current (circles; scale at the left) for $N = 5000$ and $\rho = 0.30$ under “infinite” field. The inset shows the T -dependence of the current over a wider range.

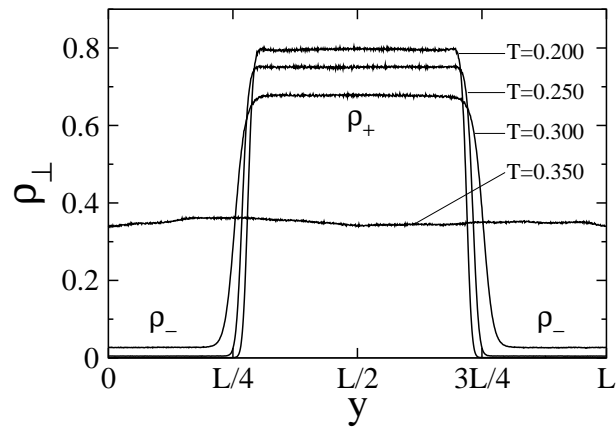


Figure 4.10: Density profiles transverse to the field for $N = 7000$, $\rho = 0.35$, and different temperature, as indicated. The coexisting densities, ρ_{\pm} , are indicated.

Table 4.1: Critical parameters

ρ_∞	T_∞	β
0.321(5)	0.314(1)	0.10(8)

As in equilibrium, one may use $\rho_+ - \rho_-$ as an order parameter. The result of plotting ρ_+ and ρ_- at each temperature results in the non-symmetric liquid-vapor coexistence curve shown in Fig. 4.11. The same result follows from the current, which in fact varies strongly correlated with the local density. Notice that the accuracy of our estimate of ρ_\pm is favored by the existence of a linear interface, which enable us to get closer to the critical point than in equilibrium. Lacking a *thermodynamic* theory for “phase transitions” in nonequilibrium liquids, other approaches have to be considered in order to estimate the critical parameters.

Consider to the rectilinear diameter law

$$\frac{1}{2}(\rho_+ + \rho_-) = \rho_\infty + b_0(T_\infty - T), \quad (4.9)$$

which is a empirical fit [4] extensively used for fluids in equilibrium. Here ρ_∞ and T_∞ denotes the critical density and the critical temperature, respectively. This, in principle, has no justification out of equilibrium. However, we found that our MC data nicely fit the diameters equation. We use this fact together with a universal scaling law⁵

$$\rho_+ - \rho_- = a_0(T_\infty - T)^\beta, \quad (4.10)$$

to accurately estimate the critical parameters. The simulation data in Fig. 4.11 then yields the values in Table 4.1, which are confirmed by the familiar log-log plots. Compared to the equilibrium critical temperature reported by Smit and Frenkel [89], one has that $T_0/T_\infty \approx 1.46$, i.e., the change is opposite to the one for the DLG [11]. This confirms the observation above that the field acts in the nonequilibrium LJ system favoring disorder.

The fact that the order-parameter critical exponent is relatively small may already be guessed by noticing the extremely flat coexistence curve in Fig. 4.11. This is similar to the corresponding curve for the equilibrium two-dimensional LJ fluids [89, 117, 118], and it is fully consistent with the equilibrium Onsager value, $\beta = 1/8$. We therefore believe that our model belongs to the Ising universality class. In any case, although the error bar is large, one may discard with confidence both the DLG value $\beta \approx 1/3$ as well as the mean field value $\beta = 1/2$ —both cases would produce a hump visible to the naked eye in a plot such as the one in Fig. 4.11. One may argue that this result is counterintuitive, as our model *apparently* has the short-range interactions and symmetries that are believed to characterize the DLG. Further understanding for this difference will perhaps come from the statistical field theory.

⁵The first term of a Wegner-type expansion [116].

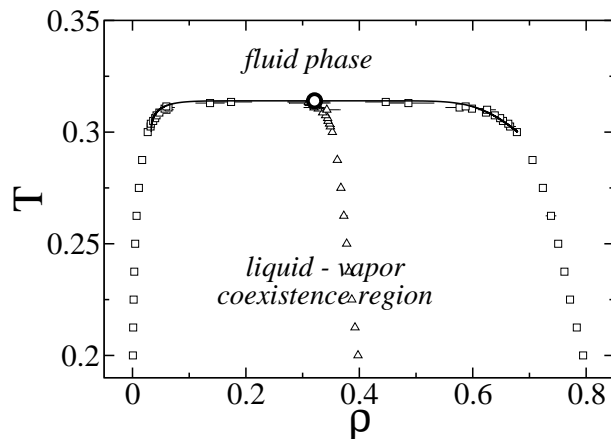


Figure 4.11: Coexistence curve (squares) for the LJ nonequilibrium model obtained from the density profiles in Fig. 4.10. The fluid phase and the coexistence region are indicated. The triangles are the arithmetic mean points, which serve to compute the critical parameters. The large circle at the top of the curve locates the critical point, and the solid line is a fit using the Wegner expansion and the rectilinear diameter law with the critical parameters given in Table 4.1.

4.4 Conclusions

In summary, the present (non-equilibrium) Lennard-Jones system, in which particles are subject to a constant driving field, has two main general features. On the one hand, this case is more convenient for computational purposes, than others such as, for instance, standard molecular-dynamics realizations of driven fluid systems. On the other hand, it seems to contain the necessary essential (microscopic) physics to be useful as a prototypical model for anisotropic behavior in nature.

This model is the natural extension to nonequilibrium anisotropic cases of the Lennard-Jones model which has played an important role in analysing equilibrium fluids. For zero field, it reduces to the familiar LJ fluid. Otherwise, it exhibits some arresting behavior, including currents and striped patterns. We have identified a process which seem to dominate early nucleation before anisotropic spinodal decomposition sets in. Interesting enough, they seem to be identical to the ones characterizing a similar situation in equilibrium. Surprisingly, we have also found that the model critical behavior is consistent with the Ising one for $d = 2$, i.e., $\beta \approx 1/8$, but not with the critical behavior of the *driven lattice gas*, i.e., $\beta \approx 1/3$. This is puzzling. Moreover, this result is quantitatively similar to the one in a related driven lattice system. Szolnoki and Szabó [91] showed that assuming nearest-neighbor *repulsion* under a driving field [93] and extending the dynamics to next-nearest-neighbor hops, the order-disorder transition which the model undergoes becomes second order for all drive, and

belongs to the Ising universality class. Furthermore, it is straightforward to see that if one allows particles' spatial coordinates to vary continuously then the model reduces to a *hard-disks* gas under a driving field, and the second order phase transition vanishes. The transition becomes similar to the melting transition for systems in equilibrium, which is described by the KTHNY scenario [119]. The fact that in both nonequilibrium diffusive models—which share similar dynamics—the critical behavior is consistent with Ising is rather surprising. For instance, using bare arguments of statistical field theory, symmetries seem to bring our system closer to the nonequilibrium lattice model (the DLG) than to the corresponding equilibrium case (the LJ fluid).

Therefore, a principal conclusion is that—regarding the modeling of complex systems—spatial discretization may change significantly not only morphological properties, but also critical properties. This is in contrast with the concept of universality in equilibrium systems, where critical properties are independent of dynamic details. The main reason for this disagreement might be the particle-hole symmetry violation in the driven *Lennard-Jones* fluid. However, to determine exactly this statement will require further study.

In any case, the additional freedom of the present, off-lattice system, which in particular implies that the particle-hole symmetry which occurs in lattice models is violated—which induces the coexistence-curve asymmetry in Fig. 4.11 in accordance with actual systems—are likely to matter more than suggested by some naive intuition. Indeed, the question of what are the most relevant ingredients and symmetries which determine unambiguously the universal properties in driven diffusive fluids is still open. Nevertheless, the above important difference between the lattice and the off-lattice cases results most interesting as an unquestionable nonequilibrium effect; as it is well known, such microscopic detail is irrelevant to universality concerning equilibrium critical phenomena.

Future investigations should address the development of a field theoretical description which shed light on the critical behavior of these models. Off-lattice models pose a new challenge for any available Langevin-type approach in which to test their viability. In principle, the *anisotropic diffusive system* approach described in the previous Chapter seems to be more appropriate because of it allows for considering the microscopic dynamical details. In fact, it is expected that a careful analysis in the derivation process from the master equation to the final Langevin equation should revail to identify the mechanisms that lead to Ising behavior.

Further study of the present nonequilibrium LJ system and its possible variations is suggested. A principal issue to be investigated is the apparent fact that the full nonequilibrium situations of interest can be described by some rather straightforward extension of equilibrium theory. We here deal with some indications of this concerning early nucleation and properties of the coexistence curve. No doubt it would be interesting to compare more systematically the behavior of models against the varied phenomenology which was already reported for anisotropic fluids. This should also help a better understanding of nonequilibrium critical phenomena.

Finally, one of our main aims at proposing this model has been motivate further research, both experimental and theoretical: we try to motivate new experiments on anisotropic decomposition besides theoretical work. In fact, our observations on the early-time separation process and structural properties are easily accessible by micro calorimetric and spectroscopy experiments, for instance.

Part II

Driven Granular Gases

Chapter 5

Introduction

The second part of this thesis focuses on *rapid granular flows*, also referred as *granular gases* [120, 121, 122, 123, 124]. They are granular systems fluidized by the application of an external driving, e.g., by mechanical vibration [39, 44], shear [125], electrostatically [126], or others means [41, 127]. In these systems, collisions between particles are considered nearly instantaneous compared with the mean free time. In fact, it is assumed (by definition) that the flow is governed by binary collisions—as in molecular gases—, whereas three-body (or more) collisions are neglected. Instead of moving in many-particle blocks, each particle moves freely and independently of even its nearest neighbors. Furthermore, granular gases exhibit many states and instabilities, e.g., convection [48, 49, 128], that characterize molecular gases. In spite of these similarities with classical molecular fluids, there are significant differences between both which make granular gases strikingly different. The origin of differences lies, as noted in the general introduction (Chapter 1), in the inelastic character of collisions between grains, and in the irrelevance of the thermal energy $k_B T$.

One important coarse-grained (continuum) approach to modeling granular gases is hydrodynamics. Granular hydrodynamics has a great predictive power and looks ideally suitable for a description of large-scale—long-wavelength and long-time— patterns observed in rapid granular flows as, for instance, a plethora of clustering phenomena [43, 44, 129, 130], vortices [37, 131, 132], oscillons [39, 133], and shocks [134]. This approach consists on a set of partial differential equations for the velocity $\mathbf{v}(\mathbf{r}, t)$, temperature $T(\mathbf{r}, t)$ (average fluctuation kinetic energy), pressure $p(\mathbf{r}, t)$, and density (or number density $n(\mathbf{r}, t)$) $\rho(\mathbf{r}, t)$ fields. Hydrodynamic equations are analogous to the Navier Stokes equations for molecular fluids, but include a sink term in the energy equation which accounts for dissipation in collisions. For two-dimensional granular fluids, these

read

$$\begin{aligned} \frac{\partial n}{\partial t} + \nabla \cdot (n\mathbf{v}) &= 0 && \text{mass conservation,} \\ n \left(\frac{\partial \mathbf{v}}{\partial t} + (\mathbf{v} \cdot \nabla) \mathbf{v} \right) &= \nabla \cdot \mathbf{p} + n\mathbf{g} && \text{momentum conservation,} \\ n \left(\frac{\partial T}{\partial t} + (\mathbf{v} \cdot \nabla) T \right) &= -\nabla \cdot \mathbf{w} + \mathbf{p} : \nabla \mathbf{v} - I && \text{energy conservation.} \end{aligned} \quad (5.1)$$

Here, \mathbf{p} is the stress tensor, \mathbf{w} is the heat flux, I is the rate of energy loss by collisions per unit area per unit time, and \mathbf{g} is an external force acting on the particles. Under some assumptions, more fundamental *kinetic theory* validates these equations and supplies constitutive relations¹ [135, 136, 137]. However, the exact criteria for the validity of (granular) kinetic theory and Navier–Stokes hydrodynamics [135, 138, 139] is still lacking. This is because first-principle derivations of universally applicable *continuum* theory of granular gas is not a simple task, even in the dilute limit. Unfortunately, the drastic simplification, provided by the binary collisions assumption, is far from sufficient for a derivation of hydrodynamics, and additional hypothesis are needed. Assuming a hard-disks system, and that the random motion of even neighboring particles are uncorrelated (*molecular chaos* assumption or *stosszahlansatz*) allows for derivations from the Boltzmann or Chapman-Enskog kinetic equation, properly generalized to account for the inelasticity of the particle collisions. An important additional assumption, made in the process of the derivation of hydrodynamics from the Chapman-Enskog equation, is scale separation [124]. Hydrodynamics demands (for inhomogeneous and/or unsteady) flows that the mean free path of the particles is much less than any characteristic length scale, and the mean free time between two consecutive collisions be much less than any characteristic time scale, aimed to be described hydrodynamically. All of these hypothesis are justified for moderate densities and for not too large inelasticity. These should be verified, in every specific system, after the hydrodynamic problem is solved and the characteristic length and time scales determined. In such case, systematic derivations of the constitutive relations—the equation of state and transport coefficients—of granular hydrodynamics from the Boltzmann or Enskog equation [140, 141, 142] use an expansion in the Knudsen number and, in some versions of theory, in inelasticity [140].

A finite inelasticity immediately brings complications [124]. Correlations between particles, developing already at a moderate inelasticity, may invalidate the molecular chaos hypothesis [143]. The correlations become stronger as the inelasticity of the collisions increases. The normal stress difference and deviations of the particle velocity distribution from the Maxwell distribution also become important for inelastic collisions. As a result, the Navier-Stokes granular hydrodynamics should not be expected to be quantitatively accurate beyond the limit of small inelasticity. In any case, despite the severe limitations intrinsic to it, the nearly elastic case is conceptually important, just because

¹These are the explicit expressions of \mathbf{p} , \mathbf{w} , and I in terms of the basic fields n , T , and \mathbf{v} .

hydrodynamics is supposed to give here a quantitatively accurate leading order theory. This is the regime (nearly elastic collisions) considered in the following Chapters 6 and 7.

A further set of difficulties for hydrodynamics arise at large densities. In mono-disperse systems strong correlations appear, already for *elastic* hard spheres, at the disorder-order transition. As multiple thermodynamic phases may coexist there [144], a general continuum theory of hard sphere fluids, which has yet to be developed, must include, in addition to the hydrodynamic fields, an order-parameter field. Furthermore, even on a specified branch of the thermodynamic phase diagram, we do not have first-principle constitutive relations. Last but not least, kinetic theory of, for instance, a finite-density gas of elastic hard spheres in two dimensions is plagued by non-existence of transport coefficients because of the long-time tail in the velocity pair autocorrelation function [145, 146].

Another potentially important limitation of the validity of granular hydrodynamics (or, rather, of any continuum approach to rapid granular flows) is due to the noise caused by the discrete nature of particles. Noise is stronger here than in classical molecular fluids simply because the number of particles is much smaller. In addition, noise can be amplified at thresholds of hydrodynamic instabilities as found, for example, in Rayleigh-Bénard convection of classical fluids [147] or in granular gases [148]. A new challenge for theory is a quantitative account of this noise. A promising approach at small or moderate densities is “Fluctuating Granular Hydrodynamics”: a Langevin-type theory that takes into account the discrete particle noise by adding a delta-correlated (gaussian) noise terms in the momentum and energy equations, in the spirit of the Fluctuating Hydrodynamics by Landau and Lifshitz [149, 150]. At high densities, however, such a theory is again beyond reach.

An alternative approach to granular flows, besides experiments, are simulations. Computer simulations have a valuable role in providing essentially exact results for certain problems which would otherwise be intractable. In addition, simulations help us to obtain the intuition we need in order to understand the complex behavior exhibited by granular material. Here (Chapters 6 and 7), we test the predictions from the hydrodynamic equations by comparing with *Molecular Dynamics* simulations [51, 88, 151]. Molecular Dynamics is a technique for computing the steady state and transport properties of a many-body system. This is in many respects very similar to real experiments. The general idea is simple: integrate numerically the microscopic equations of motion (Newton’s equations²) simultaneously for all particles ($1 \leq i \leq N$)

$$m_i \frac{d^2 \mathbf{r}_i}{dt^2} = \mathbf{F}_i(\mathbf{r}_1, \dots, \mathbf{r}_N, \mathbf{v}_1, \dots, \mathbf{v}_N) \quad (5.2)$$

This type of Molecular Dynamics is called *force-based*. However, there are systems in which this scheme is very inefficient (although, of course, still applicable)

²Typically, because of the macroscopic size of grains, quantum effects can be discarded with confidence.

[51]. In systems where most of the time each of particles propagates along a ballistic trajectory, the typical duration of a collision is much shorter than the mean time between successive collisions of a particle, i.e., binary collisions can be assumed. This is, in fact, what occurs in rapid granular flows. In such a case, if the post-collisional velocities are obtained from the pre-collisional velocities a *event-driven* Molecular Dynamics simulation can be set up³. As a result, event-driven algorithms are much more efficient, in the sense of simulation speed, than force-based algorithms (integrating directly Eq. 5.2). We will employ event-driven molecular dynamic simulations to test the validity of hydrodynamic prediction in the following chapters.

A standard prototypical model for driven granular gases, employed in many theories and simulations, as well as in experiments, is that of a monodisperse collection of uniform frictionless hard spheres (hard disks in two-dimensions) whose collisions are characterized by constant normal restitution coefficient μ_{\perp} ⁴. Usually, this model is employed to study dense or diluted flows, with or without gravity, and with or without an interstitial fluid. Here the tangential degrees of freedom are neglected, i.e., $\mu_{\parallel} = 1$, and only the normal restitution coefficient μ_{\perp} appears. However, it is worth mentioning that these two assumptions are ill-suited (see a nice discussion in [51]). This simplification is owed exclusively to the huge theoretical complication which comes along with the incorporation of the correct (velocity dependent) tangential restitution coefficient. More complex models may involve nonspherical particles, in general, irregularly shaped particles, and are also polydisperse. In addition, except for astrophysical studies [122] or experiments performed in vacuum [39] the grains are embedded in an ambient fluid. Nonetheless, the effect of a interstitial fluid, as air or water, can be sometimes neglected in determining many properties of the system [120]. This is particularly true when grain-grain interactions are stronger than fluid or grain-fluid interactions. But as the level of detail increases so does the computational effort. In spite of its shortcomings as a practical tool, the hard-spheres prototype enables the elucidation of many essential features which are the responsible for the observed macroscopic behavior.

Regarding the mechanism which drives the particles, in Chapters 6 and 7 we consider rapidly vibrating boundaries. We will assume that the characteristic frequency of vibration of the wall is much larger than the collision rate of the grains. This guarantees the absence of correlations between successive collisions of particles with the vibrating wall. In addition, it will be assumed that the amplitude of the vibration is much smaller than the mean free path of the particles, so collective motions in the system are avoided. Therefore, the vibrated wall can be represented as a hydrodynamic heat flux, i.e., as a “*thermal*” wall. From a computational point of view, the thermal wall is implemented as follows:

³There are previous works in which event-driven algorithms has been even applied to dense granular systems [130].

⁴The restitution coefficient typically depends weakly on the velocity, but using a constant simplifies the theoretical derivations greatly [51].

whenever a particle collides with the wall, it forgets its velocity and chooses a new one from a Maxwell distribution according to a certain, previously prescribed temperature T . It is important to notice that in order to avoid that the gas approaches the incorrect final temperature, the random normal velocities have to be chosen according to the probability distribution

$$N(v_n) = \frac{m}{T} v_n \exp \left[-\frac{mv_n^2}{2T} \right], \quad (5.3)$$

and the tangential velocities have to be determined from

$$N(v_t) = \sqrt{\frac{m}{2\pi T}} \exp \left[-\frac{mv_t^2}{2T} \right]. \quad (5.4)$$

See *e.g.* Ref. [51], pages 173-177, for detail.

The first simulation of a system of particles colliding inelastically and driven by a side thermal wall was considered, in one dimension, by Du, Li, and Kadanoff [152]. For typical initial conditions, the system in Ref. [152] evolves to a state where the particles are separated into two groups. Almost all particles form a low-temperature cluster in a small region, while a few remaining particles move with high velocities. Clearly, this steady state cannot be described by granular hydrodynamics. The results in Ref. [152] brought into question the validity of granular hydrodynamics in general. Nevertheless, some results [153, 154] have showed that this “anomaly” seems to vanish in higher dimensions (our studies developed in Chapters 6 and 7 concern two-dimensional systems). Therefore, the validity of hydrodynamics merits further studies.

Chapter 6

Phase separation of a driven granular gas in annular geometry

In this chapter we address phase separation of a monodisperse gas of inelastically colliding hard disks confined in a two-dimensional annulus, the inner circle of which represents a “thermal wall”. When described by granular hydrodynamic equations, the basic steady state of this system is an azimuthally symmetric state of increased particle density at the exterior circle of the annulus. When the inelastic energy loss is sufficiently large, hydrodynamics predicts spontaneous symmetry breaking of the annular state, analogous to the van der Waals-like phase separation phenomenon previously found in a driven granular gas in rectangular geometry. At a fixed aspect ratio of the annulus, the phase separation involves a “spinodal interval” of particle area fractions, where the gas has negative compressibility in the azimuthal direction. The heat conduction in the azimuthal direction tends to suppress the instability, as corroborated by a marginal stability analysis of the basic steady state with respect to small perturbations. To test and complement our theoretical predictions we performed event-driven molecular dynamics simulations of this system. We clearly identify the transition to phase separated states in the simulations, despite large fluctuations present, by measuring the probability distribution of the amplitude of the fundamental Fourier mode of the azimuthal spectrum of the particle density. We find that the instability region, predicted from hydrodynamics, is always located within the phase separation region observed in the simulations. This implies the presence of a binodal (coexistence) region, where the annular state is metastable.

6.1 Introduction

This chapter deal with a simple model of *rapid* granular flows, also referred to as granular gases: large assemblies of inelastically colliding hard spheres [120, 121, 122, 123, 124, 155]. In the simplest version of this model the only dissipative effect taken into account is a reduction in the relative normal velocity of the two colliding particles, modeled by the coefficient of normal restitution, see below.

As we explained in the previous chapter, under some assumptions a hydrodynamic description of granular gases becomes possible. In short, the molecular chaos assumption allows for a description in terms of the Boltzmann or Enskog equations, properly generalized to account for the inelasticity of particle collisions, followed by a systematic derivation of hydrodynamic equations [140, 141, 142], and for inhomogeneous flows hydrodynamics demands also scale separation. The implications of these conditions can be usually seen only *a posteriori*, after the hydrodynamic problem in question is solved, and the hydrodynamic length/time scales are determined.

We will restrict ourselves in this chapter (and also in Chapter 7) to nearly elastic collisions and moderate gas densities where, based on previous studies, hydrodynamics is expected to be an accurate leading order theory. Though quite restrictive, these assumptions allow for a detailed quantitative study (and, quite often, prediction) of a variety of pattern formation phenomena in granular gases. One of these phenomena is the phase separation instability [128, 148, 156, 157, 158, 159, 160] that was first predicted from hydrodynamics and then observed in molecular dynamic simulations. This instability arises already in a very simple, indeed prototypical setting: a monodisperse granular gas at zero gravity confined in a rectangular box, one of the walls of which is a “thermal” wall. The basic state of this system is the stripe state. In the hydrodynamic language it represents a laterally uniform stripe of increased particle density at the wall opposite to the driving wall. The stripe state was observed in experiment [129], and this and similar settings have served for testing the validity of quantitative modeling [152, 153, 154]. It turns out that (i) within a “spinodal” interval of area fractions and (ii) if the system is sufficiently wide in the lateral direction, the stripe state is unstable with respect to small density perturbations in the lateral direction [128, 158, 159]. Within a broader “binodal” (or coexistence) interval the stripe state is stable to small perturbations, but unstable to sufficiently large ones [156, 160]. In both cases the stripe gives way, usually via a coarsening process, to coexistence of dense and dilute regions of the granulate (granular “droplets” and “bubbles”) along the wall opposite to the driving wall [156, 157, 160]. This far-from-equilibrium phase separation phenomenon is strikingly similar to a gas-liquid transition as described by the classical van der Waals model, except for large fluctuations observed in a broad region of aspect ratios around the instability threshold [148]. The large fluctuations have not yet received a theoretical explanation.

This chapter addresses a phase separation process in a different geometry. We will deal here with an assembly of hard disks at zero gravity, colliding inelas-

tically inside a two-dimensional annulus. The interior wall of the annulus drives the granulate into a non-equilibrium steady state with a (hydrodynamically) zero mean flow. Particle collisions with the exterior wall are assumed elastic. The basic steady state of this system, as predicted by hydrodynamics, is the *annular* state: an azimuthally symmetric state of increased particle density at the exterior wall. The phase separation instability manifests itself here in the appearance of dense clusters with broken azimuthal symmetry along the exterior wall. Our main objectives are to characterize the instability and compute the phase diagram by using granular hydrodynamics (or, more precisely, granular hydrostatics, see below) and event driven molecular dynamics simulations. By focusing on the annular geometry, we hope to motivate experimental studies of the granular phase separation which may be advantageous in this geometry. The annular setting avoids lateral side walls (with an unnecessary/unaccounted for energy loss of the particles). Furthermore, driving can be implemented here by a rapid rotation of the (slightly eccentric and possibly rough) interior circle¹.

We organized the chapter as follows. Section 6.2 deals with a hydrodynamic description of the annular state of the gas, which is completely described by three dimensionless parameters: the grain area fraction, the inelastic heat loss parameter, and the aspect ratio. As we will be dealing only with states with a zero mean flow, we will call the respective equations hydrostatic.

A marginal stability analysis predicts a spontaneous symmetry breaking of the annular state. We compute the marginal stability curves and compare them to the borders of the spinodal (negative compressibility) interval of the system. In Section 6.3 we report event-driven molecular dynamics simulations of this system and compare the simulation results with the hydrostatic theory. In Section 6.4 we summarize the main results.

6.2 Particles in an annulus and granular hydrostatics

6.2.1 The density equation

Let N hard disks of diameter d and mass $m = 1$ move, at zero gravity, inside an annulus of aspect ratio $\Omega = R_{\text{ext}}/R_{\text{int}}$, where R_{ext} is the exterior radius and R_{int} is the interior one. The disks undergo inelastic collisions with a constant coefficient of normal restitution μ . For simplicity, we neglect the rotational degree of freedom of the particles. In each inter-particle collision the kinetic energy is continuously transferred into heat, while the momentum is conserved. The (driving) interior wall is modeled by a thermal wall kept at temperature T_0 , whereas particle collisions with the exterior wall are considered elastic. The energy transferred from the thermal wall to the granulate dissipates in the particle inelastic collisions, and we assume that the system reaches a (non-equilibrium)

¹It is worth notice that the posed setting resembles morphology and dynamical processes in planetary rings [161], where clustering, spontaneous symmetry breaking, and oscillatory instabilities, between many others, also may occur.

steady state with a zero mean flow. We restrict ourselves to the nearly elastic limit by assuming a restitution coefficient close to, but less than, unity: $1 - \mu \ll 1$. This allows us to safely use granular hydrodynamics [124]. For a zero mean flow steady state the continuity equation is obeyed trivially, while the momentum and energy equations yield two *hydrostatic* relations:

$$\nabla \cdot \mathbf{w}(\mathbf{r}) + I = 0, \quad p = \text{const}, \quad (6.1)$$

where \mathbf{w} is the local heat flux, I is the energy loss term due to inelastic collisions, and $P = P(\mathbf{n}, T)$ is the gas pressure that depends on the number density $\mathbf{n}(\mathbf{r})$ and granular temperature $T(\mathbf{r})$. Despite the inelastic collisions, if the macroscopic field gradients are not very large, it seems natural to postulate linear relation between fluxes and “thermodynamic” forces. Then, we adopt the classical Fourier relation for the heat flux $\mathbf{w}(\mathbf{r}) = -\kappa \nabla T(\mathbf{r})$ (where κ is the thermal conductivity), omitting a density gradient term $\gamma \nabla \mathbf{n}(\mathbf{r})$. In the dilute limit this term was derived in Ref. [141]. It can be neglected in the nearly elastic limit which is assumed throughout the second part of this thesis.

The momentum and energy balance equations read

$$\nabla \cdot [\kappa \nabla T(\mathbf{r})] = I, \quad p = \text{const}, \quad (6.2)$$

To get a closed formulation, we need constitutive relations for $p(\mathbf{n}, T)$, $\kappa(\mathbf{n}, T)$ and $I(\mathbf{n}, T)$. We will employ the widely used semi-empiric transport coefficients derived by Jenkins and Richman [135] from the Enskog kinetic equation, generalized to account for inelastic collision losses, for moderate densities:

$$\begin{aligned} \kappa &= \frac{2d\mathbf{n}T^{1/2}\tilde{G}}{\pi^{1/2}} \left[1 + \frac{9\pi}{16} \left(1 + \frac{2}{3\tilde{G}} \right)^2 \right], \\ I &= \frac{8(1-\mu)\mathbf{n}T^{3/2}\tilde{G}}{d\sqrt{\pi}}, \end{aligned} \quad (6.3)$$

and the equation of state first proposed by Carnahan and Starling [162]

$$p = \mathbf{n}T(1 + 2\tilde{G}), \quad (6.4)$$

where $\tilde{G} = \nu(1 - \frac{7\nu}{16})/(1 - \nu)^2$ and $\nu = \mathbf{n}(\pi d^2/4)$ is the solid fraction. Let us rescale the radial coordinate by R_{int} and introduce the rescaled inverse density $Z(r, \theta) = \mathbf{n}_c/\mathbf{n}(r, \theta)$, where $\mathbf{n}_c = 2/(\sqrt{3}d^2)$ is the hexagonal close packing density. The rescaled radial coordinate r now changes between 1 and $\Omega \equiv R_{\text{ext}}/R_{\text{int}}$, the aspect ratio of the annulus. As in the previous work [128], Eqs. (6.2), (6.4) and (6.3) can be transformed into a single equation for the inverse density $Z(r)$:

$$\nabla \cdot [\mathcal{F}(Z)\nabla Z] = \Lambda \mathcal{Q}(Z), \quad (6.5)$$

where

$$\begin{aligned}
\mathcal{F}(Z) &= \mathcal{F}_1(Z)\mathcal{F}_2(Z), \\
\mathcal{Q}(Z) &= \frac{6}{\pi} \frac{Z^{1/2}\mathcal{G}}{(1+2\mathcal{G})^{3/2}}, \\
\mathcal{F}_1(Z) &= \frac{\mathcal{G}(Z) \left[1 + \frac{9\pi}{16} \left(1 + \frac{2}{3\mathcal{G}} \right)^2 \right]}{Z^{1/2}(1+2\mathcal{G})^{5/2}}, \\
\mathcal{F}_2(Z) &= 1 + 2\mathcal{G} + \frac{\pi}{\sqrt{3}} \frac{Z \left(Z + \frac{\pi}{16\sqrt{3}} \right)}{\left(Z - \frac{\pi}{2\sqrt{3}} \right)^3}, \\
\mathcal{G}(Z) &= \frac{\pi}{2\sqrt{3}} \frac{\left(Z - \frac{7\pi}{32\sqrt{3}} \right)}{\left(Z - \frac{\pi}{2\sqrt{3}} \right)^2}.
\end{aligned} \tag{6.6}$$

The dimensionless parameter $\Lambda \equiv (2\pi/3)(1-\mu)(R_{\text{int}}/d)^2$ is the hydrodynamic inelastic loss parameter. The boundary conditions for Eq. (6.5) are

$$\partial Z(1, \theta)/\partial \theta = 0 \quad \text{and} \quad \nabla_n Z(\Omega, \theta) = 0, \tag{6.7}$$

The first of these follows from the constancy of the temperature at the (thermal) interior wall which, in view of the constancy of the pressure in a steady state, becomes constancy of the density. The second condition demands a zero normal component of the heat flux at the elastic wall. Notice that neither the pressure nor the temperature at the thermal wall enter in Eqs. (6.5)-(6.7) [159, 128]. This is a consequence of the fact that the hard-core interactions between particles does not introduce a characteristic energy scale. The temperature only sets the temperature scale in the system and affects the pressure, which is constant in the steady state problem. Finally, working with a fixed number of particles, we demand the normalization condition

$$\int_0^{2\pi} \int_1^\Omega Z^{-1}(r, \theta) r dr d\theta = \pi f (\Omega^2 - 1), \tag{6.8}$$

where

$$f = \frac{N}{\pi n_c R_{\text{int}}^2 (\Omega^2 - 1)}$$

is the area fraction of the grains in the annulus. Equations (6.5)-(6.8) determine all possible steady state density profiles, governed by three dimensionless parameters: f , Λ , and Ω .

6.2.2 Annular state

The simplest solution of the density equation (6.5) is azimuthally symmetric (θ -independent): $Z = z(r)$. Henceforth we refer to this basic state of the system

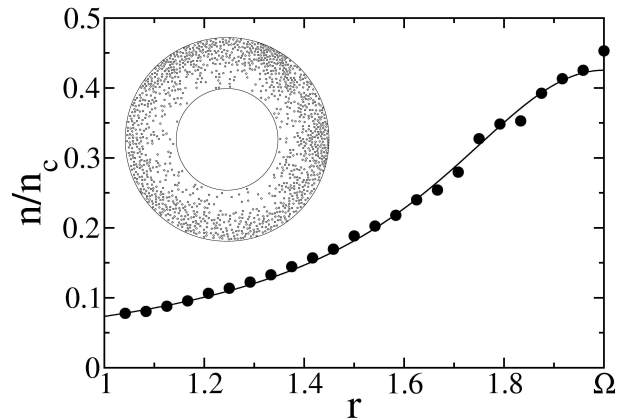


Figure 6.1: The normalized density profiles obtained from the molecular dynamics simulations (the dots) and hydrostatics (the line) for $\Omega = 2$, $\Lambda = 81.09$, and $f = 0.356$ (equivalently, $z_\Omega = 2.351$). The simulations were carried out with $N = 1250$ particles, $\mu = 0.92$, and $R_{\text{int}} = 22.0$. Also shown is a typical snapshot of the system at the steady state as observed in the simulation.

as the *annular state*. It is determined by the following equations:

$$[r\mathcal{F}(z)z']' = r\Lambda Q(z), \quad z'(\Omega) = 0, \quad \text{and} \quad \int_1^\Omega z^{-1} r dr = (\Omega^2 - 1)f/2, \quad (6.9)$$

where the primes denote r -derivatives. In order to solve the second order equation (6.9) numerically, one can prescribe the inverse density at the elastic wall $z_\Omega \equiv z(\Omega)$. Combined with the no-flux condition at $r = \Omega$, this condition defines a Cauchy problem for $z(r)$ [157, 128]. Solving the Cauchy problem, one can compute the respective value of f from the normalization condition in Eq. (6.9). At fixed Λ and Ω , there is a one-to-one relation between z_Ω and f . Therefore, an alternative parameterization of the annular state is given by the scaled numbers z_Ω , Λ , and Ω . The same is true for the marginal stability analysis performed in the next subsection.

Figure 6.1 depicts an example of annular state that we found numerically. One can see that the gas density increases with the radial coordinate², as expected from the temperature decrease via inelastic losses (the velocities of the particles decrease), combined with the constancy of the (hydrodynamic) pressure throughout the system. The hydrodynamic density profile agrees well with the one found in our simulations, see below.

²See Refs. [42, 43, 157, 163] for clustering instability.

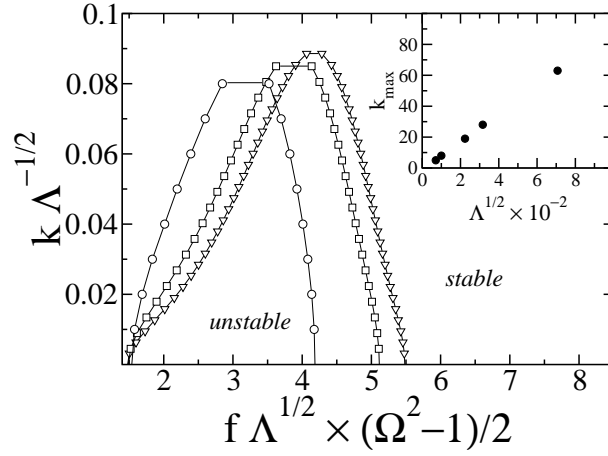


Figure 6.2: The main graph: the marginal stability curves $k = k(f)$ (where k is an integer) for $\Omega = 1.5$ and $\Lambda = 10^4$ (circles), $\Lambda = 5 \times 10^4$ (squares), and $\Lambda = 10^5$ (triangles). For a given Λ the annular state is stable above the respective curve and unstable below it, as indicated for $\Lambda = 10^4$. As Λ increases the marginal stability interval shrinks. The lines connecting dots serve to guide the eye. The inset: the dependence of k_{\max} on $\Lambda^{1/2}$. The straight line shows that, at large Λ , $k_{\max} \propto \Lambda^{1/2}$.

6.2.3 Phase separation

Mathematically, phase separation manifests itself in the existence of *additional* solutions to Eqs. (6.5)-(6.8) in some region of the parameter space f , Λ , and Ω . These additional solutions are *not* azimuthally symmetric³. Solving Eqs. (6.5)-(6.8) for fully two-dimensional solutions is not easy [159]. One class of such solutions, however, bifurcate continuously from the annular state, so they can be found by linearizing Eq. (6.5), as in rectangular geometry [159, 128]. In the framework of a time-dependent hydrodynamic formulation, this analysis corresponds to a *marginal stability* analysis which involves a small perturbation to the annular state. For a single azimuthal mode $\sim \sin(k\theta)$ (where k is integer) we can write $Z(\mathbf{r}, \theta) = z(\mathbf{r}) + \varepsilon \Xi(\mathbf{r}) \sin(k\theta)$, where $\Xi(\mathbf{r})$ is a smooth function, and $\varepsilon \ll 1$ a small parameter. Substituting this into Eq. (6.5) and linearizing the resulting equation yields a k -dependent second order differential equation for the function $\Gamma(\mathbf{r}) \equiv \mathcal{F}[Z(\mathbf{r})] \Xi(\mathbf{r})$:

$$\Gamma_k'' + \frac{1}{r} \Gamma_k' - \left(\frac{k^2}{r^2} + \frac{\Lambda Q'(Z)}{\mathcal{F}(Z)} \right) \Gamma_k = 0. \quad (6.10)$$

This equation is complemented by the boundary conditions

$$\Gamma(1) = 0 \quad \text{and} \quad \Gamma'(\Omega) = 0. \quad (6.11)$$

³As we shall show in Section 6.3, such instability also is observed in simulations.

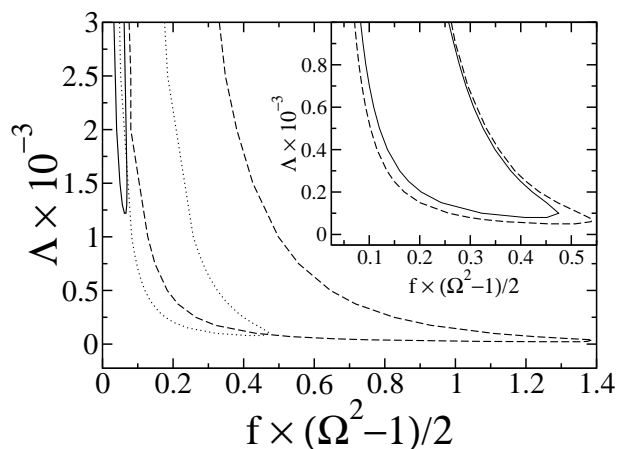


Figure 6.3: Two-dimensional projections on the Λ - f plane of the phase diagram at $\Omega = 1.5$ (the solid line), $\Omega = 3$ (the dotted line), and $\Omega = 5$ (the dashed line). The inset shows more clearly, for $\Omega = 3$, that the marginal stability curve (the solid line) lies within the negative compressibility region (depicted by the dashed line).

For fixed values of the scaled parameters f , Λ , and Ω , Eqs. (6.10) and (6.11) determine a linear eigenvalue problem for k . Solving this eigenvalue problem numerically, one obtains the marginal stability hypersurface $k = k(f, \Lambda, \Omega)$. For fixed Λ and Ω , we obtain a marginal stability curve $k = k(f)$. Examples of such curves, for a fixed Ω and three different Λ are shown in Fig. 6.2. Each $k = k(f)$ curve has a maximum k_{\max} , so that a density modulation with the azimuthal wavenumber larger than k_{\max} is stable. As expected, the instability interval is the largest for the fundamental mode $k = 1$. The inset in Fig. 6.2 shows the dependence of k_{\max} on $\Lambda^{1/2}$. The straight line shows that, at large Λ , $k_{\max} \propto \Lambda^{1/2}$, as in rectangular geometry [128].

Two-dimensional projections of the (f, Λ, Ω) -phase diagram at three different Ω are shown in Fig. 6.3 for the fundamental mode. The annular state is unstable in the region bounded by the marginal stability curve and stable elsewhere. Therefore, the marginal stability analysis predicts loss of stability of the annular state within a finite interval of f , that is at $f_{\min}(\Lambda, \Omega) < f < f_{\max}(\Lambda, \Omega)$.

The physical mechanism of this phase separation *instability* is the negative compressibility of the granular gas in the azimuthal direction, caused by the inelastic energy loss. To clarify this point, let us compute the *pressure* of the annular state, given by Eq. (6.4). First we introduce a rescaled pressure $P = p/(n_c T_0)$ and, in view of the pressure constancy in the annular state, compute it at the thermal wall, where $T = T_0$ is prescribed and $z(1)$ is known from our

numerical solution for the annular state. We obtain

$$P(f, \Lambda, \Omega) = \frac{1 + 2\mathcal{G}(z(1))}{z(1)}.$$

The spinodal (negative compressibility) region is determined by the necessary condition for the *instability*: $(\partial P/\partial f)_{\Lambda, \Omega} < 0$, whereas the borders of the spinodal region are defined by $(\partial P/\partial f)_{\Lambda, \Omega} = 0$. That is, computing the derivative we arrive at $\partial P/\partial f = (\partial P/\partial z(1))(\partial z(1)/\partial z(\Omega))(\partial z(\Omega)/\partial f)$. One can easily check that the first and third multipliers on the righthand side of this relation are always negative, thus the sign of $(\partial P/\partial f)_{\Lambda, \Omega}$ is determined by the sign of $(\partial z(1)/\partial z(\Omega))_{\Lambda, \Omega}$.

Typical $P(f)$ curves for a fixed Ω and several different Λ are shown in Fig. 6.4. One can see that, at sufficiently large Λ , the rescaled pressure P goes down with an increase of f at an interval $f_1 < f < f_2$. That is, the effective compressibility of the gas with respect to a redistribution of the material in the azimuthal direction is negative on this interval of area fractions. By joining the spinodal points f_1 and (separately) f_2 at different Λ , we can draw the spinodal line for a fixed Ω . As Λ goes down, the spinodal interval shrinks and eventually becomes a point at a critical point (P_c, f_c) , or (Λ_c, f_c) (where all the critical values are Ω -dependent). For $\Lambda < \Lambda_c$ $P(f)$ monotonically increases and there is no instability.

What is the relation between the spinodal interval (f_1, f_2) and the marginal stability interval (f_{\min}, f_{\max}) ? These intervals would coincide were the azimuthal wavelength of the perturbation infinite (or, equivalently, $k \rightarrow 0$), so that the azimuthal heat conduction would vanish. Of course, this is not possible in annular geometry, where $k \geq 1$. As a result, the negative compressibility interval must include in itself the marginal stability interval (f_{\min}, f_{\max}) . This is what our calculations indeed show, see the inset of Fig. 6.3. That is, a negative compressibility is necessary, but not sufficient, for instability, similarly to what was found in rectangular geometry [128].

Importantly, the instability region of the parameter space is by no means not the *whole* region the region where phase separation is expected to occur. Indeed, in analogy to what happens in rectangular geometry [156, 160], phase separation is also expected in a *binodal* (or coexistence) region of the area fractions, where the annular state is stable to small perturbations, but unstable to sufficiently large ones. The whole region of phase separation should be larger than the instability region, and it should of course *include* the instability region. Though we did not attempt to determine the binodal region of the system from the hydrostatic equations (this task has not been accomplished yet even for rectangular geometry, except in the close vicinity of the critical point [160]), we determined the binodal region from our molecular dynamics simulations reported in the next section.

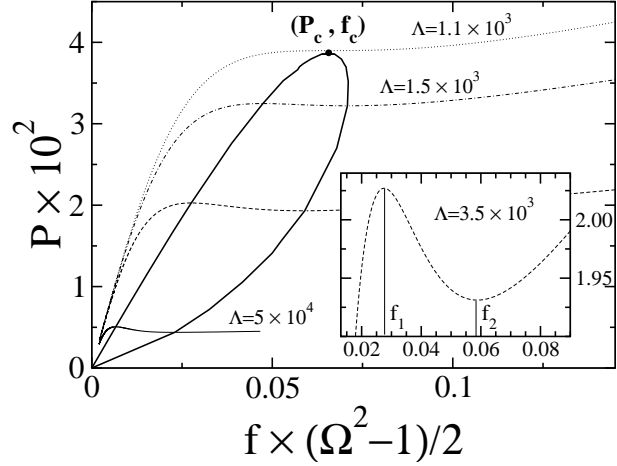


Figure 6.4: The scaled steady state granular pressure P versus the grain area fraction f for $\Omega = 1.5$ and $\Lambda = 1.1 \times 10^3$ (the dotted line), $\Lambda = 1.5 \times 10^3$ (the dash-dotted line), $\Lambda = 3.5 \times 10^3$ (dashed line), and $\Lambda = 5 \times 10^4$ (the solid line). The inset shows a zoom-in for $\Lambda = 3.5 \times 10^3$. The borders f_1 and f_2 of the spinodal interval are determined from the condition $(\partial P / \partial f)_{\Lambda, \Omega} = 0$. The thick solid line encloses the spinodal balloon where the effective azimuthal compressibility of the gas is negative.

6.3 Molecular Dynamics Simulations

6.3.1 Method

We performed a series of event-driven molecular dynamics simulations of this system using an algorithm described by Pöschel and Schwager [51] and sketched in the previous chapter. Simulations involved N hard disks of diameter $d = 1$ and mass $m = 1$. After each collision of particle i with particle j , their relative velocity is updated according to

$$\vec{v}'_{ij} = \vec{v}_{ij} - (1 + \mu) (\vec{v}_{ij} \cdot \hat{r}_{ij}) \hat{r}_{ij}, \quad (6.12)$$

where \vec{v}_{ij} is the precollisional relative velocity, and $\hat{r}_{ij} \equiv \vec{r}_{ij} / |\vec{r}_{ij}|$ is a unit vector connecting the centers of the two particles. Particle collisions with the exterior wall $r = R_{\text{ext}}$ are assumed elastic. The interior wall is kept at constant temperature T_0 that we set to unity. This is implemented as explained in Chapter 5. When a particle collides with the wall it forgets its velocity and picks up a new one from a proper Maxwellian distribution with temperature T_0 . The time scale is therefore $d(m/T_0)^{1/2} = 1$. The initial condition is a uniform distribution of non-overlapping particles inside the annular box. Their initial velocities are taken randomly from a Maxwellian distribution at temperature $T_0 = 1$. In all simulations the coefficient of normal restitution $\mu = 0.92$ and the interior radius $R_{\text{int}}/d = 22.0$ were fixed, whereas the the number of particles $527 \leq N \leq 7800$

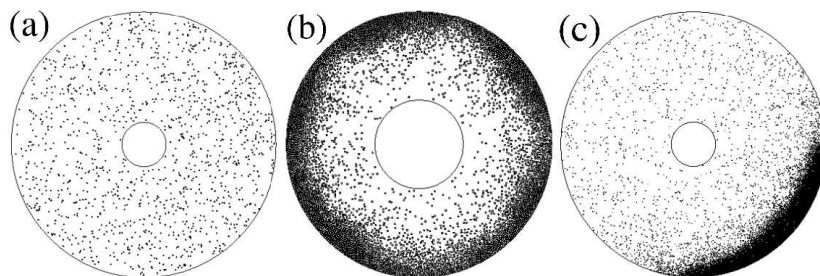


Figure 6.5: Typical steady state snapshots for $N = 1250$ and $\Omega = 6$ (a); $N = 5267$ and $\Omega = 3$ (b), and $N = 6320$ and $\Omega = 6$ (c). Panels (a) and (b) correspond to annular states of the hydrostatic theory, whereas panel (c) shows a broken-symmetry (phase separated) state.

and the aspect ratio $1.5 \leq \Omega \leq 6$ were varied. In terms of the three scaled hydrodynamic parameters the heat loss parameter $\Lambda = 81.09$ was fixed whereas f and Ω varied.

To compare the simulation results with predictions of our hydrostatic theory, all the measurements were performed once the system reached a steady state. This was monitored by the evolution of the total kinetic energy $(1/2) \sum_{i=1}^N \vec{v}_i^2$, which first decays and then, on the average, stays constant.

6.3.2 Steady States

Typical steady state snapshots of the system, observed in our molecular dynamics simulation, are displayed in Fig. 6.5. Panel (a) shows a dilute state where the radial density inhomogeneity, though actually present, is not visible by naked eye. Panels (b) and (c) do exhibit a pronounced radial density inhomogeneity. Apart from visible density fluctuations, panels (a) and (b) correspond to annular states. Panel (c) depicts a broken-symmetry (phase separated) state. When an annular state is observed, its density profile agrees well with the solution of the hydrostatic equations (6.5)-(6.8). A typical example of such a comparison is shown in Fig. 6.1.

Let us fix the aspect ratio Ω of the annulus at not too a small value and vary the number of particles N . First, what happens on a qualitative level? The simulations show that, at small N , dilute annular states, similar to snapshot (a) in Fig. 6.5, are observed. As N increases, broken-symmetric states start to appear. Well within the unstable region, found from hydrodynamics, a high density cluster appears, like the one shown in Fig. 6.5c, and performs an erratic motion along the exterior wall. As N is increased still further, well beyond the high- f branch of the unstable region, an *annular state* reappears, as in Fig. 6.5b. This time, however, the annular state is denser, while its local structure varies from a solid-like (with imperfections such as voids and line defects) to a liquid-like.

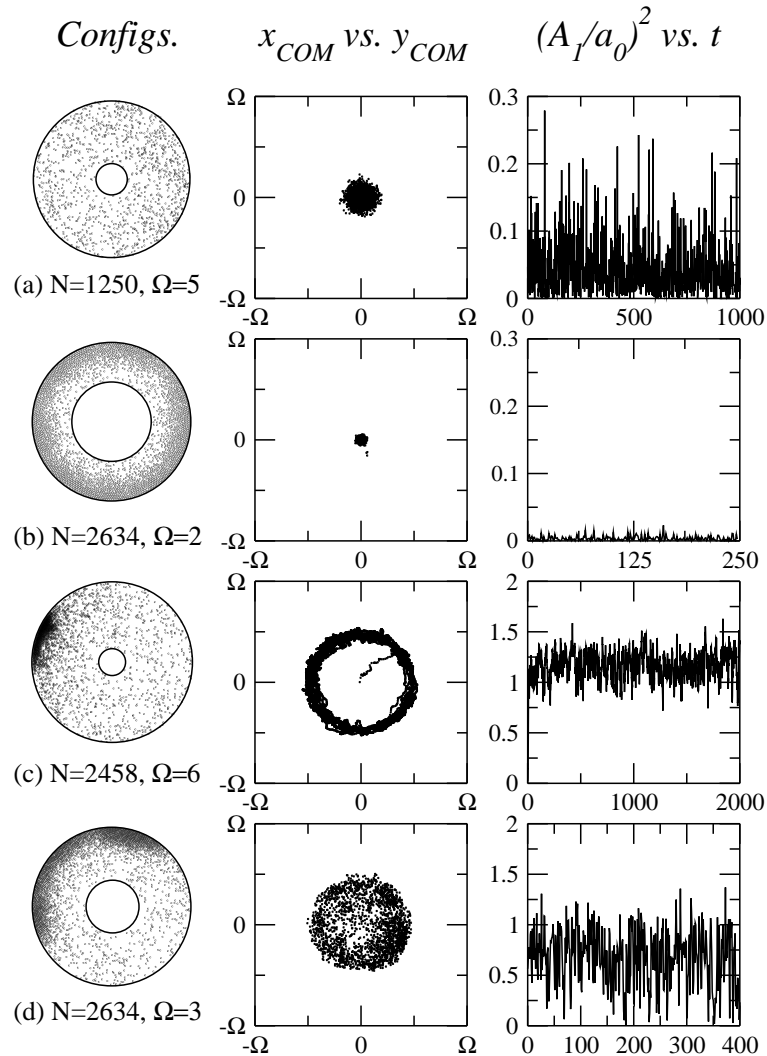


Figure 6.6: Typical steady state snapshots (the left column; particle size looks larger than it is) and the temporal evolution of the COM (the middle column) and of the squared amplitude of the fundamental Fourier mode (the right column). The temporal data are sampled each 150 collisions per particle. Each row corresponds to one simulation with the indicated parameters. The vertical scale of panels (a) and (b) was stretched for clarity.

To characterize the spatio-temporal behavior of the granulate at a steady state, we followed the position of the center of mass (COM) of the granulate. Several examples of the COM trajectories are displayed in Fig. 6.6. Here cases (a) and (b) correspond, in the hydrodynamic language, to annular states. There are, however, significant fluctuations of the COM around the center of the annulus. These fluctuations are of course not accounted for by hydrodynamic theory. In case (b), where the dense cluster develops, the fluctuations are much weaker than in case (a). More interesting are cases (c) and (d). They correspond to broken-symmetry states: well within the phase separation region of the parameter space (case c) and close to the phase separation border (case d). The COM trajectory in case (c) shows that the granular “droplet” performs random motion in the azimuthal direction, staying close to the exterior wall. This is in contrast with case (d), where fluctuations are strong both in the azimuthal and in the radial directions. Following the actual snapshots of the simulation, one observes here a very complicated motion of the “droplet”, as well as its dissolution into more “droplets”, mergers of the droplets *etc.* Therefore, as in the case of granular phase separation in rectangular geometry [148], the granular phase separation in annular geometry is accompanied by considerable spatio-temporal fluctuations. In this situation a clear distinction between a phase-separated state and an annular state, and a comparison between the simulations and hydrodynamic theory, demand proper diagnostics. We found that such diagnostics are provided by the azimuthal spectrum of the particle density and its probability distribution.

6.3.3 Azimuthal Density Spectrum

Let us consider the (time-dependent) rescaled density field $\nu(\mathbf{r}, \theta, t) = \mathbf{n}(\mathbf{r}, \theta, t)/n_c$ (where \mathbf{r} is rescaled to the interior wall radius as before), and introduce the integrated field $\hat{\nu}(\theta, t)$:

$$\hat{\nu}(\theta, t) = \int_1^{\Omega} \nu(\mathbf{r}, \theta, t) r \, dr. \quad (6.13)$$

In a system of N particles, $\hat{\nu}(\theta, t)$ is normalized so that

$$\int_0^{2\pi} \hat{\nu}(\theta, t) \, d\theta = \frac{N}{n_c R_{\text{int}}^2}. \quad (6.14)$$

Because of the periodicity in θ the function $\hat{\nu}(\theta, t)$ can be expanded in a Fourier series:

$$\hat{\nu}(\theta, t) = a_0 + \sum_{k=1}^{\infty} [a_k(t) \cos(k\theta) + b_k(t) \sin(k\theta)], \quad (6.15)$$

where a_0 is independent of time because of the normalization condition (6.14). We will work with the quantities

$$A_k^2(t) \equiv a_k^2(t) + b_k^2(t), \quad k \geq 1. \quad (6.16)$$

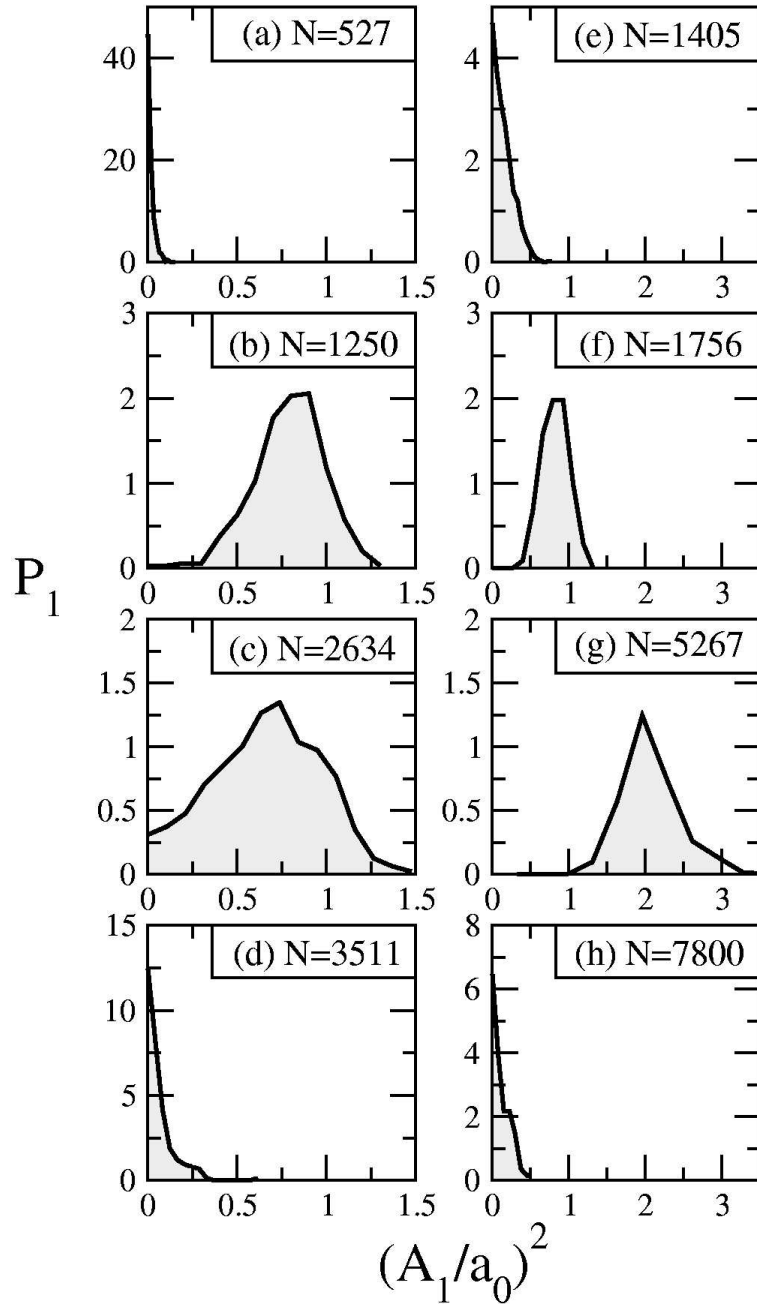


Figure 6.7: The normalized probability distribution functions $P_1 (A_1^2/a_0^2)$ for $\Omega = 3$ (the left column) and $\Omega = 5$ (the right column) at a different number of particles.

Table 6.1: The averaged squared relative amplitudes $\langle A_k^2(t) \rangle / a_0^2$ for the first three modes $k = 1, 2$ and 3 . (a) $N = 2634$, $\Omega = 3$, (b) $N = 5267$, $\Omega = 4$, (c) $N = 1000$, $\Omega = 2.25$, and (d) $N = 1250$, $\Omega = 3$.

k	(a)	(b)	(c)	(d)
1	0.66 ± 0.05	0.39 ± 0.04	0.30 ± 0.08	0.77 ± 0.05
2	0.04 ± 0.02	0.05 ± 0.02	0.07 ± 0.01	0.28 ± 0.09
3	0.03 ± 0.02	0.03 ± 0.03	0.02 ± 0.02	0.11 ± 0.08

For the (deterministic) annular state one has $A_k = 0$ for all $k \geq 1$, while for a symmetry-broken state $A_k > 0$. The relative quantities $A_k^2(t)/a_0^2$ can serve as measures of the azimuthal symmetry breaking. As is shown in Table 6.1, $A_1^2(t)$ is usually much larger (on the average) than the rest of $A_k^2(t)$. Therefore, the quantity $A_1^2(t)/a_0^2$ is sufficient for our purposes.

Once the system relaxed to a steady state, we followed the temporal evolution of the quantity A_1^2/a_0^2 . Typical results are shown in the right column of Fig. 6.6. One observes that, for annular states, this quantity is usually small, as is the cases (a) and (b) in Fig. 6.6. For broken-symmetry states A_1^2 is larger, and it increases as one moves deeper into the phase separation region. (Notice that the averaged value of A_1^2/a_0^2 in (c) is larger than in (d), which means that (c) is deeper in the phase separation region.) Another characteristics of $A_1^2(t)/a_0^2$ is the magnitude of fluctuations. One can notice that, in the vicinity of the phase separation border the fluctuations are stronger (as in case (d) in Fig. 6.6).

All these properties are encoded in the *probability distribution* P_1 of the values of $(A_1/a_0)^2$: the ultimate tool of our diagnostics. Figure 6.7 shows two series of measurements of this quantity at different N : for $\Omega = 3$ and $\Omega = 5$. By following the position of the maximum of P_1 we were able to sharply discriminate between the annular states and phase separated states and therefore to locate the phase separation border. When the maximum of P_1 occurs at the zero value of $(A_1/a_0)^2$ (as in cases (a) and (d) and, respectively, (e) and (h) in Fig. 6.7), an annular state is observed. On the contrary, when the maximum of P_1 occurs at a non-zero value of $(A_1/a_0)^2$ (as in cases (b) and (c) and, respectively, (f) and (g) in Fig. 6.7), a phase separated state is observed. In each case, the width of the probability distribution (measured, for example, at the half-maximum) yields a direct measure of the magnitude of fluctuations. Near the phase separation border, strong fluctuations (that is, broader distributions) are observed, as in case (c) of Fig. 6.7.

Using the position of the maximum of P_1 as a criterion for phase separation, we show, in Fig. 6.8, the $\Omega - f$ diagram obtained from the molecular dynamics simulations. The same figure also depicts the hydrostatic prediction of the *instability* region. One can see that the instability region is located within the phase separation region, as expected.

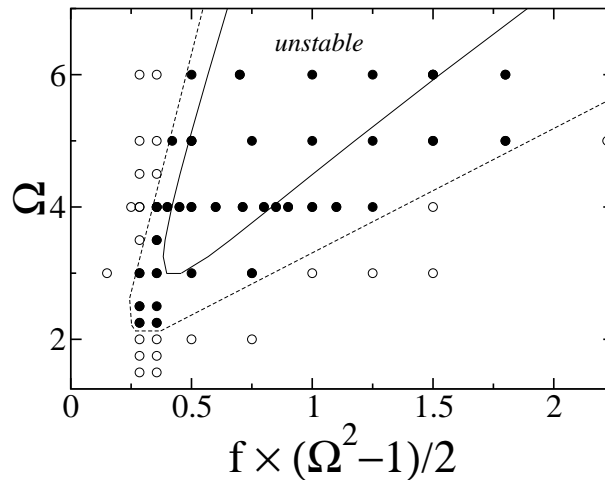


Figure 6.8: The Ω - f phase diagram for $\Lambda = 81.09$. The solid curve is given by the granular hydrostatics: it shows the borders of the region where the annular state is unstable with respect to small perturbations. The filled symbols depict the parameters in which phase separated states are observed, whereas the hollow symbols show the parameters at which annular states are observed. The dashed line is an estimated binodal line of the system.

6.4 Conclusions

We combined equations of granular hydrostatics and event-driven molecular dynamics simulations to investigate spontaneous phase separation of a monodisperse gas of inelastically colliding hard disks in a two-dimensional annulus, the inner circle of which serves as a “thermal wall”. A marginal stability analysis yields a region of the parameter space where the annular state—the basic, azimuthally symmetric steady state of the system—is unstable with respect to small perturbations which break the azimuthal symmetry. The physics of the instability is negative effective compressibility of the gas in the azimuthal direction, which results from the inelastic energy loss. Simulations of this system show phase separation, but it is masked by large spatio-temporal fluctuations. By measuring the probability distribution of the amplitude of the fundamental Fourier mode of the azimuthal spectrum of the particle density we were able to clearly identify the transition to phase separated states in the simulations. We found that the instability region of the parameter space, predicted from hydrostatics, is located within the phase separation region observed in the molecular dynamics simulations. This implies the presence of a binodal (coexistence) region, where the annular state is *metastable*, similar to what has been found in rectangular geometry [156, 160]. We hope our results will stimulate experimental work on the phase separation instability.

Finally, we have also investigated an alternative setting in which the exterior

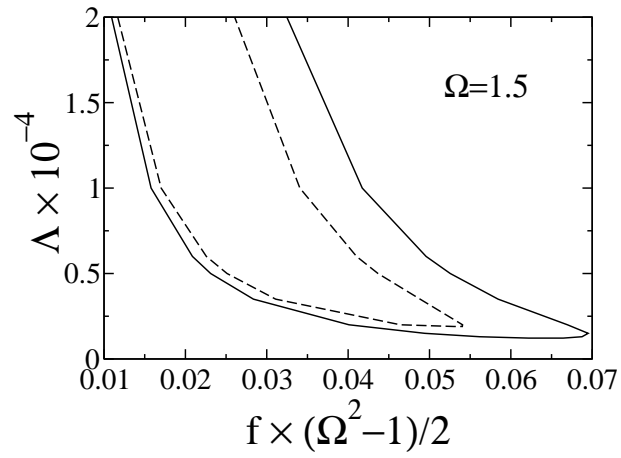


Figure 6.9: The marginal stability lines for our main setting (the solid line) and for an alternative setting in which the thermal wall is at $r = R_{ext}$ and the elastic wall is at $r = R_{int}$ (the dashed line).

wall is the driving wall, while the interior wall is elastic. The corresponding hydrostatic problem is determined by the same three scaled parameters f , Λ and Ω , but the boundary conditions must be changed accordingly. Here azimuthally symmetric clusters appear near the (elastic) interior wall. Symmetry breaking instability occurs here as well. We found very similar marginal stability curves here, but they are narrower (as shown in Fig. 6.9) than those obtained for our main setting.

Chapter 7

Close-packed granular clusters

Dense granular clusters often behave like macro-particles. We address this interesting phenomenon in a model system of inelastically colliding hard disks inside a circular box, driven by a thermal wall at zero gravity. Molecular dynamics simulations show a close-packed cluster of an almost circular shape, weakly fluctuating in space and isolated from the driving wall by a low-density gas. The density profile of the system agrees well with the azimuthally symmetric solution of granular hydrostatic equations employing constitutive relations by Grossman *et al.* We find that fluctuations of the center of mass of the system are Gaussian. This suggests an effective Langevin description in terms of a macro-particle, confined by a harmonic potential and driven by a delta-correlated noise. Surprisingly, the fluctuations persist when increasing the number of particles in the system.

7.1 Introduction

This chapter addresses granular hydrodynamics and fluctuations in a simple two-dimensional granular system under conditions when existing hydrodynamic descriptions [140, 141, 142] break down because of large density, *not* large inelasticity. In view of the difficulties mentioned in Chapters 5 and 6, attempts of a first-principle description of hydrodynamics and fluctuations should give way here to more practical, empiric or semi-empiric, approaches. One such approach to a hydrodynamic (or, rather, hydrostatic) description was suggested by Grossman *et al.* [154]. In the present chapter, we put it into a test in an extreme case when macro-particles (granular clusters with the maximum density close to the hexagonal close packing) form. The model system we are dealing with was first introduced by Esipov and Pöschel [153]. It is an assembly of $N \gg 1$ identical disks of mass m , diameter d and coefficient of normal restitution μ , placed inside a circular box of radius R at zero gravity (typical steady state

configurations are shown in Fig. 7.1). The circular wall of the box, which supply energy continuously to the granulate, is kept at constant temperature T_0 , i.e., the vibrating boundary is represented as a thermal wall (under conditions specified in Chapter 5). There are not additional external forces acting on the system.

We used a model of inelastically colliding hard disks to develop kinetic and hydrodynamic descriptions. We measure, using event-driven molecular dynamics simulations, the radial density profiles of the system, including the close-packed part. Furthermore, we solve numerically a set of granular hydrostatic equations which employ the constitutive relations by Grossman *et al.* and show that, in a wide range of parameters, there is good agreement between the two. A marginal stability analysis will show that there are no steady-state solutions with broken azimuthal symmetry which would bifurcate from the azimuthally symmetric solution. Finally, we address, for the first time, fluctuations of the macro-particles, by measuring the radial probability distribution function (PDF) of the center of mass of the system. These fluctuations turn out to be Gaussian, which suggests an effective Langevin description of the system in terms of a macro-particle, confined by a harmonic potential and driven by a white noise. Surprisingly, the fluctuations persist as the number of particles in the system is increased.

7.2 Event-driven molecular dynamics simulations

As we outlined in Chapter 2, we employed a standard event-driven molecular dynamics algorithm [51]. One of the simplest models one can employ to study flows dominated by binary particle collisions [124, 155] consists of N inelastically colliding hard disks of mass m and diameter d . Rotational degree of freedom is neglected, and thus inelasticity is modeled by the coefficient of normal restitution $\mu < 1$, which is considered constant (velocity independent). When two particles collide (say $1 \leq i, j \leq N$), their tangential velocities are unchanged, whereas the relative normal velocity is decreased. Using momentum conservation, the post-collisional velocities in terms of the pre-collisional read

$$\begin{aligned}\vec{v}'_i &= \vec{v}_i - \frac{1+\mu}{2} [(\vec{v}_i - \vec{v}_j) \cdot \hat{e}_{ij}] \hat{e}_{ij}, \\ \vec{v}'_j &= \vec{v}_j + \frac{1+\mu}{2} [(\vec{v}_i - \vec{v}_j) \cdot \hat{e}_{ij}] \hat{e}_{ij},\end{aligned}\tag{7.1}$$

where primed quantities stand for post-collisional velocities, and $\hat{e}_{ij} \equiv (\vec{r}_i - \vec{r}_j) / |\vec{r}_i - \vec{r}_j|$ is unitary vector oriented along the direction connecting their centers¹. The circular boundary supply continuously energy to the system as if were driven by a vibrating wall. If the frequency of the oscillating wall is large enough, the energy supply may be modelled by a heated wall. The thermal wall implementation [51] is simple: whenever a particle touches the

¹Notice that Eq. (7.1) is equivalent to Eq. (6.12), but expressed in a more detailed way.

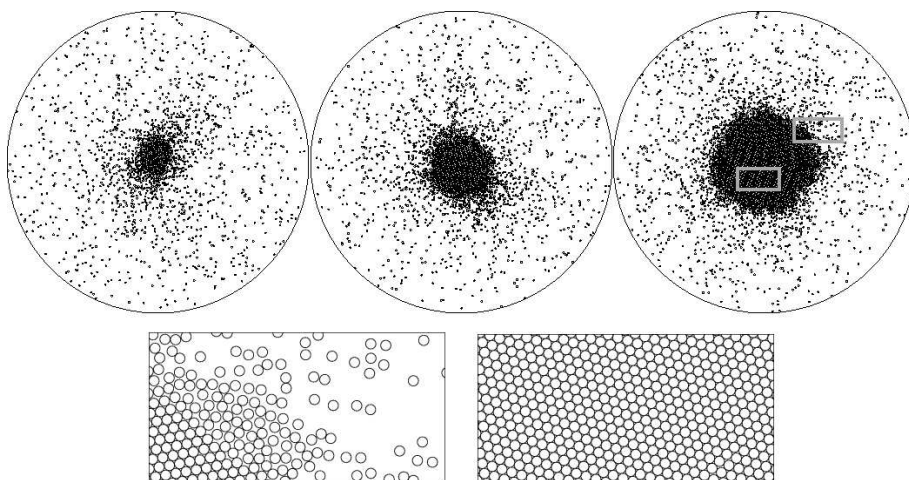


Figure 7.1: Snapshots of the system (top, from left to right) for $N = 1716$, 2761 and $N = 5055$. Also shown are magnifications (bottom) of the indicated areas in the rightmost snapshot. Notice the coexistence of the different kinds of packings.

wall its velocity is chosen from a Maxwell distribution according to T_0 (which is measure in units of energy), that we set to unity. We put $m = 1$ and fixed $R/d = 100$ and $\mu = 0.888$, while the total number of particles N served as the control parameter in the simulations. So the scaled time unit is $d(m/T_0)^{1/2} = 1$.

We were mostly interested in a hydrodynamic (low Knudsen number) regime, when the mean free path is small compared to the system size and the mean free time is small compared with any hydrodynamic time scale. This requires $N \gg R/d = 100$. For N in the range of a few hundred, we observed a dilute granular gas with an increased density in the center of the box (although not observable to naked eye). The clustering in the center becomes more pronounced as N grows. The clustering can be easily explained in the hydrodynamics language: because of the inelastic collisions the granular temperature goes down as one moves away from the wall toward the center of the box. This, combined with the constancy of the pressure throughout the system, causes an increased particle density at the center. As N increases further, the particle density in the center approaches the hexagonal close packing value $n_c = 2/(\sqrt{3}d^2)$. Figure 7.1 shows snapshots of the system for three different, but sufficiently large, values of N . A perfect hexagonal packing is apparent nearby the center. Movies of these simulations show that the macro-particle (close-packed cluster) position fluctuates around the center of the box, while the cluster shape fluctuates around a circular shape. Notice that both kind of fluctuations, in particular the off-center location if the cluster, can not be explained hydrodynamically.

Our diagnostics was focused on two radial distributions: the number density of the particles $n(r)$ and the PDF of a radial position of the center of mass

of the system $P(\mathbf{r}_m)$, defined below. To measure $n(\mathbf{r})$ (likewise in Chapter 6), we recorded all particle coordinates in intervals of 100,000 particle collisions. For each snapshot we introduced bins in the form of concentric circular rings of width 0.5, centered in the center of mass of the system. For each particle we determined the fraction of its area falling in each of the rings, summed the contributions of all particles to each bin, and divided the result by the bin area. The resulting radial profile was averaged over many snapshots (typically 1000). Similar method is employed to measure $P(\mathbf{r}_m)$. As we are interested in steady-state distributions, we disregarded initial transients. This was monitored by the time-dependence of the average kinetic energy of the particles (the first decayed and then approached an almost constant value) and the time-dependence of the center of mass itself.

7.3 Hydrostatic theory

As the fluctuations are relatively weak, it is natural to start with a purely hydrodynamic description. For a zero mean flow this is a *hydrostatic* theory, as it operates only with (time-independent) granular density $n(\mathbf{r})$, temperature $T(\mathbf{r})$ and pressure $p(\mathbf{r})$. The energy input at the thermal wall is balanced by dissipation due to inter-particle collisions, and one can employ the momentum and energy balance equations:

$$\begin{aligned} p &= \text{const}, \\ \nabla \cdot (\kappa \nabla T) &= I. \end{aligned} \tag{7.2}$$

Here κ is the thermal conductivity and I is the rate of energy loss by collisions. Note that the heat flux, entering the thermal balance in Eq. (7.2), does not include an inelastic term, proportional to the *density* gradient [140, 141, 142]. In the nearly elastic limit $1 - \mu \ll 1$, that we are interested in, this term can be neglected. The boundary condition at the thermal wall is $T(r = R, \theta) = T_0$, where r and θ are polar coordinates with the origin at the center of the box.

To proceed from here and compute numerical factors, we need constitutive relations: an equation of state $p = p(n, T)$ and relations for κ and I in terms of n and T . As we attempt to describe close-packed clusters, the first-principle standard techniques, based on the Boltzmann or Enskog equations, are inapplicable. Grossman *et al.* [154] suggested a set of semi-empiric relations in two dimensions, that are valid for all densities, all the way to hexagonal close packing. Their approach ignores possible coexistence beyond the disorder-order transition and assumes that the whole system is on the thermodynamic branch extending to the hexagonal close packing. The delicate issue of phase coexistence (liquid-like phase, close-packed phase with multiple domains) occur here is close analogy to the system of *elastic* hard spheres [122, 144, 164]. Grossman *et al.* employed free volume arguments in the vicinity of the close packing, and suggested an interpolation between the hexagonal-packing limit and the well-known low-density relations. The resulting *global* equation of state and

constitutive relations [154] read

$$\begin{aligned} p &= n T \frac{n_c + n}{n_c - n}, \\ \kappa &= \frac{\sigma n (\alpha l + d)^2 T^{1/2}}{l}, \\ I &= (\sigma/\gamma l) (1 - \mu^2) n T^{3/2}. \end{aligned} \quad (7.3)$$

Here l is the mean free path, which is given by an interpolation formula [154]

$$l = \frac{1}{\sqrt{8}nd} \frac{n_c - n}{n_c - \alpha n}, \quad (7.4)$$

and $\alpha = 1 - (3/8)^{1/2}$. These relations include three dimensionless numerical factors of order unity: α , γ and σ , where the latter drops out from the steady-state problem. They can be calculated exactly from the velocity distribution function. However, this distribution is poorly understood [124]. Grossman *et al.* determined the optimum values $\alpha = 1.15$ and $\gamma = 2.26$, verified by a detailed comparison with molecular dynamics simulations of a system of inelastic hard disks in a rectangular box without gravity, driven by a thermal wall, and numerical solutions of the hydrostatic equations (7.2) in rectangular geometry. We adopted the same values of α^2 and γ in our calculations for the circular geometry.

Most interesting state among the one-dimensional states is the azimuthally symmetric state (θ -independent), which is indeed one of the possible solutions of Eq. (7.2). In this case, assuming azimuthal symmetry, we rewrite Eq. (7.2) as

$$\begin{aligned} p(n, T) &= \text{const}, \\ \frac{1}{r} \frac{d}{dr} \left[r \kappa(n, T) \frac{dT}{dr} \right] &= I(n, T). \end{aligned} \quad (7.5)$$

Equations (7.5) can be reduced to a single equation for the scaled inverse density $z(r) \equiv n_c/n(r)$. In the rescaled coordinate, $r/R \rightarrow r$, the circle radius becomes 1, and Eqs. (7.5) reduces to

$$\frac{1}{r} \frac{d}{dr} \left[r \mathcal{F}(z) \frac{dz}{dr} \right] = \Lambda \mathcal{Q}(z), \quad (7.6)$$

where

$$\begin{aligned} \mathcal{F}(z) &= \frac{(z^2 + 2z - 1) \left[\alpha z(z - 1) + \sqrt{32/3}(z - \alpha) \right]^2}{(z - \alpha)(z - 1)^{1/2} z^{3/2} (z + 1)^{5/2}}, \\ \mathcal{Q}(z) &= \frac{(z - \alpha)(z - 1)^{1/2}}{(z + 1)^{3/2} z^{1/2}}, \end{aligned} \quad (7.7)$$

²The value of α differs in systems with gravity ($\alpha \approx 0.6$) [130].

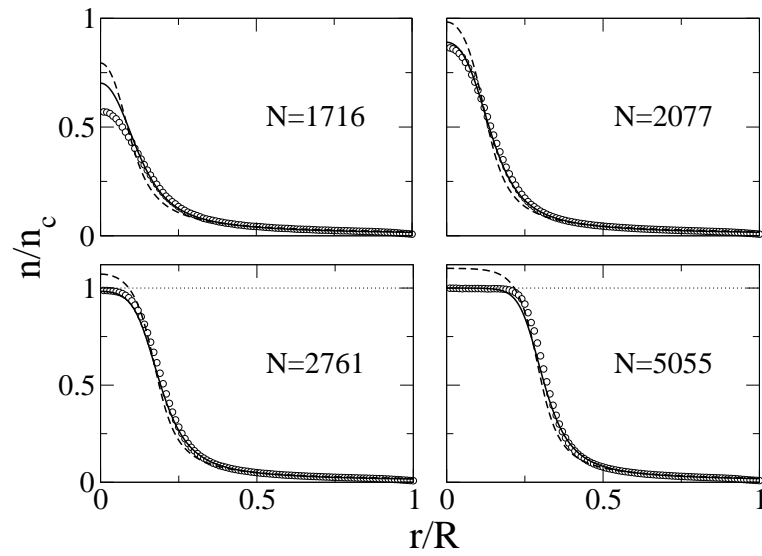


Figure 7.2: Scaled density n/n_c versus scaled radius r/R as observed in simulations (circles) and predicted by the hydrostatic theory with the constitutive relations by Grossman *et al.* [154] (solid lines) and with the Enskog-type relations [135] (dashed lines) for four different values of the total number of particles N . For the rest of parameters please see the text. The dotted lines indicate $n/n_c = 1$.

and $\Lambda = (32/3\gamma)(R/d)^2(1 - \mu^2)$ is the hydrodynamic inelasticity parameter, first introduced in Ref. [159] in the context of rectangular geometry³. The fixed total number of particles yields a normalization condition, which read

$$\int_0^1 z^{-1}(r) r dr = f/2, \quad (7.8)$$

where $f = (\sqrt{3}/2\pi)N(d/R)^2$ is the average grain area fraction. Equations (7.6) and (7.8), together with the obvious boundary condition $dz/dr|_{r=0} = 0$ (this is a consequence of the fact that the temperature gradient vanish at the center of the system), form a complete set. The hydrostatic problem is completely determined by two scaled parameters Λ and f . This can be solved numerically as explained in Chapter 6 for the annular geometry. That is, in order to solve Eq. (7.6), instead of consider the area fraction f one can prescribe the inverse density at the center of the system z_0 . This condition, combined with the no-flux condition at $r = 0$ define a Cauchy problem for $z^{-1}(r)$ [128]. Solving the Cauchy problem one can compute the respective value for f from Eq. (7.8). At fixed Λ , z_0 is a strictly monotonically decreasing function of f . Therefore, an alternative parameterization of the azimuthally symmetric state is given by the scaled numbers Λ and z_0 . The same considerations keep for the marginal stability analysis (see below).

In our event-driven simulations we varied the number of particles N . Accordingly, the scaled parameter f is varied, while $\Lambda = 9980$ was constant. Figure 7.2 shows a comparison of the hydrostatic radial density profiles with the radial density profiles obtained in simulations, for four different values of N . The simulations profiles were averaged over 1000 uncorrelated configurations. It can be seen from Fig. 7.2 that for $N = 1716$ the theory overestimates the density in the center of the box. This is expected as, for relatively small N , the maximum density is considerably less than the close-packing density, and the accuracy of the constitutive relations by Grossman *et al.* is not as good. For larger N the agreement rapidly improves. As Fig. 7.3 shows, the agreement between the hydrostatic theory and the simulations persists for the *maximum* radial densities at different number of particles N . The agreement is excellent for the densities approaching the close packing density, whereas for small N , there is small deviations. In absolute scale, however, the agreement is very good. We also computed the density profiles using another set of semi-empiric constitutive relations⁴, those obtained in the spirit of Enskog theory [135]. These read,

$$\begin{aligned} \kappa &= \frac{2dn\Gamma^{1/2}G}{\pi^{1/2}} \left[1 + \frac{9\pi}{16} \left(1 + \frac{2}{3G} \right)^2 \right], \\ I &= \frac{8(1 - \mu)n\Gamma^{3/2}G}{d\sqrt{\pi}}, \end{aligned} \quad (7.9)$$

³Notice that, no matter how small (but finite) the inelasticity is, the parameter Λ goes to infinity in the thermodynamic limit $R \rightarrow \infty$.

⁴These were already employed in Chapter 6.

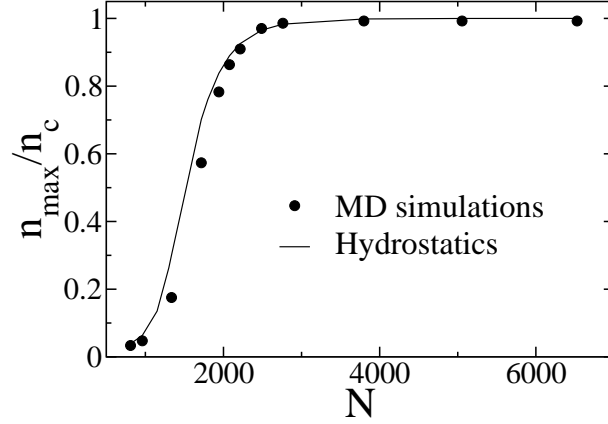


Figure 7.3: Maximum scaled density n_{\max}/n_c as a function of N as predicted by the hydrostatic theory and observed in simulations.

and the equation of state first proposed by Carnahan and Starling [162]

$$P = nT(1 + 2G), \quad (7.10)$$

where $G = \nu(1 - \frac{7\nu}{16})/(1 - \nu)^2$ and $\nu = n(\pi d^2/4)$ is the solid fraction. One can clearly see from Fig. 7.2 that the Enskog-type constitutive relations predict unphysically high densities in the cluster.

We employ the same hydrostatic formulation to perform a systematic *linear stability analysis* of the reference state (azimuthally symmetric solution). In the framework of time-dependent hydrodynamics, this corresponds to marginal stability analysis of the azimuthally symmetric solution with respect to small perturbations along the azimuthal coordinate θ . Substituting

$$\hat{z}(\mathbf{r}, \theta) = z(\mathbf{r}) + \varepsilon \phi_k(\mathbf{r}) \sin(k\theta), \quad (7.11)$$

where $k \geq 1$ is an integer, into Eq. (7.2) and linearizing around the azimuthally symmetric state $z(\mathbf{r})$ with respect to the small correction $\varepsilon \ll 1$, we arrive to a linear eigenvalue problem for $k = k(f)$ which read

$$\zeta_k'' + \frac{1}{r} \zeta_k' - \left[\frac{k^2}{r^2} + \frac{\Lambda Q'(z)}{\mathcal{F}(z)} \right] \zeta_k = 0, \quad (7.12)$$

where $\zeta_k(\mathbf{r}) = \phi_k(\mathbf{r}) \mathcal{F}(z)$. This equation is complemented by the boundary conditions

$$\zeta_k(0) = 0 \quad \zeta_k(1) = 0. \quad (7.13)$$

For a fixed value of Λ , we obtain numerically the marginal stability curve $k = k(f)$ and the corresponding eigenfunctions ζ_k by analyzing (as explained in

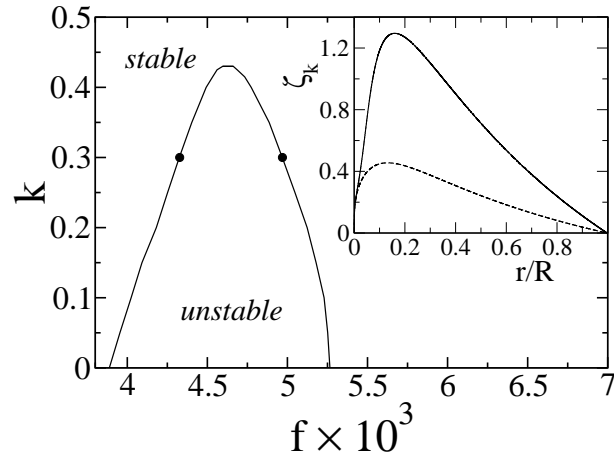


Figure 7.4: Main graph: The marginal stability curve for a fixed $\Lambda = 10^4$. In order to observe the symmetry breaking instability k must be integer. However, for our system all the solutions lay below $k < 1$. Therefore the azimuthally symmetric state is stable. The black dots correspond to the eigenfunctions shown in the inset. Inset: Eigenfunctions ζ_k associated with the eigenvalue $k = 0.3$. The dashed (solid) line corresponds to the low-density (high-density) branch of the marginal stability curve for $f = 4.316 \times 10^{-3}$ ($f = 4.96 \times 10^{-3}$).

Chapter 6) the resulting eigenvalue problem Eqs. 7.12 and 7.13. Our numerical results imply that Eq. 7.12 has only two possible solutions which correspond to the low- and high-density “instability” borders. They are shown in Figure 7.4 for $\Lambda = 10^4$. The low- f and high- f values eventually collapse at a maximum k_{\max} , which means that a density modulation with a short enough azimuthal wavelength (high enough modes) should be stable, for all f . For the $\Lambda = 10^4$ case, the marginal stability curve has its maximum at $k \approx 0.43 < 1$ which is less than unity. This means that, because of the periodicity of the perturbation, all the values for k obtained from the eigenvalue problem are unphysical. Because of the periodicity of the perturbation, k must be integer, thus all the physical values ($k = 1, 2, 3 \dots$) lay well above the marginal stability curve (see Fig. 7.4), i.e. there are not integer solutions. Similar curves (all of them below $k = 1$) can be obtained from $\Lambda = 10^2$ to $\Lambda = 10^6$ (not shown in Fig. 7.4). Therefore, there are no steady-state solutions with broken azimuthal symmetry which would bifurcate from the azimuthally symmetric solution. This is in stark contrast with the presence of bifurcating states with broken azimuthal symmetry in the model system (a driven granular gas in annular geometry) studied in Chapter 6. Symmetry-breaking instabilities are also observed in rectangular geometry [157, 159, 160]. As we discussed in the previous chapter, the driving force of the instability is the negative effective azimuthal compressibility of the granulate, which is caused by the destabilizing role of collisional losses [43, 128]. However, this is necessary but not sufficient for instability. In fact, the stabilizing role is

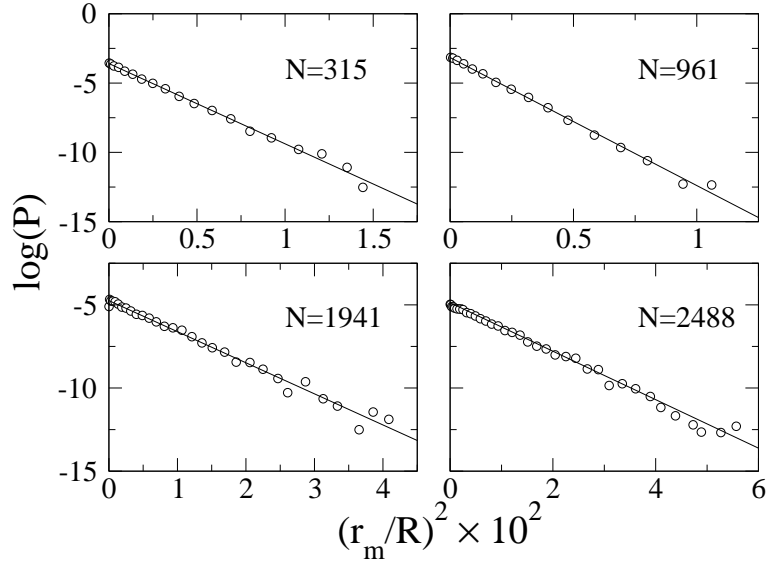


Figure 7.5: The logarithm of the radial probability distribution function $P(r_m)$ of the center of mass position versus $(r_m/R)^2$, for four values of N .

played here by the heat conduction in the azimuthal direction, which outweighs the collisional losses, and thus suppress the instability at any f and any Λ .

This result, the absence of solutions with broken symmetry in the radial geometry, agrees with the persistence of circular macro-particle shapes as observed in our simulations: no other shapes but circular has been observed. This prediction is very robust, as it is independent of the values α and γ , and even of the constitutive relations employed. For instance, the same result is found by employing Enskog-type relations [135] (see Eq. (7.9)).

7.4 Macro-particle fluctuations

Now we turn to stationary fluctuations, that is, after transients die out. To better characterize the fluctuation-dominated behavior of this system, we compute the radial coordinate $r_m(t)$ of the center of mass of the system. The radial probability distribution function $P(r_m, t)$ is normalized by the condition $2\pi \int_0^R P(r_m, t) r_m dr_m = 1$, where we have returned to the dimensional coordinate. Typical molecular dynamics results are presented in Fig. 7.5, which shows $\log P(r_m)$ versus $(r_m/R)^2$, for four different values of N . The observed straight lines clearly indicate a Gaussian distribution, both for small and large N values.

This finding strongly suggests a Langevin description of the macro-particle. One can consider the macro-particle performing an over-damped motion in a

(central-symmetric) confining harmonic potential⁵ $U(\mathbf{r}_m) = k\mathbf{r}_m^2/2$ and driven by a (delta-correlated) discrete-particle noise $\eta(t)$. The Langevin equation for this problem reads

$$h\dot{\mathbf{r}}_m + k\mathbf{r}_m = \eta(t), \quad (7.14)$$

where h is the damping rate, $\langle \eta(t)\eta(t') \rangle = 2h\Gamma \delta(t-t')$, and Γ is an effective magnitude of the discrete-particle noise. In the simplest approach the close-packed cluster and the discrete-particle noise can be characterized, for each N , respectively, by a point-like mass M and mobility χ , and by T_0 , the temperature of the circular wall. A stochastic equivalent description is provided in terms of the Fokker-Planck equation for $P(\mathbf{r}_m, t)$ [1, 2]. In the limit $\Gamma \rightarrow 0$, the (deterministic) steady-state solution of Eq. (7.14) is $\mathbf{r}_m = \dot{\mathbf{r}}_m = 0$: the macro-particle at rest, located at the center of the box. At $\Gamma > 0$, the steady state distribution function is given by the steady state solution of the Fokker-Planck equation [1, 2] which is $P(\mathbf{r}_m) = (\pi\sigma^2)^{-1} \exp(-\mathbf{r}_m^2/\sigma^2)$, where $\sigma^2 = \Gamma/k$, and the normalization constant is computed for $\sigma \ll R$. The variance σ^2 is the ratio of Γ (a characteristic of the discrete noise) and k (a macroscopic quantity). An important insight can be achieved from the N -dependence of σ , obtained by molecular dynamics (see Section 7.2). In analogy with equilibrium systems, one might expect the relative magnitude of fluctuations to decrease with increasing N . Surprisingly, this is not what we observed, see Fig. 7.6. One can see that $\sigma(N)$ approaches a plateau, that is fluctuations persist at large N . The small- N behavior (the first three data points: $N = 150, 315$ and 480) in Fig. 7.6 agrees with the dependence $\sigma/R = \mathcal{O}(N^{-1/2})$, expected for an ideal gas in equilibrium. Not surprisingly, for these relatively small N the clustering effect is small. On the other hand, at very large N , when the whole system approaches close packing (in our event-driven simulations, this corresponds to $N = 36275$), σ/R must go to zero. We could not probe this regime, however, as simulations became prohibitively long already at $N \sim 15000$. An apparently related phenomenon has been recently reported for rectangular geometry, in the context of a van der Waals-like phase separation in a granular gas driven by a thermal wall [148].

7.5 Conclusions

We employed a simple model system [153] to investigate the structure and fluctuations of dense clusters emerging in granular gases. The density profiles, obtained in event-driven molecular dynamics simulations, are well described by hydrostatic equations which employ the constitutive relations suggested by Grossman et al. [154]. This agrees with similar results in rectangular geometry, with and without gravity [130, 154, 159]. We also extended their validity for lower restitution coefficient, and for the circular geometry. The agreement is particularly good for the large density region (close packing). The azimuthally symmetric state is predicted to be stable, fact which is apparent with our simulations. The observed Gaussian fluctuations of the center of mass, which are

⁵The systematic restoring force which confines the macro-particle has a potential $U(\mathbf{r}_m)$. Not far from the center, $U(\mathbf{r}_m)$ can be approximated by a harmonic potential.

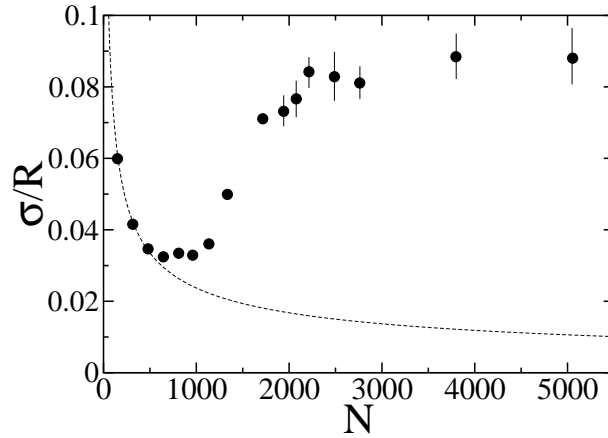


Figure 7.6: Scaled standard deviation of the center of mass position as a function of N , obtained in molecular dynamics simulations (dots). The dashed line shows is for $\sigma/R = 0.75 N^{-1/2}$. This power law characterizes the fluctuations of an ideal (elastic) gas in equilibrium.

too large to be explained by diffusion, suggest an effective Langevin description in terms of a macro-particle in a confining potential of hydrodynamic nature, driven by discrete particle noise. Surprisingly, the fluctuations persist as the number of particles in the system is increased. This unexpected behavior is stark contrast with the shown by elastic gases in thermal equilibrium.

Other important point is the transition from a "smooth state" (with enhanced density in the middle) to a "cluster state" with a pronounced and sharp-edged cluster in the center, as a function of particle number density. It has not been stated before, that the process of cluster formation requires a certain particle number and the transition between a homogeneous (or irregular) state to a regularly clustered state (with a persisting cluster in the middle) is rather sharp. In our case it is at $N = 1700 \pm 300$.

It is worth mention that the global constitutive relations of Grossman *et al.* [154] completely ignore the issue of coexistence of different phases of the granulate: the liquid-like phase, the random close-packed phase, etc. However, the vibrofluidized steady state, considered in this chapter, has a zero mean flow. Therefore the viscosity terms in the hydrodynamic equations vanish. This fact is not merely a technical simplification. The shear viscosity of granular flow is finite in the liquid-like phase, and infinite in the (multiple) domains of the random close-packed phase. The effective total viscosity of the system is expected to diverge when the coarse-grained density slightly exceeds the freezing density [145, 146]. This invalidates any hydrodynamic description for sufficiently dense flows, and requires the introduction of an order parameter and a different

type of the stress–strain relation into the theory (cf. Ref. [153]). Luckily, these complications do not appear for a zero–mean–flow state. Indeed, the equation of state, heat conductivity, and the inelastic heat loss rate do not exhibit any singularity around the freezing point, and all the way to the hexagonal close packing. Therefore, the hydrostatic description remains reasonably accurate far beyond the freezing point.

Future work should focus on dense clusters (more precisely, on their “core” regions) and characterize the positional and orientational ordering at different N . This can be achieved by measuring two correlation functions: the positional correlation function and the orientational correlation function. The motivation is the following. There are classical papers of Kosterlitz and Thouless, Young and Nelson, and Halperin, from the 70-ies —these yielded the KTHNY theory of melting, reviewed by Strandburg in Ref. [119]—, which suggested that melting in assemblies of *elastic* hard disks occurs (as the density decreases) via two continuous phase transitions: the first one from the perfect hexagonally packed phase to the so called *hexatic*⁶ phase, and the second one from the hexatic phase to a liquid–like phase. A main question about our inelastic system which remains to be answered is, as the density in the central region increases, whether there is any signature of additional instabilities.

⁶This phase can exist between solid and liquid phases. The system in the hexatic phase has no long-range translational order but has quasi-long-range orientational order.

Part III

Appendices

Appendix A

Equilibrium properties of the Lattice Gas

The *driven lattice gas* studied in Chapter 3 reduces to the (equilibrium) *lattice gas* [165] for zero field. This is a model for density fluctuations and liquid-gas phase transformations. As its nonequilibrium counterpart, this is defined in a square lattice with $N = L_{\parallel}L_{\perp}$ sites¹. Thus, each lattice site i can exist in two states, occupied by a particle or empty, labelled by an occupation variable $n_i = 1$ or $n_i = 0$, respectively. The *lattice gas* can be mapped to the *Ising* model with *ferromagnetic* couplings². The Ising model is perhaps the simplest system that undergoes a nontrivial phase transition in two or more dimensions. The model was initially proposed to describe ferromagnetism —the presence of spontaneous magnetization in metals such as Fe and Ni below a critical temperature T_c —. The relation between the lattice gas and the Ising model is set by simple change of variables, namely, $s_i = (2n_i - 1)/2$, where s_i are spin variables capable of two orientations, “up” and “down”. The spin up $s_i = 1/2$ and the spin down $s_i = -1/2$ states correspond to occupied ($n_i = 1$) and unoccupied ($n_i = 0$) cells, respectively. Each spin i interacts with one another via an exchange interaction $J_{ij} > 0$. Assuming ferromagnetic coupling and isotropic interactions ($J_{ij} \equiv J > 0$), the Ising Hamiltonian is

$$H = -J \sum_{\langle ij \rangle} s_i s_j - B \sum_{i=0}^N s_i , \quad (\text{A.1})$$

where $\langle ij \rangle$ denotes neighbor interactions and B is the external magnetic field, which plays the role of the chemical potential of the lattice gas. In fact, the *canonical* partition function for the ferromagnetic model is the *grandcanonical* partition function [3] for the lattice gas model. Therefore the lattice model is

¹We consider here only two-dimensional lattices.

²Historically, the Ising model [52] was introduced before the lattice model [165]. Likewise, the lattice gas as and the *binary alloy* model [32] are equivalent.

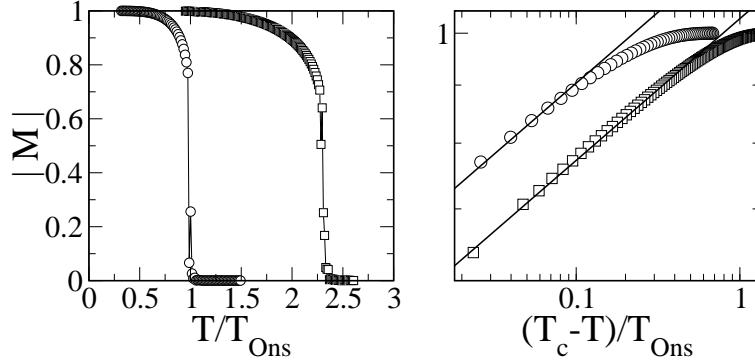


Figure A.1: Phase transition in the Ising model with NN (circles) and NNN couplings (squares). Left panel: Spontaneous magnetization M as a function of the temperature. The magnetization vanishes abruptly at $T_c/T_{\text{Ons}} = 1$ for NN couplings, and at $T_c/T_{\text{Ons}} = 2.32$ for the NNN case. Otherwise is zero for $T > T_c$ in both cases. Right panel: As expected in equilibrium systems [34] the order parameter critical exponent do not depend on the dynamics details. The solid lines represent slopes of $\beta_{\text{Ising}} = 1/8$.

isomorphic with the Ising model. Thermodynamically the descriptions of the ising model and the lattice gas are equivalent, but there are simplifying features for the Ising magnet. Henceforth we shall refer to them without distinction.

Lars Onsager [31, 32] gave in 1944 the (exact) partition function for the two-dimensional model, in the absence of external magnetic field. The Onsager solution showed the existence of a second order phase transition at $T_c = 2/\ln(1 + \sqrt{2}) Jk_B^{-1}$, referred to as the Onsager temperature T_{Ons} . The spontaneous magnetization

$$|M| = \left| \frac{1}{N} \sum_{i=1}^N s_i \right| \quad (\text{A.2})$$

is the order parameter for this transition. Above the critical temperature the (average) spontaneous magnetization is zero, whereas below criticality M is non-zero, thus one finds the system in a ferromagnetic state. Due to the up-down symmetry of the Ising system, the spontaneous magnetization is doubly degenerate, with an “up” phase and a “down” phase. In the terminology of the lattice gas, there should be a dense (liquid) phase coexisting with a dilute (gas) phase below the critical temperature. Otherwise, typical configurations are disordered. The left panel in Fig. A.1 shows the second order phase transition for nearest-neighbor (NN) couplings and next-nearest-neighbor (NNN) couplings, as schematized in Fig. 3.4 in Chapter 3. For NN couplings, the first sum in Eq. (A.1) runs over the four NN sites, and for the NNN case it runs over the eight NNN sites. As is shown in Fig. A.1, the phase transition occurs exactly at T_{Ons} for NN couplings. The immediate effect of considering additional neigh-

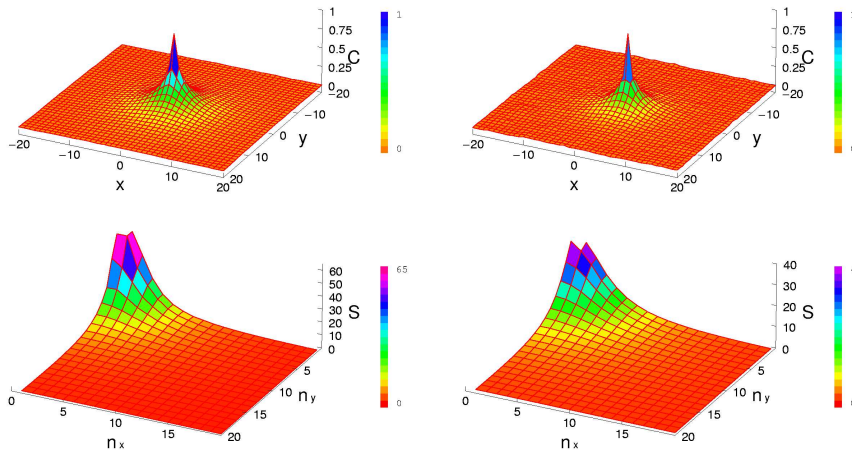


Figure A.2: Surface plots of the two-point correlation (upper row) and the structure factor (lower row). These are for the Ising magnet, or equivalently the lattice gas, on a $L_{\parallel} \times L_{\perp} = 128 \times 128$ lattice with NN (left column) and NNN interactions (right column). To avoid complications due to inhomogeneous ordered phases, we choose temperatures above criticality. Temperatures are $T/T_{\text{Ons}} = 1.09$ for the NN and $T/T_{\text{Ons}} = 2.61$ for the NNN case. Notice the change of color code with each plot.

bors, as in the NNN case, is the rising of the critical temperature. For NNN couplings, the critical temperature raises to $T_c = 2.32 T_{\text{Ons}}$ [94]. In the neighborhood of the critical temperature the spontaneous magnetization behaves like $M \approx (1 - T/T_c)^{\beta_{\text{Ising}}}$ as $T \rightarrow T_c -$. Here, β_{Ising} is the order parameter critical exponent. The right panel of Fig. A.1 shows the behavior of M near T_c for NN and NNN couplings. In both cases, $\beta_{\text{Ising}} = 1/8$. This result is consistent with (equilibrium) renormalization group ideas [34], which set up that the critical exponents are universal. It means that there are only a few parameters, such as dimensionality and underlying symmetries which are relevant near the critical point, therefore critical exponents do not depend on the particular system, either magnetic or fluid.

In zero magnetic field the pair-correlation function is of particular interest since it in a sense measures the “degree of order” of the lattice. It is defined in general from the partition function as $C = \langle s_i s_j \rangle$, where $\langle \dots \rangle$ (see also Eq. (3.6) in Chapter 3) denotes the proper ensemble average. Two-point correlations are shown in Fig. A.2. Correlations in the equilibrium Ising model are short ranged, except at the critical point where the free energy shows a nonanalytic point, controlled by a correlation length ξ . Specifically, they decay exponentially (in Fig. A.2 or more clearly in Fig. A.3) when r , a typical inter-particle separation, becomes large compared to ξ . Translated into the momentum space,

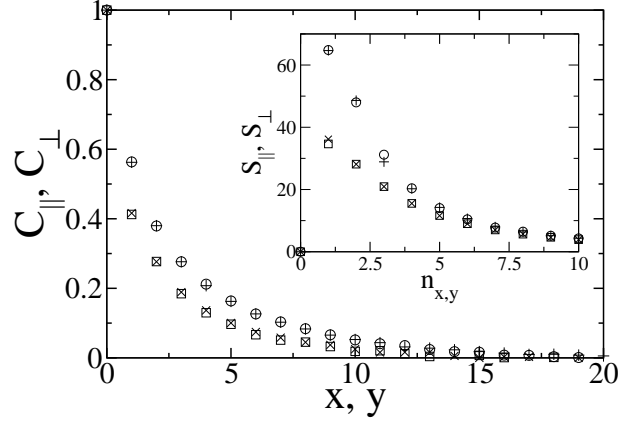


Figure A.3: Main graph: Parallel C_{\parallel} and transverse C_{\perp} projections of the two-point correlation function. Symbols \circ (parallel) and $+$ (transverse) are for NN interactions, whereas \square (parallel) and \times (transverse) correspond to the NNN case. Inset: Parallel S_{\parallel} and transverse S_{\perp} projections of the structure factor. Here, $n_{x,y} = 128 \kappa_{x,y} / 2\pi$ are integers. Symbols are as in the main graph. System size and temperatures are as in Fig. A.2.

the pair correlation function lead to the structure factor $S(\kappa_x, \kappa_y)$ (see Eq. (3.7) in Chapter 3), i.e., structure factor is the Fourier transform of the two-point correlation function. Structure factors are shown in Figs. A.2 and A.3. Exponential decay in correlations, takes the form of “analyticity at the origin” in the momentum space. Notice also that this analyticity in the origin do not depend on whether one takes isotropic or anisotropic couplings. As indicated above, we have assumed isotropic couplings between spins, and therefore both C and S are isotropic (more clearly in Fig. A.3). In Chapter 3 we show that the *driven lattice gas* behaves quite differently, displaying generic power law decay in two-point correlations, not only at the critical point, and discontinuity singularity at the origin in the structure factor.

Appendix B

Interfacial stability of Driven Lattice Gases under saturating field

In Chapter 3 we pointed out one of the most striking, even counterintuitive, features of the *Driven Lattice Gas* (DLG) with nearest-neighbor (NN) interactions: Monte Carlo (MC) simulations with Metropolis rates show that the critical temperature T_E monotonically increases with the external driving field from the Onsager value $T_0 = T_{\text{Ons}} = 2.269 \text{ Jk}_B^{-1}$ to $T_\infty \simeq 1.4 T_{\text{Ons}}$. As we concluded, this is associated with the fact that a driven particle is geometrically restrained in the DLG. In fact, allowing hops and interactions to the next-nearest-neighbors (NNN) one observes just the opposite behavior: the critical temperature decreases as the field increases. Moreover, there is no phase transition for a large enough field, i.e., $T_E \rightarrow 0$ as $E \rightarrow \infty$. Or in other words, in the DLG with NNN interactions a strong field prevents transition to an ordered low-temperature phase. This is better illustrated in Fig. 3.2 in Chapter 3. Qualitatively, this difference of behavior in the infinite field limit between the two models may be understood in terms of stability of the liquid-gas interface. That is, in contrast with the NN case, a (well-ordered) interface cannot be stable under a strong field in the NNN case. This suggests a balance between thermal effects, which favor the stability (the order) of the interface [101], and driving effects, which would drive particles out of the interface favoring disorder.

In order to study this balance, the disparate behavior between both dynamics, and characterize the two competing tendencies —i.e, the field vs. temperature balance— we propose a generalized driven lattice gas model. This is an intermediate model between the two cases above mentioned (the NN and the NNN case) which captures the behavior in the large field limit observed in each system. It is defined on a two-dimensional lattice $L_{\parallel} \times L_{\perp}$ with periodic

boundary conditions in which particles interact via the usual Ising Hamiltonian,

$$H = -4 \sum_{\langle j,k \rangle} \sigma_j \sigma_k . \quad (\text{B.1})$$

Each site $i \in \mathbb{Z}^2$ is either occupied by a particle or empty, which we denote by a lattice occupation number σ_i taking two values: $\sigma_i = 1$ (occupied) or $\sigma_i = 0$ (empty). The sum in the Hamiltonian runs over all the NNN sites. As in the standard DLG, dynamics is induced by the competition between a heat bath at temperature T and an external driving field E , which break the *detailed balance* condition. The field is assumed pointing along one of the principal lattice directions, say horizontal. Time evolution is then by microscopic dynamics according to the *Metropolis* transition probability per unit time w (this was previously defined in Eq. (3.2) in Chapter 3):

$$w(\sigma \rightarrow \sigma') = \min \left\{ 1, e^{(\Delta H + \vec{E} \cdot \vec{x}) / k_B T} \right\} . \quad (\text{B.2})$$

Here ΔH is the energy difference of a particle-hole exchange and $\vec{E} \cdot \vec{x}$ denotes the dot product between the field and the displacement of the exchange. $\sigma \equiv \{\sigma_i; i \in \text{two-dimensional lattice}\}$ stands for a configuration.

Given a particle, its neighboring sites along the principal lattice directions has different probability to be reached than the sites along the diagonals (see Fig. B.1). The former are always accessible (probability 1), whereas the latter have probability $0 \leq \alpha \leq 1$, parameter which is set at the beginning of the simulation (as well as T and E). The algorithm proceed as follows¹:

1. We randomly select a NNN pair i, j of sites with different occupancies, $\sigma_i \neq \sigma_j$.
2. As Fig. B.1 illustrates, if the selected pair is along one of the principal lattice directions the exchange attempt is allowed (Go to next item). In other case, draw a random number r_1 , and if $r_1 \leq \alpha$ then the attempt is allowed (Go to next item), otherwise rejected (Go to item 1).
3. Perform a standard MC trial move controlled by the Metropolis *rate* function $w(z) = \min\{1, e^{-z}\}$, i.e., controlled by the standard biased rate Eq. (B.2). To be specific, first compute z ; if $z \leq 0$ the attempt (particle-hole exchange) is finally accepted; if, however, $x > 0$, we draw a random number r_2 and perform the exchange only if $r_2 \leq e^{-x}$.
4. Go to item 1.

Notice that when $\alpha \rightarrow 0$ only NN particle-hole exchanges are allowed, otherwise there is a non-zero probability for diagonal hops. The limit case of $\alpha = 1$ corresponds with the NNN dynamics, i.e., with the NDLG model already introduced

¹The algorithm as we use it is more complicated to obtain better (and faster) results. We do not present this algorithm due to its complexity. Instead, we show a simpler algorithm which would work like this.

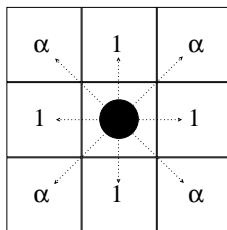


Figure B.1: Schematic diagram of the accessible sites a particle (at the center, marked with a dot) has for the α DLG. Attempts (particle-hole exchanges) along the principal lattice directions are always allowed (marked with probability 1). Diagonal attempts are allowed with probability α . The limit of $\alpha \rightarrow 0(1)$ corresponds with NN (NNN) couplings. Once α is set at the beginning, the allowed exchanges are controlled by the Metropolis rate function Eq. (B.2).

in Chapter 3. Therefore, this model (henceforth referred to as the α DLG) can capture both the DLG and NDLG phenomenology by varying the parameter α (the *effective connectivity*). One may also think on α as a *temperature* which controls the diagonal degrees of freedom. For $E = 0$ this model reduces to the equilibrium lattice gas² (see Appendix A).

We carried out extensive MC simulations on the α DLG by assuming half-filled lattices and periodic boundary conditions (toroidal conditions). Hence, nontrivial nonequilibrium steady state is set in asymptotically. As in the standard DLG, MC simulations reveal that this model undergoes a *temperature-induced* second-order phase transition. This transition is analogous to the studied in Chapters 3 and 4. However, in this appendix we are rather interested in the stability of the interface under saturating fields. Specifically, we study the mechanisms which lead to an ordered or disordered low-temperature states in the large field limit, i.e., to a stable or unstable interface. To this end, we restrict ourselves to the $E \rightarrow \infty$ limit and to $T \rightarrow 0$. The latter limit is the most favorable case for ordering, which will enable us to identify the point in where the field effects outweigh the thermal effects. In addition, this limit is convenient for theoretical and computational purposes since T is no longer a parameter.

For $\alpha = 0$, we observe fully frozen striped configurations, which extends along the field direction. Here, a one-strip liquid-like (rich-particle) phase percolates along the field direction (the density of the vapor phase is zero). When increasing α , i.e. increasing the weight of the diagonal dynamics, some particles are driven out the interface. Nevertheless, if α is not too large, the thermal effects still dominate. In such a case, a liquid-like (high-density) phase which is striped then coexists with its gas (low density phase). With a further increase

²Although, of course, the equilibrium critical temperature depends on α , but not the critical properties. The α DLG belongs to the Ising universality class for all α .

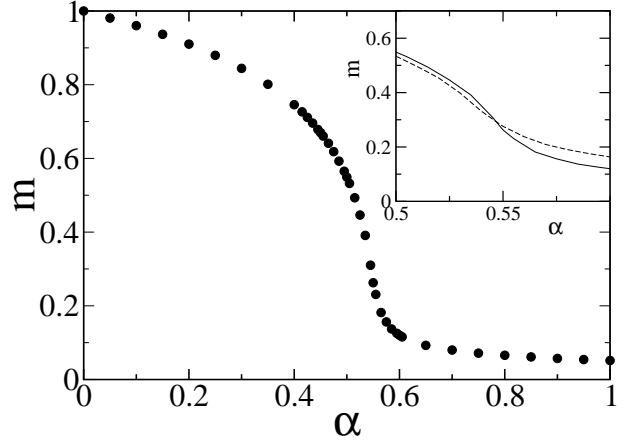


Figure B.2: The α -dependence of the order parameter m defined in Eq. (B.3) for half-filled lattices. The main graph shows the results from MC simulations for $L_{\parallel} \times L_{\perp} = 256 \times 256$. The inset shows a zooming of the transition region for system sizes $L_{\parallel} \times L_{\perp} = 128 \times 128$ (dashed line) and $L_{\parallel} \times L_{\perp} = 256 \times 256$ (solid line).

in α , the thermal effects are overweighted by the field effects and the interface becomes unstable. This results in fully disordered configurations (single gas-like phase). The transition between ordered and disordered states are rather sharp, which suggest a phase transition. This is confirmed. We found a *topological* (α -induced) extraordinary phase transition, which is found to be continuous (second order). In order to understand this second order phase transition, we introduce an order parameter. One quantity that has been used as a measure of order in the two-dimensional DLG and some related systems [11] is

$$m = \frac{1}{2\sqrt{\rho(1-\rho)}} \sqrt{|\langle M_{\parallel} \rangle - \langle M_{\perp} \rangle|}, \quad (\text{B.3})$$

where M_{\parallel} and M_{\perp} are squared longitudinal and transverse *magnetizations* given by,

$$M_{\parallel(\perp)} = \frac{1}{L_{\parallel} \times L_{\perp} \times L_{\parallel(\perp)}} \sum_{\mathbf{y}(\mathbf{x})} \left[\sum_{\mathbf{x}(\mathbf{y})} (1 - 2\sigma_{\mathbf{x},\mathbf{y}}) \right]^2, \quad (\text{B.4})$$

respectively, where \mathbf{x} and \mathbf{y} denote the principal lattice directions, and ρ the systems density $\rho = N/(L_{\parallel}L_{\perp})$. The order parameter m is a measure of the difference between the densities of the liquid (strip-like) and gas phases: one has $\langle M_{\parallel} \rangle = \langle M_{\perp} \rangle$ when configurations are fully disordered (as if $T = \infty$), which implies $m = 0$, while $\langle M_{\parallel} \rangle \rightarrow 1$ and $\langle M_{\perp} \rangle \rightarrow 0$ in the limit of $T = 0$ leading to $m \rightarrow 1$. We computed the order parameter m for different values of α . Figure B.2 shows how m varies between these two limits as a function of α . As

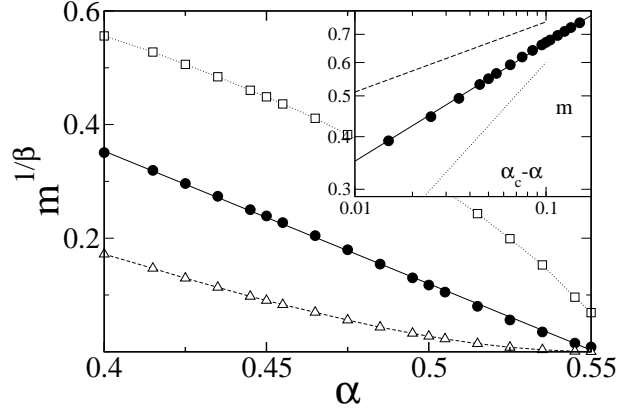


Figure B.3: The main graph shows plots of $m^{1/\beta}$ for different values of β : $1/2$ (squares) and $1/6$ (triangles); this gives a the straight line only for $\beta \approx 0.28$ (circles). The inset is a Log-Log plot assuming $\alpha_c = 0.550 \pm 0.004$ which gives $\beta \approx 0.28$. Lines of slope $1/2$ (dotted line) and $1/6$ (dashed line) are also shown.

observed in Fig. B.2, the transition from a stable interface (high m regime) into a unstable one (low m regime) is rather sharp. As a matter of fact, due to the finite size effects some smoothness is introduced in the critical region (see the inset in Fig. B.2). It seems natural to try the power law behavior

$$m \approx A |\alpha_c - \alpha|^\beta \quad \text{as} \quad \alpha \rightarrow \alpha_c \text{ (from below)}. \quad (\text{B.5})$$

With this aim, we try to identify a value of α_c with the familiar Log-Log plots, which yields a linear region (see inset in Fig. B.3). The slope near α_c corresponds to β . Alternatively, one may plot m raised to the power of $1/\beta$ versus α for different trials values of β , looking for also straight lines. This is also shown in Fig. B.3. The latter procedure has the advantage that no guess for α_c that might introduce further errors is involved. Both methods indicate that the data are consistent with Eq. (B.5). The estimates obtained from this analysis are $\alpha_c = 0.550 \pm 0.04$ and $\beta = 0.28 \pm 0.02$.

This connectivity-induced (nonequilibrium) phase transition characterizes the balance between thermal and field effects and describes the stability of the interface in the α DLG and related models. That is, for low enough connectivities the α DLG is well ordered (the thermal effects dominate, and the interface is stable; this is indeed the case of the standard DLG), whereas for connectivities above the critical point the system exhibits disordered configurations (thermal effects are outweighed by field effects, and therefore the interace is unstable, as the NDLG). This second order (continuous) phase transition indicates that the temperature-field balance is not as trivial as the microscopic dynamic (by the Metropolis rate Eq. (B.2)) may suggest, i.e., a mere linear superposition, which in particular would had led to a linear behavior in Fig. B.2. On the contrary, this is a clear expression of complexity originated in the cooperative behavior.

Appendix C

Detailed derivation of a mesoscopic equation for the Driven Lattice Gas with next-nearest-neighbor Interactions

In this appendix we detail the derivation the (mesoscopic) Langevin-type equation for the *Driven Lattice Gas* with next-nearest-neighbor interactions (NDLG) introduced in Chapter 3. We employ and extend the method introduced in Ref. [80] for the *Driven Lattice Gas* with nearest-neighbor couplings (DLG).

The original microscopic model consists of a two-dimensional lattice, whose sites have occupation variables $\sigma_i = 1$ or 0 , for site i . These variables evolve following a particle-hole exchange dynamics. Let us define at each point $\mathbf{r} \in \mathbb{Z}^2$ a density variable, $\phi_{\mathbf{r}} \in \mathbb{R}$, which is the averaged value of the occupation variables σ_i in a region of volume v around \mathbf{r} . The system evolves from a given configuration γ to another γ' by choosing at random a particle at point \mathbf{r} and exchanging it with next nearest neighbor in the μ direction at time t , namely

$$\phi'_{\mathbf{r}} = \phi_{\mathbf{r}} + v^{-1} (\delta_{\mathbf{r}} - \delta_{\mathbf{r}+\mu}) . \quad (\text{C.1})$$

When v is large enough, $\phi_{\mathbf{r}}$ is assumed to be a continuous function of \mathbf{r} , say $\phi(\mathbf{r}, t)$. This represent the coarse grained excess particle density field. So that we have at time t ,

$$\gamma' = \{ \phi(\mathbf{r}) + v^{-1} \nabla_{\mu} \delta(\mathbf{r}' - \mathbf{r}), \text{ where } \phi \in \gamma \} . \quad (\text{C.2})$$

We can also generalized this dynamics to consider exchanges of magnitude γ/v

with probability amplitude, the latter being an even function of η [166], e.g.,

$$f(\eta) = (\delta(\eta + 1) + \delta(\eta - 1)) / 2. \quad (\text{C.3})$$

Or in other words, Eq. (C.3) represents the probability distribution function of a η , amount of mass attempted to be displaced. The configurations η evolves according to a stochastic hopping dynamics which conserves the number of particles, or equivalently the density. That is, configurations have a statistical weight $P(\gamma, t)$, which evolves accordingly to the following continuous *master equation* [1, 2]:

$$\partial_t P(\gamma, t) = \sum_{\mu} \int d\eta f(\eta) \int d\mathbf{r} [\Omega(\gamma \rightarrow \gamma') P(\gamma, t) - \Omega(\gamma' \rightarrow \gamma) P(\gamma', t)], \quad (\text{C.4})$$

where $\Omega(\gamma \rightarrow \gamma')$ stands for the transition probability per unit time (transition rate) from γ to γ' . As usual, the transition rates are given in terms of entropic and energetic contributions as

$$\Omega(\gamma \rightarrow \gamma') = D(\Delta S(\eta)) \cdot D(\Delta H(\eta) + H_\epsilon). \quad (\text{C.5})$$

Here D is a function satisfying the detailed balance constraint, i.e., $D(-x) = e^x D(x)$, which ensures that in the zero field limit ($\epsilon = 0$) the stationary distribution is the equilibrium one, $P_{st} \propto e^{-H}$. ΔH and ΔS are the increment of energy $H(\gamma') - H(\gamma)$ and entropy $S(\gamma') - S(\gamma)$, respectively. At a mesoscopic level, the equivalent to the microscopic Hamiltonian (Eq. (3.1) in Chapter 3) is the standard ϕ^4 (Ginzburg–Landau) Hamiltonian. The structure of the free energy consist of two contributions [33]: entropic and energetic which are given by, respectively

$$\begin{aligned} S(\gamma) &= v \int d\mathbf{r} \left(\frac{\mathbf{a}}{2} \phi^2 + \frac{\mathbf{g}}{4!} \phi^4 \right) \\ H(\gamma) &= v \int d\mathbf{r} \left(\frac{1}{2} (\nabla \phi)^2 + \frac{\tau}{2} \right), \end{aligned} \quad (\text{C.6})$$

where \mathbf{a} and \mathbf{g} are entropic coefficients whereas the parameter τ comes from the energetic functional. Notice that, in Eq. (C.5) the increment of energy from the drive H_ϵ enters the dynamics through $D(\Delta H(\eta) + H_\epsilon)$, where $H_\epsilon = \eta \mu \cdot \epsilon (1 - \phi^2) + \mathcal{O}(v^{-1})$. This means that the transition rates depend on the energy and entropy difference between configurations plus a term H_ϵ whose dominant part in v^{-1} is the natural choice to mirror the effects of the drive as far as it accounts for the local increment of energy due to the driving field. Notice also that the detailed dependence of the coarse-grained field ϵ on the microscopic field introduced in Eq. (3.2) remain still as an open issue [11]. We also assumed the driving field acting along one of the principal lattice directions, say horizontal.

The next step is to get a Fokker-Planck equation by expanding the master equation Eq. (C.4) in v^{-1} up to v^2 order (Kramers–Moyal expansion [1]). To this end, we expand a functional F around γ which read,

$$F(\gamma') = F(\gamma) + \sum_{k=1}^{\infty} \frac{-\eta^k v^{-k}}{k!} \left(\nabla_{\mu} \frac{\delta}{\delta\phi} \right)^k F(\gamma), \quad (\text{C.7})$$

where F is a functional representing either S , H , or P . The operator $\frac{\delta}{\delta\phi}$ means the functional derivative of $F(\phi)$ with respect to ϕ . To be specific, we also choose H_{ε} as

$$H_{\varepsilon}(\gamma' \rightarrow \gamma') = \eta \lambda_{\mu}^{(\varepsilon)} + \sum_{k=1}^{\infty} \frac{(-1)^k \eta^{k+1} v^{-k}}{(k+1)!} \left(\nabla_{\mu} \frac{\delta}{\delta\phi} \right)^k \lambda_{\mu}^{(\varepsilon)}, \quad (\text{C.8})$$

with $\lambda_{\mu}^{(\varepsilon)} = \mu \cdot \varepsilon (1 - \phi(\mathbf{r})^2)$. These expansions yield the following Fokker-Planck equation [80].

$$\begin{aligned} \partial_t P_t = \sum_{\mu} \int d\mathbf{r} \left(\nabla_{\mu} \frac{\delta}{\delta\phi} \right) \times \\ \left[v^{-1} p(\lambda_{\mu}^S, \lambda_{\mu}^H + \lambda_{\mu}^{\varepsilon}) P_t + \frac{1}{2v^2} q(\lambda_{\mu}^S, \lambda_{\mu}^H + \lambda_{\mu}^{\varepsilon}) \left(\nabla_{\mu} \frac{\delta}{\delta\phi} \right) P_t \right], \end{aligned} \quad (\text{C.9})$$

where

$$\begin{aligned} P_t &\equiv P(\gamma, t), \\ \lambda_{\mu}^X &\equiv - \left(\nabla_{\mu} \frac{\delta}{\delta\phi} \right) X, \\ p(z_1, z_2) &\equiv \int d\eta \eta f(\eta) D(\eta z_1) D(\eta z_2), \\ q(z_1, z_2) &\equiv \int d\eta \eta^2 f(\eta) D(\eta z_1) D(\eta z_2). \end{aligned} \quad (\text{C.10})$$

After using standard techniques in the theory of stochastic processes [1] we derive from the Fokker–Planck equation its stochastically equivalent Langevin equation using the Ito prescription, which reads

$$\partial_t \phi(\mathbf{r}, t) = \sum_{\mu} \nabla_{\mu} \left[p(\lambda_{\mu}^S, \lambda_{\mu}^H + \lambda_{\mu}^{\varepsilon}) + q(\lambda_{\mu}^S, \lambda_{\mu}^H + \lambda_{\mu}^{\varepsilon})^{1/2} \xi_{\mu}(\mathbf{r}, t) \right]. \quad (\text{C.11})$$

The time has been rescaled by v^{-1} and $\xi_{\mu}(\mathbf{r}, t)$ is a delta-correlated Gaussian white noise, i.e., $\langle \xi_{\mu}(\mathbf{r}, t) \rangle_t = 0$ and $\langle \xi_{\mu}(\mathbf{r}, t) \xi_{\mu'}(\mathbf{r}', t') \rangle = \delta_{\mu\mu'} \delta(t - t') \delta(\mathbf{r} - \mathbf{r}')$.

We focus on the critical region where large fluctuations on all length scales dominate. Further simplification in Eq. (C.11) is possible in this regime by dropping the irrelevant terms in the renormalization group sense. Following the

standard field theoretic methods let us introduce an external momentum scale τ and make the following anisotropic scale transformations

$$\begin{aligned} \mathbf{t} &\rightarrow \tau^{-z} \mathbf{t}, \\ \mathbf{r}_\perp &\rightarrow \tau^{-1} \mathbf{r}_\perp, \\ \mathbf{r}_\parallel &\rightarrow \tau^{-s} \mathbf{r}_\parallel, \\ \phi &\rightarrow \tau^\delta \phi. \end{aligned} \tag{C.12}$$

Next, we expand the Langevin equation in powers of τ around $\tau = 0$, keeping only the leading terms. For next-nearest-neighbor interactions, the sum \sum_μ involves a sum for each possible direction, namely $\sum_\parallel \sum_\perp \sum_{/} \sum_{\backslash}$ which are respectively the parallel, transverse, and the two diagonals directions. After some cumbersome algebra, one can split the terms depending on both diagonal ($/$ and \backslash) into the two parallel and transversal to the driving field ε components. The time scale, the transverse noise, and the transverse spatial interaction are forced to remain invariant under transformation. With this, one gets $z = 4$ and $\delta = (s + d - 3)/2$. Different scenarios are now possible depending on the value of s . Demanding that the most relevant terms in the parallel and transverse to the field scale in the same way, as in the standard analysis of the critical behavior of the NDLG (see subsection 3.3.2), would lead to $s = 2$. According to this, the Langevin equation for finite (coarse-grained) driving field contains a large bunch of ε -dependent terms. Similarly to what occurs in Ref. [80], just taking a large enough value of the driving field most of those terms vanish. By doing this, one is led to the following Langevin equation

$$\partial_t \phi(\mathbf{r}, \mathbf{t}) = -\nabla_\perp^4 \phi + \left(\tau + \frac{3}{2} \mathbf{a}\right) \nabla_\perp^2 \phi + \frac{\mathbf{g}}{4} \nabla_\perp^2 \phi^3 + \mathbf{a} \nabla_\parallel^2 \phi + \xi(\mathbf{r}, \mathbf{t}) \tag{C.13}$$

The resulting Langevin equation is analogous to the one for nearest-neighbor interactions (see Eq. (3.10) in Chapter 3), although Eq. (C.13) contains additional entropic, not energetic, contributions due to the presence of larger number of bonds than in the NN case.

Appendix D

Hydrodynamic description for a three-dimensional granular gas: Clustering and symmetry breaking

A straightforward extension to three dimensions of the circular system studied in Chapter 7 is a *cylinder* in which the curved wall is maintained at a constant temperature and the other two are elastic (see Fig. D.1). Particles of diameter d move inside the cylinder undergoing inelastic collisions with a constant restitution coefficient μ . In this appendix we study the clustering and symmetry-breaking instabilities employing granular hydrodynamics in such a geometry. To this end, we generalize the Grossman *et al.* [154] constitutive relations to three-dimensional situations.

Constitutive Relations. Before go further, we derive heuristic constitutive relations for inelastic gases in three dimensions employing free volume arguments in the vicinity of the close packing, and suggest an interpolation between the close-packing limit and the usual dilute-limit relations. We follow here the strategy taken by Grossman *et al.* [154] in two dimensions.

Let us consider our three-dimensional system, in which there is a temperature gradient in the radial direction because of the thermalized wall (set at temperature T_0). As a result, there will be an energy flux along this direction. Consequently —assuming both azimuthal and longitudinal symmetry, i.e, the state do not depend neither θ nor x —, the energy balance equation, which is derived from the hydrostatic version of Eqs. (5.1), reduces to

$$\frac{1}{r} \frac{d}{dr} \left(r \kappa \frac{dT}{dr} \right) = I, \quad (\text{D.1})$$

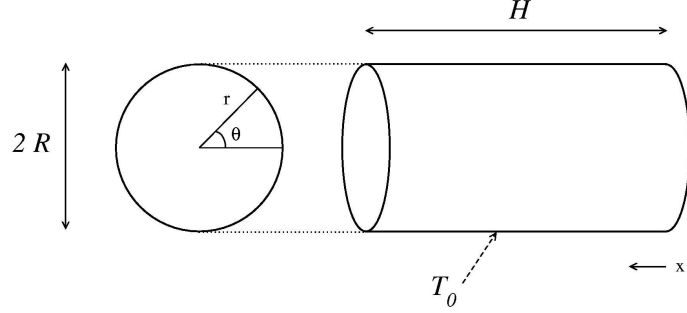


Figure D.1: A perspective sketch of a cylinder of volume πHR^2 . The curved surface is thermalized to temperature T_0 whereas the remaining two surfaces are considered elastic. Definition of the cylindrical coordinates, which we will employ along this appendix, are also indicated.

where I is the sink term (mean energy lost per unit volume per unit time) and κ is the coefficient of thermal diffusivity. Constitutive relations for I and κ are estimated heuristically following the approach devised in Ref. [154], yielding the same expressions as in Eq. (7.3). These are

$$\begin{aligned}\kappa &= \frac{\sigma n (\alpha l + d)^2 T^{1/2}}{l}, \text{ and} \\ I &= \frac{\sigma}{\gamma l} (1 - \mu^2) n T^{3/2},\end{aligned}\tag{D.2}$$

where α and γ are numerical factors of the order unity. The effect of the system dimensionality enters only in σ and γ , which will differ from the two-dimensional case. Concerning the equation of state in the low density limit, as is well-known, the ideal gas law holds, $P = nT$. Contrary, in the high density limit, the mean free path l is much less than the particle diameter d , that is, $l \ll d$. Thus, one finds

$$\frac{n}{n_c} = \frac{d^3}{(d+l)^3} \approx 1 - \frac{3l}{d}\tag{D.3}$$

where $n_c = \sqrt{2}/d^3$ is the close packing value in three-dimensions [167]. In this limit [154] the entropy per particle is $S \sim \ln(l^3) + g(T)$, with g an arbitrary function of T . Therefore, employing Eq. (D.3) we obtain the pressure in the limit $n \rightarrow n_c$,

$$P = \frac{3n^2 T}{n_c - n}\tag{D.4}$$

We therefore propose the following interpolation formula for the pressure

$$P = nT \frac{n_c + 2n}{n_c - n}.\tag{D.5}$$

The mean free path can be also expressed in terms of the density and temperature. In the dilute limit one has (in three dimensions) $l = 1/(\pi\sqrt{2}nd^2)$, while

from Eq. (D.3) one has in the high density limit

$$l \approx \frac{n_c - n}{3n_c} d. \quad (\text{D.6})$$

Again, by using these limits to interpolate a global expression for the mean free path, we find

$$l = \frac{1}{\pi\sqrt{2}nd^2} \frac{n_c - n}{n_c - \alpha n}, \quad (\text{D.7})$$

where $\alpha = 1 - \frac{3}{2\pi}$.

The Density Equation. Substituting Eqs. (D.2) into Eq. (D.1), and eliminating the temperature dependence with Eqs. (D.5) and (D.7) we arrive to a second order differential equation for n :

$$\frac{1}{r} \frac{d}{dr} \left[r \mathcal{F}(z) \frac{dz}{dr} \right] = \eta \mathcal{Q}(z). \quad (\text{D.8})$$

This is *the density equation*. For convenience, the radial coordinate has been rescaled by R and a normalized inverse density $z(r) = n_c/n$ is introduced. The functions \mathcal{F} and \mathcal{Q} read

$$\begin{aligned} \mathcal{F}(z) &= \frac{(z^2 + 4z - 2) [\alpha z(z - 1) + 2\pi(z - \alpha)]^2}{(z - \alpha)(z - 1)^{1/2} z^{3/2} (z + 2)^{5/2}} \\ \mathcal{Q}(z) &= \frac{(z - \alpha)(z - 1)^{1/2}}{(z + 2)^{3/2} z^{1/2}}, \end{aligned} \quad (\text{D.9})$$

and $\eta = \frac{4\pi^2}{\gamma} (1 - \mu^2) \left(\frac{R}{d}\right)^2$. The fixed total number of particles N yields a normalization condition, which read

$$\int_0^1 z^{-1}(r) r dr = f/2, \quad (\text{D.10})$$

where $f = \frac{N}{\pi\sqrt{2}\Delta} \left(\frac{d}{R}\right)^3$ is the average grain area fraction, and $\Delta = H/R$ the system aspect ratio. Equations (D.8) and (D.10), together with the boundary conditions $dz(0)/dr = 0$ and $z(1) = \text{const}$ form a complete set. The hydrostatic problem is completely determined by three scaled parameters η , f , and Δ . Notice that the definitions of \mathcal{F} , \mathcal{Q} , η , and f differ from the two-dimensional case (see Eqs. (7.7)–(7.8)). Figure D.2 shows the numerical solution of Eq. (D.8). This is actually a one-dimensional solution, which corresponds with the *azimuthally- and longitudinally-symmetric* state. Once the density $z(r) = n_c/n(r)$ is obtained, the temperature profile can be determined from the equation of state (Eq. (D.5)).

Marginal Stability Analysis. In general, Eq. (D.8) provides only one of the possible solutions —actually, a one-dimensional solution—. However, as we

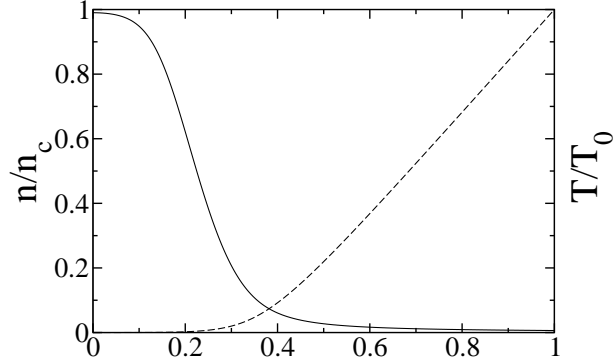


Figure D.2: Scaled temperature (dashed line) and density (solid line) profiles predicted by the hydrostatic theory for $\eta = 10^4$ and $f = 0.036$.

will demonstrate, this system exhibits symmetry-breaking instability¹. That is, there are truly two-dimensional solutions in which the longitudinal symmetry along x is broken. These solutions can be found by linearizing Eq. (D.8) around the one-dimensional solution given by Eqs. (D.8)–(D.10) — a similar analysis was performed in Chapters 6 and 7—. In general, one can rewrite the energy balance equation in terms of the three coordinates r , θ , and x :

$$\nabla \cdot (\mathcal{F}(r)\nabla z) = \eta\mathcal{Q}(z), \quad (\text{D.11})$$

with \mathcal{F} and \mathcal{Q} given by Eq. (D.9). Substituting $z(r, \theta, x) \sim z(r) + \varepsilon\omega(r, \theta, x)$, assuming $\omega = \Xi(r)\Pi(\theta)\Phi(x)$, and linearizing Eq. (D.11) with respect to the small correction ε , one obtains:

$$\begin{aligned} \Phi(x) &= A \sin(mx) + B \cos(mx), \quad x \in [0, \Delta] \\ \Pi(\theta) &= C \sin(k\theta) + D \cos(k\theta), \quad \theta \in [0, 2\pi] \\ \Gamma'' + \frac{1}{r}\Gamma' - \left(m^2 + \frac{k^2}{r} + \frac{\eta\mathcal{Q}'}{\mathcal{F}} \right) \Gamma &= 0, \quad r \in [0, 1], \end{aligned} \quad (\text{D.12})$$

where A, B, C , and D are constants, and m and k are, respectively, the longitudinal and azimuthal wave number determined by the boundary conditions. Here, $\Gamma(r) \equiv \Xi(r)\mathcal{F}$, \mathcal{Q}' denotes the z derivative of \mathcal{Q} , and functions \mathcal{F} and \mathcal{Q} are evaluated at $z = z(r)$. For fixed values of η and f , Eq. (D.12) and the boundary conditions

$$\Phi'(0) = \Phi'(\Delta) = 0 \quad (\text{D.13})$$

represent a linear eigenvalue problem for k and m . We focus here only in the longitudinal wave number m , so that $m = j\pi/\Delta$, where $j \in \{0, \mathbb{N}\}$ because of the boundary conditions Eq. (D.13). That is, we solve numerically the eigenvalue problem for $k = 0$. If there are nontrivial solutions for the lowest mode $k = 0$ then there will be solutions for higher modes. Moreover, in

¹This is in contrast with its two-dimensional counterpart, previously studied in Chapter 7.

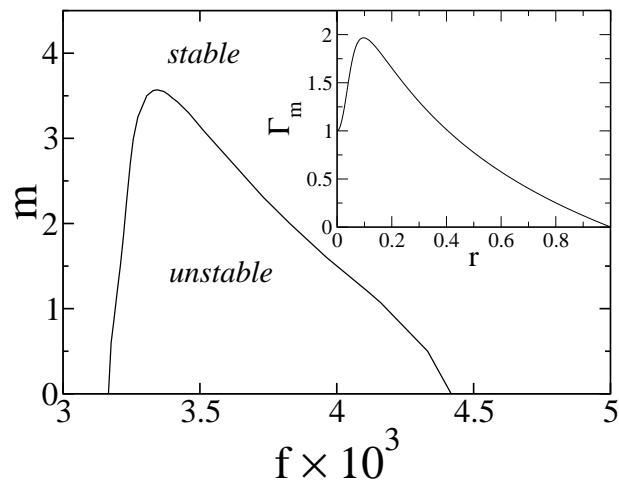


Figure D.3: Main graph: Marginal stability curve $m = m(f)$ for $\eta = 10^5$. The symmetry-breaking instability develops in the parameter region above this curve. Inset: Eigenfunction $\Gamma_m(r)$ corresponding to the eigenvalue $m = 0.585$ for $\eta = 10^5$ and $f = 2.16 \cdot 10^{-3}$.

Chapter 7 we proved the stability of the azimuthally-symmetric state —against linear perturbations—, hence one expects that the azimuthal wave number k does not play a relevant role here. The symmetry breaking instability along the longitudinal (not azimuthal) direction is confirmed. Figure D.3 shows the marginal stability curve $m = m(f)$ found numerically. For a fixed value of η the azimuthally- and longitudinally-symmetric state is *unstable* (*stable*) for any m below (above) the marginal stability curve. Interestingly, the symmetric state remains stable for any m beyond a finite interval of $f \in (f_{\min}, f_{\max})$. Or in other words, for each aspect ratio $\Delta > \Delta_{\text{crit}} = \pi j/m$, where $j = 0, 1, 2, \dots$, the symmetric state loses stability with respect the longitudinal mode j [159].

Therefore, granular hydrodynamics, employing our heuristic constitutive relations —an extension of the Grossman *et al.* approach to three-dimensional cases—, may be a good candidate to describe the clustering and symmetry-breaking instabilities which may occur in inelastic hard-sphere systems.

Part IV

Conclusions

Conclusions and future work

Unfortunately, despite of the much research efforts, a rigorous statistical-mechanical description of nonequilibrium instabilities remains still elusive. The work presented here goes deep into the nonequilibrium realm, aiming for a new effort towards better understanding basic features of nonequilibrium phase transitions. Indeed, the study of *driven diffusive fluids* and *driven granular gases*, besides its technological importance, is of general interest because it will contribute to the rationalization of nonequilibrium phenomena. The emphasis in our investigations is on the study—in most cases at different levels of description, namely, macroscopic, mesoscopic, and microscopic—of the instabilities which occur in those systems. This task were carried out with both state-of-the-art and novel theoretical and computational techniques in statistical physics.

This thesis was structured in four parts. The first part, which comprises Chapters 2, 3, and 4, was devoted to the early-time kinetic and steady state properties of *driven diffusive fluids*; the Part II (Chapters 5, 6, and 7) dealt with both the atomistic and macroscopic description of two-dimensional driven *inelastic* gases; finally, Appendices A, B, C, and D were enclosed in Part III. In what follows (Part IV), we summarize the main results and the original contributions contained in this work. We also give an outlook for principal issues to be investigated in future work.

Chapter 1. In the first chapter we reviewed the general features, phenomenology, and open issues of the class of systems which we are dealing with in the text from a mechanical-statistical point of view. Likewise we remarked the subject of this thesis as well as the main motivation behind it.

Chapter 2. In this chapter we presented the model—i.e., the *driven lattice gas* (DLG)—which was the prototype for *driven diffusive fluids*, and summarized some of its already known, unusual properties and controversies. The relevant background for Chapters 3 and 4 is also provided. This comprises state-of-the-art simulation schemes (lattice and off-lattice Metropolis *Monte Carlo*) as well as field-theoretical approaches (statistical field theories).

Chapter 3. We have described Monte Carlo simulations and field theoretical calculations that aim at illustrating how slight modifications of dynamics at the microscopic level may influence, even quantitatively, both the resulting nonequilibrium steady state and the kinetic properties. With this aim, we took as a reference the DLG. We introduced related lattice and off-lattice microscopic models in which particles, as in the DLG, interact via a local anisotropic rule. The rule induces preferential hopping along one direction, so that a net current sets in if allowed by boundary conditions. In particular, we have discussed on the similarities and differences between the DLG and its continuous counterpart, namely, a Lennard–Jones analogue in which the particles’ coordinates vary continuously. A comparison between the two models allowed us to discuss some exceptional, hardly realistic features of the original discrete system—which has been considered a prototype for nonequilibrium anisotropic phase transitions (although we claim here is not justified). We outline the main conclusions as follows:

- We found that the continuous, off-lattice model closely resembles the DLG in that both depict a particle current, a highly anisotropic liquid-vapor interface which extends along the field direction, and the corresponding second order phase transition.
- However, they differ in some essential features. Contrary to the DLG, its off-lattice counterpart shows a transition temperature which decreases with the field strength. Moreover, unlike for the DLG, there is no phase transition for a large enough field. Concerning the early process of kinetic ordering, early-time anisotropies in the off-lattice case point along the field, contrary to the ones observed in the discrete DLG.
- These observations suggest that the DLG behavior is highly conditioned by the lattice geometry, which acts more efficiently in the DLG as an ordering agent than the field itself. Therefore, the striking, counterintuitive feature of the DLG that a strong field raises the critical temperature above the equilibrium one is a *geometrical* effect—induced by the lattice topology—rather than *dynamic*.
- In particular, it ensues that, due to its uniqueness, the DLG does not have a simple off-lattice analog.
- In order to deepen in this situation, we studied the DLG with an infinite drive extending hops and interaction to next-nearest-neighbors (this model was named NDLG). We confirmed that the NDLG behaves closer to the off-lattice case: the critical temperature decreases with the field and early-time anisotropies point along the field.
- However, we found that allowing jumping along intermediate directions leaves invariant both spatial correlations and criticality. The former was

monitored by the two-point correlation function and the equal-time structure factor, whereas the latter was determined by standard finite size scaling, and corroborated by the *anisotropic driven system* (ADS) (mesoscopic) approach.

- Therefore, allowing jumping along intermediate directions modifies essentially the phase diagram—which is not determined by bare symmetry arguments—but not features (such as generic power-laws in spatial correlations) that seem intrinsic of the nonequilibrium nature of the phenomenon.

These conclusions are properly complemented by the results obtained in the Chapter 4 on criticality in a related off-lattice model. Moreover, we believe that the fact that particles are constrained to travel along discrete lattice directions may condition not only the DLG's properties, but also the properties of many other lattice models. Further research, which is going on at present, confirms this on the off-lattice versions of the *Time Asymmetric Exclusion Process* [16, 57] (TASEP), and of the DLG with nearest neighbor *repulsion* [91, 93]. Further issues are the characterization of the stability of the interface under strong fields (see Appendix B), and the study of the early-time kinetic of phase separation in the NDLG from the field-theoretical point of view, by using the successful ADS approach.

Chapter 4. Since the DLG was shown in Chapter 3 to be unrealistic in some essential sense, we introduced here a novel, *realistic* off-lattice driven fluid, which is a candidate to portray some of the anisotropic behavior in nature. This is a nonequilibrium Lennard-Jones fluid with an external constant driving field, settled on a thermal bath. We studied short-time kinetic and steady-state properties of its non-equilibrium phases, namely, solid (mono- and polycrystalline), liquid and gas anisotropic phases. Specifically, we described the early-time segregation process as monitored by the excess energy, which measures the droplets surface; structural properties of the steady state, namely, the radial and azimuthal distribution functions, and the degree of anisotropy; transport properties; and also an accurate estimate of the liquid-vapor coexistence curve and the associated critical indices. The principal conclusions are:

- This model seems to contain the necessary essential physics to be useful as a prototypical model for anisotropic behavior in nature.
- This case is more convenient for computational purposes, than others such as, for instance, standard molecular-dynamics realizations of driven fluid systems.
- This is the natural extension to nonequilibrium anisotropic cases of the familiar Lennard-Jones fluid, which has played an important role in analysing equilibrium fluids. Indeed, our model reduces to the (equilibrium) Lennard-Jones fluid for zero field. Otherwise, it exhibits a net current, and striped structures below a critical point.

- Concerning kinetics properties, in spite of the anisotropy of the late-time “spinodal decomposition” process, earlier nucleation seems to proceed by *Smoluchowski coagulation* and *Ostwald ripening*, which are known to account for nucleation in equilibrium, isotropic lattice systems and actual fluids.
- Unexpectedly, we have also found that the model critical behavior is consistent with the Ising, equilibrium one but not with the one for the DLG. The main reason for this and other disagreements discussed in this chapter might be the particle-hole symmetry violation in the driven Lennard-Jones fluid.
- In addition, regarding the modeling of complex systems, one may infer that spatial discretization may change significantly not only morphological and early-time kinetics properties, but also critical properties. This is in stark contrast with the concept of universality in equilibrium systems, where critical properties are independent of dynamic details.
- Finally, we believe this model will motivate new experiments on anisotropic spinodal decomposition besides theoretical work. In fact, our observations on the early-time separation process and structural properties are easily accessible by micro calorimetric and spectroscopy experiments, for instance.

Many other issues remain. Further research, which are going on at this moment, involve detailed studies of its interfacial properties, the role of the finite size effects, and sheared versions of this driven Lennard-Jones fluid. Other questions which we would like to raise for future work is how do the particle-hole symmetry and the shape of the interaction potential influence the critical properties. A detailed analysis of the late-time segregation process, which has already been studied for both equilibrium [107, 108] and non-equilibrium cases, including the DLG [103, 109], will be the subject of future investigations. Also interesting is the detailed study of the structure and morphological features of the (monocrystalline) solid and glass-like (polycrystalline solid) phases. The fact that our off-lattice model and a related driven-diffusive model [91] exhibit a critical behavior consistent with Ising is rather remarkable, and merits further investigations.

Chapter 5. In this chapter we have provided the framework relevant to Chapters 6 and 7. We discussed on some unresolved puzzles and recent developments in granular fluids, in particular, on the applicability of granular hydrodynamics to granular flows. We also presented the basic ingredients of the studied models and the computer simulation methods (event-driven molecular dynamics).

Chapter 6. We have described hydrodynamic derivations as well as event-driven molecular dynamics simulations in a monodisperse granular gas confined in an annulus, the inner circle of which represents a “thermal wall”. The quasi-elastic limit was considered, and the granular hydrodynamics with Enskog-type

transport coefficients [135] was employed. We performed a comprehensive study of the clustering, symmetry breaking and phase separation instabilities, which enable us to establish a detailed phase diagram. To test and complement our theoretical predictions we performed event-driven molecular dynamics simulations of this system. This led us to discuss on the physics of the instabilities which occur in this model. Here we itemize the main conclusions:

- The zero-flow regime was completely determined by three scaled parameters: the grain area fraction, the inelastic heat loss parameter, and the aspect ratio of the annulus.
- In our event-driven molecular dynamics simulations, azimuthally symmetric steady states were observed far from the driving wall. In spite of the small number of particles employed, these *annular states* were accurately described by the numerical solutions of our granular hydrostatic equations.
- A marginal stability analysis yielded a region of the (three-dimensional) parameter space where the annular state—the basic, azimuthally symmetric steady state of the system—is unstable with respect to small perturbations which break the azimuthal symmetry. We computed the marginal stability curves and compared them to the borders of the spinodal (negative compressibility) interval of the system.
- We found that, the physical mechanism of the phase separation *instability* is the negative compressibility of the granular gas in the azimuthal direction, caused by the inelastic energy loss. Mathematically, phase separation manifests itself in the existence of *additional* solutions to the *density equation* in some region of the parameter space.
- Our event-driven simulations of this system also showed phase separation, but it is masked by large spatio-temporal fluctuations. By measuring the probability distribution of the amplitude of the fundamental Fourier mode of the azimuthal spectrum of the particle density we were able to clearly identify the transition to phase separated states in the simulations.
- We found that the instability region of the parameter space, predicted from hydrostatics, is located within the phase separation region observed in our simulations. This implies the presence of a binodal (coexistence) region, where the annular state is *metastable*.
- Clustering, symmetry breaking, and phase separation instabilities should be observable in actual experiments. In fact, the model we proposed is experimentally accessible, and, therefore, if brought to the attention of the appropriate community, might stimulate experimental work on these instabilities.

Of course, it would be interesting to test the predictions of our theory/simulations in experiment. By focusing on the annular geometry, we hope to motivate experimental studies of these granular instabilities which may be advantageous

in this geometry. The annular setting avoids lateral side walls (with an unnecessary/unaccounted for energy loss of the particles). A possible experiment can employ metallic spheres rolling on a slightly concave smooth surface and driven by a rapidly vibrating (slightly eccentric and possibly rough) interior circle. While particle rotation and rolling friction may become important, we expect that the main predictions of the theory will persist. It would be also interesting to determine the nature (sub- or supercritical?) of the solutions which bifurcate from the azimuthally symmetric state. Further studies may exploit the similarities between the phenomenology observed in our model system and the one in planetary rings, in which clustering, spontaneous symmetry breaking, oscillations, and many other instabilities occur.

Chapter 7. In this chapter we addressed granular hydrodynamics and fluctuations in a simple two-dimensional granular system under conditions when first-principle hydrodynamic descriptions break down because of large density, *not* large inelasticity. We put it into a test —using event-driven molecular dynamics simulations— in an extreme case when granular clusters with the maximum density close to the hexagonal close packing form (we defined them as *macro-particles*). The model system we considered here, comprises inelastically colliding hard disks enclosed by circular boundaries, driven by a thermal wall at zero gravity. The main conclusions are summarized as follows:

- Molecular dynamics simulations showed a sharp-edged close-packed cluster (macroparticle) of an almost circular shape, weakly fluctuating in space and isolated from the thermal wall by a low-density gas. This is due to collisional cooling. The macroparticle formation requires a certain number of particles, and, as the particle density is increased, the transition from a (quasi-) homogeneous state to a macroparticle is rather sharp.
- We were able to solve numerically a set of granular hydrostatic equations which employ the constitutive relations by Grossman *et al.* [154]. We found that the density profiles, in a wide range of parameters, agrees almost perfectly —including the close-packed part— with the azimuthally symmetric solution of granular hydrostatic equations. We also showed that, for the same setting, first-principle Enskog-type relations [135] perform poorly.
- This agrees with previous results in rectangular geometry, with and without gravity, and extends the validity of the Grossman *et al.* relations for a slightly lower restitution coefficient, and for the circular geometry.
- A marginal stability analysis have shown —independently of the constitutive relations employed— that there are no steady-state solutions with broken azimuthal symmetry which would bifurcate from the azimuthally symmetric solution. This agrees with the persistence of circular shapes for the macroparticle as observed in our simulations.

- We addressed, for the first time, fluctuations of the macroparticles, by measuring the radial probability distribution function of the center of mass of the system. These fluctuations turn out to be Gaussian.
- The observed Gaussian fluctuations of the center of mass suggest an effective Langevin description in terms of a macroparticle in a confining potential of hydrodynamic nature, driven by discrete particle noise —i.e., the cluster performs a Brownian motion inside the system. The associated Langevin equation is provided.
- In stark contrast with equilibrium systems, in which the relative magnitude of fluctuations decreases with increasing the number of particles², we found that the fluctuations persist as the number of particle in the system is increased.

There are still many open issues. A question that should be addressed is whether there are additional instabilities in this model system. For instance, an important insight, in analogy with the KTHNY theory [119] of two-dimensional melting (for fluids at thermal equilibrium), might be given by the positional and orientational ordering of the macroparticles at different number densities. This can be achieved by measuring their respective correlation functions. In addition, both a general solution of the time-dependent hydrodynamic equations and a non-linear stability analysis will contribute to the quest. Other future issue may involve the detailed study of instabilities in related three-dimensional systems. An outline can be found in Appendix D. It should be also worthy to study how polydisperse granulates behave in this system.

In spite of appendices are commonly pushed into the background, we think that our Appendices B and D merit their own conclusions.

Appendix B. In this appendix we introduced a driven-diffusive lattice model (the α DLG) which aim at understanding the balance between thermal and field effects which take place in such a models, as the DLG and related models (specifically the models studied in Chapter 3). This balance can be understood in terms of stability of the interface between the condensed and vapor phases—which are elongated along the field direction—. Thermal effects favor the stability (the order) of the interface, whereas the driving effects would drive particles out of the interface favoring disorder. We studied this *dynamic* balance in the extreme case of saturating field, zero temperature limit. The main results are:

- Our model undergoes a second-order phase transition employing as order parameter the measure of the *ordering on the lattice* as a function of the *effective connectivity*. That is, for low enough connectivities the system is well ordered (the thermal effects dominate, and the interface is stable),

²For an ideal gas in equilibrium: $\sigma \sim \mathcal{O}(N^{-1/2})$, where σ is the relative magnitude of fluctuations and N is the number of particles.

whereas for connectivities above the critical point α_c the system exhibits disordered configurations (thermal effects are outweighed by field effects, and therefore the interface is unstable).

- We computed the critical indexes associated with the transition.
- This second order (continuous) phase transition indicates that the temperature-field balance is not as trivial as the microscopic dynamic may suggest, i.e., a mere linear superposition [54]. On the contrary, this is a clear expression of complexity originated in the cooperative behavior.

Appendix D. The last appendix addressed clustering and symmetry-breaking instabilities in a monodisperse gas of inelastic hard spheres confined in a cylinder, the curved wall of which represents a “thermal wall”. We employed a set of granular hydrodynamic equations with heuristic constitutive relations, which we derived from free-volume arguments. This model is a simple extension for three-dimensional cases of the circular system studied in Chapter 7.

- Following the Grossman *et al.* [154] strategy, we proposed phenomenological expressions for the equation of state and the transport coefficients for three-dimensional cases. We employed free-volume arguments in the vicinity of the close packing, and suggested an interpolation between the hexagonal-packing limit and the well-known low density relations.
- The stationary solutions of the granular hydrodynamic equations predict symmetric clustered states far from the thermal wall. Some of the solutions bifurcate from the (steady-state) symmetric solution, i.e., hydrodynamic also predicts the existence of broken-symmetry states. The presence of symmetry breaking instability in this system is in contrast with our findings in its two-dimensional counterpart (see Chapter 7) in which no symmetry breaking instability was found.
- Granular hydrodynamics, employing our heuristic constitutive relations may be a good candidate to describe the clustering and symmetry-breaking instabilities which may occur in inelastic hard-sphere systems.

Published work

- Manuel Díez-Minguito, Pedro L. Garrido, and Joaquín Marro, *Lennard-Jones and lattice models of driven fluids*, Phys. Rev. E **72**, 026103 (2005).
- Joaquín Marro, Pedro L. Garrido, and Manuel Díez-Minguito, *Nonequilibrium anisotropic phases, nucleation and critical behavior in a driven Lennard-Jones fluid*, Phys. Rev. B **73**, 184115 (2006).
- Manuel Díez-Minguito, Pedro L. Garrido, and Joaquín Marro, *Lattice versus Lennard-Jones models with a net particle flow in Traffic and Granular Flows '05*, in press (Springer, Berlin, 2006).
- Baruch Meerson, Manuel Díez-Minguito, Thomas Schwager, and Thorsten Pöschel, *Close-packed granular clusters: hydrostatics and persistent Gaussian fluctuations*, submitted to Europhys. Lett. (2006)
- Manuel Díez-Minguito, J. Marro, and P. L. Garrido, *On the similarities and differences between lattice and off-lattice models of driven fluids* in *Workshop on Complex Systems: New Trends and Expectations*, to be published in Euro. Phys. J.-Special Topics (2006).
- Manuel Díez-Minguito and Baruch Meerson, *Phase separation of a driven granular gas in annular geometry*, submitted to Phys. Rev. E (2006).

ABSTRACTS

- Manuel Díez-Minguito, Pedro L. Garrido, Joaquín Marro, and Francisco de los Santos, *Driven two-dimensional Lennard-Jones fluid* in *Modeling Cooperative Behavior in the Social Sciences*, P. L. Garrido, J. Marro, M. A. Muñoz (eds.), AIP Conference Proceedings **779**, 199 (2005).
- Manuel Díez-Minguito, Pedro L. Garrido, Joaquín Marro, and Francisco de los Santos, *Simple computational Lennard-Jones fluid driven out-of-equilibrium*, in *XIII Congreso de Física Estadística FISES'05*, Abstract Book (2005).
- Manuel Díez-Minguito and Baruch Meerson, *Phase separation of a driven granular gas in annular geometry*, in *XIV Congreso de Física Estadística FISES'06*, Abstract Book (2006).

IN PREPARATION

- Manuel Díez-Minguito, A. Achahbar, Pedro L. Garrido, and Joaquín Marro, *Langevin-type description for the driven lattice gas with next-nearest-neighbor dynamics* (2006).
- Manuel Díez-Minguito and Thorsten Poeschel, *On the validity of global equations of state for driven granular gases* (2006).
- Manuel Díez-Minguito, Pedro L. Garrido, and Joaquín Marro, *Interfacial properties in a nonequilibrium microfluidic system* (2006).

The author acknowledge financial support from the Spanish Ministry for Science (MEC) and FEDER (project FIS2005-00791).

Bibliography

- [1] N. G. van Kampen, *Stochastic Processes in Chemistry and Physics*, (North Holland, Amsterdam, The Netherlands, 1981).
- [2] C. W. Gardiner, *Handbook of Stochastic Methods for Physics, Chemistry and the Natural Sciences*, (Springer, Berlin, Germany, 2004).
- [3] R. Balescu, *Equilibrium and Nonequilibrium Statistical Mechanics*, (John Wiley & Sons, New York, U.S.A., 1975); K. Huang, *Statistical Mechanics*, (John Wiley & Sons, New York, U.S.A., 1987).
- [4] J. Biel, *Formalismo y Métodos de la Termodinámica*, (Editorial Reverté, Barcelona, Spain, 1998).
- [5] O. Lioubashevski, Y. Hamiel, A. Agnon, Z. Reches and J. Fineberg, *Oscillations and propagating solitary waves in a vertically vibrated colloidal suspension*, Phys. Rev. Lett. **83**, 3190 (1999).
- [6] N. Goldenfeld and L. P. Kadanoff, *Simple lessons from complexity*, Science **284**, 87 (1999).
- [7] M. C. Cross and P. C. Hohenberg, *Pattern formation outside of equilibrium*, Rev. Mod. Phys. **65**, 851 (1993).
- [8] J. P. Gollub and J. S. Langer, *Pattern formation in nonequilibrium physics*, Rev. Mod. Phys. **71**, S396 (1999).
- [9] A.-L. Barabási and H. E. Stanley, *Fractals Concepts in Surface Growth*, (Cambridge University Press, Cambridge, U.K., 1995).
- [10] P. Bak, *How Nature Works: The Science of Self-Organised Criticality*, (Copernicus, New York, U.S.A., 1996).
- [11] J. Marro and R. Dickman, *Nonequilibrium Phase Transitions in Lattice Models*, (Cambridge University Press, Cambridge, U.K., 1999).
- [12] H. Haken, *Cooperative phenomena in systems far from thermal equilibrium and in nonphysical systems*, Rev. Mod. Phys. **47**, 67 (1975).

-
- [13] *Far from Equilibrium Phase Transitions*, Sitges Conference 1988, edited by L. Garrido, (Springer Verlag, Berlin, Germany, 1989).
- [14] S. R. de Groot and P. Mazur, *Non-Equilibrium Thermodynamics*, (Dover Publications, Inc., New York, U.S.A., 1984).
- [15] B. Schmittmann and R. K. P. Zia, in *Statistical Mechanics of Driven Diffusive Systems* in Phase Transitions and Critical Phenomena, Vol. 17, edited by C. Domb and J. L. Lebowitz (Academic, London, U.K., 1996).
- [16] T. M. Liggett, *Interacting Particle Systems*, (Springer Verlag, Heidelberg, Germany, 1985).
- [17] V. Privman, *Nonequilibrium Statistical Mechanics in One Dimension*, (Cambridge University Press, Cambridge, U.K., 1996).
- [18] B. Chopard and M. Droz, *Cellular Automata Modeling of Physical Systems*, (Cambridge University Press, Cambridge, U.K., 1998).
- [19] H. Hinrichsen, *Non-equilibrium critical phenomena and phase transitions into absorbing states*, Adv. Phys. **49**, 815 (2000).
- [20] G. Ódor, *Universality classes in nonequilibrium lattice systems*, Rev. Mod. Phys. **76**, 663 (2004).
- [21] C. P. Ferreira and J. F. Fontanari, *Nonequilibrium phase transitions in a model for the origin of life*, Phys. Rev. E **65**, 021902 (2002).
- [22] A. Treves and Y. Roudi, in *Methods and Models in Neurophysics*, Les Houches School 2003, (Elsevier, 2005).
- [23] T. Vicsek, A. Czirók, E. Ben-Jacob, I. Cohen, and O. Shochet, *Novel type of phase transition in a system of self-driven particles*, Phys. Rev. Lett. **75**, 1226 (1995); J. Toner and Y. Tu, *Long-range order in a two-dimensional dynamical XY model: How birds fly together*, Phys. Rev. Lett. **75** 4326 (1995).
- [24] I. Rodríguez-Iturbe and A. Rinaldo, *Fractal River Basins: Chance and Self-Organization*, (Cambridge University Press, New York, U.S.A., 1997).
- [25] J. L. Cardy, *Field theoretic formulation of an epidemic process with immunisation*, J. Phys. A: Math. Gen. **16**, L709 (1983); J. L. Cardy and P. Grassberger, *Epidemic models and percolation*, J. Phys. A **18**, L267 (1985); H. K. Janssen, Z. Phys. B: Condens. Matter, *Renormalized field theory of dynamical percolation* **58**, 311 (1985).
- [26] K. Nagel and M. Schreckenberg, *A cellular automaton model for freeway traffic*, J. Phys. I (France) **2**, 2221 (1992); D. Chowdhury, L. Santen, and A. Schadschneider, *Statistical physics of vehicular traffic and some related systems*, Phys. Rep. **329**, 199 (2000).

- [27] D. Helbing, *Traffic and related self-driven many-particle systems*, Rev. Mod. Phys. **73**, 1067 (2001).
- [28] H. Berry, *Nonequilibrium phase transition in a self-activated biological network*, Phys. Rev. E **67**, 031907 (2003).
- [29] D. Chowdhury, K. Nishinari, and A. Schadschneider, *Self-organized patterns and traffic flow in colonies of organisms: From bacteria and social insects to vertebrates*, Phase Trans. **77**, 601 (2004).
- [30] B. B. Mandelbrot, *Renormalization and fixed points in finance, since 1962*, Physica A **263**, 477 (1999); R. N. Mantegna and H. E. Stanley, *Introduction to Econophysics: Correlations and Complexity in Finance*, (Cambridge University Press, Cambridge, U.K., 1999); J. P. Bouchaud and M. Potters, *Theory of Financial Risks*, (Cambridge University Press, Cambridge, U.K., 2000).
- [31] L. Onsager, *Crystal statistics. I. A two-dimensional model with an order-disorder transition*, Phys. Rev. **65**, 117 (1944).
- [32] C. J. Thompson, *Mathematical Statistical Mechanics*, (The Macmillan Company, New York, U.S.A., 1972).
- [33] D. J. Amit, *Field Theory, the Renormalization Group and Critical Phenomena*, (World Scientific, Singapore, 1989).
- [34] K. G. Wilson and J. Kogut, *The renormalization group and the ϵ expansion*, Phys. Rep. **12**, 75 (1974).
- [35] S.-K. Ma, *Modern Theory of Critical Phenomena*, (Benjamin, New York, U.S.A., 1976).
- [36] J. J. Binney, N. J. Dowrick, A. J. Fisher and M. E. J. Newman, *The Theory of Critical Phenomena*, (Clarendon Press, Oxford, U.K., 1992).
- [37] H. R. Jaeger, S. Nagel, and R. P. Behringer, *Granular solids, liquids, and gases*, Rev. Mod. Phys. **68**, 1259 (1996); *ibid*, *The physics of granular materials*, Physics Today **49**(4), 32 (1996).
- [38] F. Melo, P. B. Umbanhowar, H. L. Swinney, *Transition to parametric wave patterns in a vertically oscillated granular layer*, Phys. Rev. Lett. **72**, 172 (1994).
- [39] P. B. Umbanhowar, F. Melo, and H. L. Swinney, *Localized excitations in a vertically vibrated granular layer*, Nature **382**, 793 (1996).
- [40] G. H. Ristow, *Pattern Formation in Granular Materials* (Springer Tracts in Modern Physics) (Springer, Berlin, 2000).
- [41] I. S. Aranson and L. S. Tsimring, *Patterns and collective behavior in granular media: Theoretical concepts*, Rev. Mod. Phys. **78**, 641 (2006).

- [42] S. MacNamara and W. R. Young, *Dynamics of a freely evolving, two-dimensional granular medium*, Phys. Rev. E **53**, 5089 (1996); *ibid*, *Kinetics of a one-dimensional granular medium in the quasielastic limit*, Phys. Fluids A **5**, 34 (1993).
- [43] I. Goldhirsch and G. Zanetti, *Clustering instability in dissipative gases*, Phys. Rev. Lett. **70**, 1619 (1993).
- [44] J. S. Olafsen and J. S. Urbach, *Clustering, order, and collapse in a driven granular monolayer*, Phys. Rev. Lett. **81**, 4369 (1998).
- [45] G. W. Baxter, R. P. Behringer, T. Faggert, and G. A. Johnson, *Pattern formation in flowing sand*, Phys. Rev. Lett. **62**, 2825 (1989); X. M. Zheng and J. M. Hill, *Molecular dynamics modelling of granular chute flow: Density and velocity profiles*, Powder Technol. **86**, 219 (1996).
- [46] A. Daerr and S. Douady, *Two types of avalanche behaviour in granular media*, Nature (London), **399**, 241 (1999).
- [47] T. Shinbrot and F. Muzzio, *Noise to order*, Nature (London) **410**, 251 (2001); N. Burtally, P. J. King, and M. R. Swift, *Spontaneous air-driven separation in vertically vibrated fine granular mixtures*, Science **295**, 1877 (2002).
- [48] R. D. Wildman, J. M. Huntley, and D. J. Parker, *Convection in highly fluidized three-dimensional granular beds*, Phys. Rev. Lett. **86**, 3304 (2001).
- [49] X. He, B. Meerson, and Doolen, *Hydrodynamics of thermal granular convection* Phys. Rev. E **65**, 030301 (2002).
- [50] D. Lohse, *el al.*, *Impact on soft sand: Void collapse and jet formation*, Phys. Rev. Lett. **93**, 198003 (2004); D. Lohse, R. Bergmann, R. M. Rauhe, D. van der Meer, *Creating a dry variety of quicksand*, Nature **432**, 689 (2004); see also some nice movies in <http://pof.tnw.utwente.nl/> .
- [51] T. Pöschel and T. Schwager, *Computational Granular Dynamics: Models and Algorithms*, (Springer, Berlin, Germany, 2005).
- [52] E. Ising, *Beitrag zur Theorie des Ferromagnetismus*, Z. Physik **31**, 253 (1925).
- [53] S. Katz, J. L. Lebowitz, and H. Spohn, *Phase transitions in stationary nonequilibrium states of model lattice systems*, Phys. Rev. B **28**, 1655 (1983); *ibid*, *Nonequilibrium steady states of stochastic lattice gas models of fast ionic conductors*, J. Stat. Phys. **34**, 497 (1984).
- [54] N. Metropolis, A. W. Rosenbluth, M. M. Rosenbluth, A. H. Teller, and E. Teller, *Equation of state calculations by fast computing machines*, J. Chem. Phys. **21**, 1087 (1953).

- [55] M. E. J. Newman and G. T. Barkema, *Monte Carlo Methods in Statistical Physics*, (Oxford University Press, Cambridge, U.K., 1995); D. P. Landau and K. Binder, *A Guide to Monte Carlo Simulation in Statistical Physics*, (Cambridge University Press, Cambridge, U.K., 2000).
- [56] S. Geller, *Solid Electrolytes, Topics in Applied Physics*, Vol. **21** (Springer, Heidelberg, Germany, 1977); J. W. Perram, *The Physics of Superionic Conductors and Electrode Materials*, Vol. **15** (Plenum, New York, U.S.A., 1983).
- [57] T. Antal and G. M. Schütz, *Asymmetric exclusion process with next-nearest-neighbor interaction: Some comments on traffic flow and a nonequilibrium reentrance transition*, Phys. Rev. E **62**, 83 (2000).
- [58] D. Helbing, I. J. Farkas, and T. Vicsek, *Freezing by heating in a driven mesoscopic system*, Phys. Rev. Lett. **84**, 1240 (2000).
- [59] M. Aertsens and J. Naudts, *Field-induced percolation in a polarized lattice gas*, J. Stat. Phys. **62**, 609 (1991).
- [60] U. Alon and D. Mukamel, *Gel electrophoresis and diffusion of ring-shaped DNA*, Phys. Rev. E **55**, 1783 (1997).
- [61] D. Beysens and M. Gbadamassi, *Shear-induced effects on critical concentration fluctuations*, Phys. Rev. A **22**, 2250 (1980).
- [62] C. K. Chan, F. Perrot, and D. Beysens, *Experimental study and model simulation of spinodal decomposition in a binary mixture under shear*, Phys. Rev. A **43**, 1826 (1991); T. Baumberger, F. Perrot, and D. Beysens, *Shear flow effects on a critical binary mixture during phase separation*, Physica A **174**, 31 (1991).
- [63] T. Hashimoto, K. Matsuzaka, E. Moses, and A. Onuki, *String phase in phase-separating fluids under shear flow*, Phys. Rev. Lett. **74**, 126 (1995); A. Onuki, *Phase transitions of fluids in shear flow*, J. Phys.: Condens. Matter **9**, 6119 (1997).
- [64] R. G. Larson, *The Structure and Rheology of Complex Fluids*, (Oxford University Press, New York, U.S.A., 1999).
- [65] J. Dzubiella, G. P. Hoffmann, and H. Löwen, *Lane formation in colloidal mixtures driven by an external field*, Phys. Rev. E **65**, 021402 (2002).
- [66] P. M. Reis and T. Mullin, *Granular segregation as a critical phenomenon*, Phys. Rev. Lett. **89**, 244301 (2002).
- [67] P. Sánchez, M. R. Swift, and P. J. King, *Stripe formation in granular mixtures due to the differential influence of drag*, Phys. Rev. Lett. **93**, 184302 (2004).

- [68] C. K. Chan, *Anisotropic phase separation of a nonequilibrium liquid-liquid interface*, Phys. Rev. Lett. **72**, 2915 (1994).
- [69] H. Yizhaq, N. J. Balmforth, and A. Provenzale, *Blown by wind: Nonlinear dynamics of aeolian sand ripples*, Physica D **195**, 207 (2004).
- [70] B. Andreotti, Ph. Claudin, and O. Pouliquen, *Aeolian sand ripples: Experimental study of fully developed states*, Phys. Rev. Lett. **96**, 028001 (2006).
- [71] J. Hoffman *et al.*, *A four unit cell periodic pattern of quasi-particle states surrounding vortex cores in $\text{Bi}_2\text{Sr}_2\text{CaCu}_2\text{O}_{8+\delta}$* , Science **295**, 466 (2002).
- [72] J. Stremper, I. Zegkinoglou, U. Rütt, M.v. Zimmermann, C. Bernhard, C. T. Lin, Th. Wolf, and B. Keimer, *Oxygen superstructures throughout the phase diagram of $(\text{Y,Ca})\text{Ba}_2\text{Cu}_3\text{O}_{6+x}$* , Phys. Rev. Lett. **93**, 157007 (2004).
- [73] U. Zeitler, H. W. Schumacher, A. G. M. Jansen, R. J. Haug, *Magneto-resistance anisotropy in Si/SiGe in tilted magnetic fields: Experimental evidence for a stripe-phase formation*, Phys. Rev. Lett. **86**, 866 (2001).
- [74] B. Spivak, *Phase separation in the two-dimensional electron liquid in MOSFET's*, Phys. Rev. B **67**, 125205 (2003).
- [75] K. Kawasaki, in *Phase Transitions and Critical Phenomena*, Vol. 4, edited by C. Domb and M. S. Green, (Academic Press, London, U.K., 1972).
- [76] H. van Beijeren and L. S. Schulman, *Phase transitions in lattice-gas models far from equilibrium*, Phys. Rev. Lett. **53**, 806 (1984).
- [77] D. Frenkel and B. Smit, *Understanding Molecular Simulation*, (Academic Press, London, U.K., 2002).
- [78] P. J. Hoogerbrugge and J. M. V. A. Koelman, *Simulating microscopic hydrodynamics phenomena with dissipative particle dynamics*, Europhys. Lett. **19**, 155 (1992); *ibid*, *Dynamic simulation of hard sphere suspensions under steady shear*, Europhys. Lett. **21**, 363 (1993).
- [79] P. Español and P. B. Warren, *Statistical mechanics of dissipative particle dynamics*, Europhys. Lett. **30**, 191 (1995); P. Español, *Hydrodynamics from dissipative particle dynamics*, Phys. Rev. E **52**, 1734 (1995).
- [80] F. de los Santos, P. L. Garrido, and M. A. Muñoz, *Entropic contributions in Langevin equations for anisotropic driven systems*, Physica A **296**, 364 (2001).
- [81] A. Achahbar, P. L. Garrido, J. Marro, and M. A. Muñoz, *Is the particle current a relevant feature in driven lattice gases?*, Phys. Rev. Lett. **87**, 195702 (2001).

- [82] E. V. Albano and G. Saracco, *Dynamic behavior of anisotropic nonequilibrium driving lattice gases*, Phys. Rev. Lett. **88**, 145701 (2002); *ibid*, *Reply to comment on "Dynamic behavior of anisotropic nonequilibrium driving lattice gases"*, Phys. Rev. Lett. **92**, 029602 (2004).
- [83] K. Leung and J. L. Cardy, *Field theory of critical behavior in a driven diffusive system*, J. Stat. Phys. **44**, 567 (1986).
- [84] H. K. Janssen and B. Schmittmann, *Field theory of long time behaviour in driven diffusive systems*, Z. Phys. B **64**, 503 (1986).
- [85] R. K. P. Zia, L. B. Shaw, B. Schmittmann, and R. J. Aсталos, arXiv:cond-mat/9906376 v1 24 Jun 1999.
- [86] B. Schmittmann and R. K. P. Zia, *Driven diffusive systems: An introduction and recent developments*, Phys. Rep. **301**, 45 (1998).
- [87] F. J. Alexander, C. A. Laberge, J. L. Lebowitz, and R. K. P. Zia, *Monte Carlo studies of a driven lattice gas. I. Growth and asymmetry during phase segregation*, J. Stat. Phys. **82**, 1133 (1996).
- [88] M. P. Allen and D. J. Tildesley, *Computer Simulations of Liquids*, (Oxford University Press, Oxford, U.K., 1987).
- [89] B. Smit and D. Frenkel, *Vapor-liquid equilibria of the two-dimensional Lennard-Jones fluid(s)*, J. Chem. Phys. **94**, 5663 (1991).
- [90] J. L. Vallés and J. Marro, *Nonequilibrium phase transitions in stochastic lattice systems: Influence of the hopping rates*, J. Stat. Phys. **43**, 441 (1986).
- [91] A. Szolnoki and G. Szabó, *Influence of extended dynamics on phase transitions in a driven lattice gas*, Phys. Rev. E **65**, 047101 (2002).
- [92] A. D. Rutenberg and C. Yeung, *Triangular anisotropies in driven diffusive systems: Reconciliation of up and down*, Phys. Rev. E **60**, 2710 (1999).
- [93] R. Dickman, *First- and second-order phase transitions in a driven lattice gas with nearest-neighbor exclusion*, Phys. Rev. E **64**, 016124 (2001).
- [94] D. C. Mattis, *The Theory of Magnetism II: Thermodynamics and Statistical Mechanics*, (Springer, Berlin, Germany, 1995).
- [95] P. L. Garrido, J. L. Lebowitz, C. Maes, and H. Spohn, *Long-range correlations for conservative dynamics*, Phys. Rev. A **42**, 1954 (1990).
- [96] K.-T. Leung, *Finite-size scaling of driven diffusive systems: Theory and Monte Carlo studies*, Phys. Rev. Lett. **66**, 453 (1991).
- [97] J. S. Wang, *Anisotropic finite-size scaling analysis of a two-dimensional driven diffusive system*, J. Stat. Phys. **82**, 1409 (1996).

- [98] E. Praestgaard, H. Larsen, and R. K. P. Zia, *Finite-size scaling in a two-temperature lattice gas: A Monte Carlo study of critical properties*, Europhys. Lett. **25**, 447 (1994).
- [99] K. Binder and D. Stauffer, *Theory for the slowing down of the relaxation and spinodal decomposition of binary mixtures*, Phys. Rev. Lett. **33**, 1006 (1974).
- [100] P. C. Hohenberg and B. I. Halperin, *Theory of dynamic critical phenomena*, Rev. Mod. Phys. **49**, 435 (1977).
- [101] P. D. Siders, *Effects of field orientation on the driven lattice gas*, J. Stat. Phys. **119**, 861 (2005).
- [102] S. A. Kivelson, *How to detect fluctuating stripes in the high-temperature superconductors*, Rev. Mod. Phys. **75**, 1201 (2003).
- [103] P. I. Hurtado, J. Marro, P. L. Garrido, and E. V. Albano, *Kinetics of phase separation in the driven lattice gas: Self-similar pattern growth under anisotropic nonequilibrium conditions*, Phys. Rev. B **67**, 014206 (2003).
- [104] R. Yamamoto and X. C. Zeng, *Molecular dynamics study of a phase-separating fluid mixture under shear flow*, Phys. Rev. E **59**, 3223 (1999).
- [105] L. Berthier, *Phase separation in a homogeneous shear flow: Morphology, growth laws, and dynamic scaling*, Phys. Rev. E **63**, 051503 (2001).
- [106] K. Binder and P. Fratzl, in *Phase Transformations in Materials*, edited by G. Kostorz, (Wiley-VCH Verlag, Weinheim, Germany, 2001).
- [107] J. Marro, J. L. Lebowitz, and M. H. Kalos, *Computer simulation of the time evolution of a quenched model alloy in the nucleation region*, Phys. Rev. Lett. **43**, 282 (1979).
- [108] A. J. Bray, *Theory of phase-ordering kinetics*, Adv. Phys. **43**, 357 (1994).
- [109] E. Levine, Y. Kafri, and D. Mukamel, *Ordering dynamics of the driven lattice-gas model*, Phys. Rev. E **64**, 026105 (2001).
- [110] R. Toral and J. Marro, *Scaling of the excess energy in thermodynamically unstable solutions*, Phys. Rev. Lett. **54**, 1424 (1985).
- [111] S. Y. Huang, X. W. Zou, and Z. Z. Jin, *Early dynamics of the potential energy evolution in two-dimensional gas-liquid phase separation*, J. Phys.: Condens. Matter **13**, 7343 (2001).
- [112] J. Marro, R. Toral, and A. M. Zahra, *Time evolution of the excess energy in supersaturated solid solutions: Microcalorimetric experiments, computer simulations and theory*, J. Phys. C **18**, 1377 (1985).

- [113] W. Ostwald, *Z. Phys. Chem., Stoechiom. Verwandtschaftsl.* **37**, 385 (1901); I. Lifshitz and V. Slyozov, *J. Phys. Chem. Solids* **19**, 35 (1961); C. Wagner, *Z. Elektrochem.* **65**, 58 (1961).
- [114] T. Baumberger, F. Perrot, and D. Beysens, *Kinetics of nucleation and growth in a near-critical binary liquid mixture at rest and under a shear flow*, *Phys. Rev. A* **46**, 7636 (1992).
- [115] T. M. Squires and S. R. Quake, *Microfluidics: Fluid physics at the nanoliter scale*, *Rev. Mod. Phys.* **77**, 977 (2005).
- [116] F. Wegner, *Corrections to scaling laws*, *Phys. Rev. B* **5**, 4529 (1972).
- [117] R. R. Singh, K. S. Pitzer, J. J. de Pablo, and J. M. Pravsnitz, *Monte Carlo simulation of phase equilibria for the two-dimensional Lennard-Jones fluid in the Gibbs ensemble*, *J. Chem. Phys.* **92**, 5463 (1990).
- [118] A. Z. Panagiotopoulos, *Molecular simulation of phase coexistence: Finite-size effects and determination of critical parameters for two- and three-dimensional Lennard-Jones fluids*, *Int. J. Thermophys.* **15**, 1057 (1994).
- [119] K. J. Strandburg, *Two-dimensional melting*, *Rev. Mod. Phys.* **60**, 161 (1988).
- [120] C. S. Campbell, *Rapid granular flows*, *Annu. Rev. Fluid Mech.* **22**, 57 (1990).
- [121] L. P. Kadanoff, *Built upon sand: Theoretical ideas inspired by granular flows*, *Rev. Mod. Phys.* **71**, 435 (1999).
- [122] *Granular Gases*, edited by T. Pöschel and S. Luding, (Springer, Berlin, Germany, 2001).
- [123] *Granular Gas Dynamics*, edited by T. Pöschel and N. Brilliantov, (Springer, Berlin, Germany, 2001).
- [124] I. Goldhirsch, *Rapid granular flows*, *Annu. Rev. Fluid Mech.* **35**, 267, (2003).
- [125] T. S. Komatsu, S. Inagaki, N. Nakagawa, and S. Nasuno, *Creep motion in a granular pile exhibiting steady surface flow*, *Phys. Rev. Lett.* **86**, 1757 (2001); D. M. Mueth *et al.*, *Signatures of granular microstructure in dense shear flows*, *Nature* **406**, 385 (2000).
- [126] I. S. Aranson, *et al.*, *Electrostatically driven granular media: Phase transitions and coarsening*, *Phys. Rev. Lett.* **84**, 3306 (2000); I. S. Aranson, B. Meerson, P. V. Sasorov, and V. M. Vinokur, *Phase separation and coarsening in electrostatically driven granular media*, *Phys. Rev. Lett* **88**, 204301 (2002).

- [127] J. Li, I. S. Aranson, W.-K. Kwok, and L. S. Tsimring, *Periodic and disordered structures in a modulated gas-driven granular layer*, Phys. Rev. Lett. **90**, 134301 (2003).
- [128] E. Khain and B. Meerson, *Symmetry-breaking instability in a prototypical driven granular gas*, Phys. Rev. E **66**, 021306 (2002).
- [129] A. Kudrolli, M. Wolpert, and J. P. Gollub, *Cluster formation due to collisions in granular material*, Phys. Rev. Lett. **78**, 1383 (1997).
- [130] B. Meerson, T. Pöschel, and Y. Bromberg, *Close-packed floating clusters: Granular hydrodynamics beyond the freezing point?*, Phys. Rev. Lett. **91**, 024301 (2003).
- [131] R. D. Wildman, J. M. Hutley, and D. J. Parker, *Convection in highly fluidized three-dimensional granular beds*, Phys. Rev. Lett. **86**, 3304 (2001).
- [132] Y. Forterre and O. Pouliquen, *Longitudinal vortices in granular flows*, Phys. Rev. Lett. **86**, 5886 (2001).
- [133] L. S. Tsimring and I. S. Aranson, *Localized and cellular patterns in a vibrated granular layer*, Phys. Rev. Lett. **79**, 213 (1997).
- [134] E. C. Rericha, C. Bizon, M. D. Shattuck, and H. L. Swinney, *Shocks in supersonic sand*, Phys. Rev. Lett. **88**, 014302 (2001); J. Bougie, S. J. Moon, J. B. Swift, and H. L. Swinney, *Shocks in vertically oscillated granular layers*, Phys. Rev. E **66**, 051301 (2002).
- [135] J. T. Jenkins and M. W. Richman, *Kinetic theory for plane flows of a dense gas of identical, rough, inelastic, circular disks*, Phys. Fluids **28**, 3485 (1985).
- [136] M. Babić, *On the stability of rapid granular flows*, J. Fluid Mech. **254**, 127 (1993).
- [137] J. J. Brey and D. Cubero, in Ref. [122].
- [138] P. K. Haff, *Grain flow as a fluid-mechanical phenomenon*, J. Fluid Mech. **134**, 401 (1983).
- [139] M.-L. Tan and I. Goldhirsch, *Rapid granular flows as mesoscopic systems*, Phys. Rev. Lett. **81**, 3022 (1998).
- [140] N. Sela and I. Goldhirsch, *Hydrodynamic equations for rapid flows of smooth inelastic spheres, to Burnett order*, J. Fluid Mech. **361**, 41 (1998).
- [141] J. J. Brey, J. W. Dufty, C. S. Kim, and A. Santos, *Hydrodynamics for granular flow at low density*, Phys. Rev. E **58**, 4638 (1998).
- [142] J. F. Lutsko, *Transport properties of dense dissipative hard-sphere fluids for arbitrary energy loss models*, Phys. Rev. E **72**, 021306 (2005).

- [143] C. Bizon, M. D. Shattuck, J. B. Swift, and H. L. Swinney, *Transport coefficients for granular media from molecular dynamics simulations*, Phys. Rev. E **60**, 4340 (1999); R. Soto, J. Piasecki, and M. Mareschal, *Precollisional velocity correlations in a hard-disk fluid with dissipative collisions*, Phys. Rev. E **64**, 031306 (2001); T. Pöschel, N. Brilliantov, and T. Schwager, *Violation of the molecular chaos in dissipative gases*, Int. J. Mod. Phys. C **13**, 1263 (2003).
- [144] P. Chaikin, in *Soft and Fragile Matter. Nonequilibrium Dynamics, Metastability and Flow*, edited by M. E. Cates and M. R. Evans, (IOP, Bristol, U.K., 2000), p. 315.
- [145] T. Wainright, B. J. Alder, and D. M. Gass, *Decay of time correlations in two dimensions*, Phys. Rev. A **4**, 233 (1971).
- [146] R. García-Rojo, S. Luding, and J. Javier Brey, *Transport coefficients for dense hard-disk systems*, cond-mat/0511671 (2005).
- [147] P. C. Hohenberg and J. B. Swift, *Effects of additive noise at the onset of Rayleigh-Bénard convection*, Phys. Rev. A **46**, 4773 (1992), and references therein; G. Quentin and I. Rehberg, *Direct measurement of hydrodynamic fluctuations in a binary mixture*, Phys. Rev. Lett. **74**, 1578 (1995); M. Wu, G. Ahlers, and D. S. Cannel, *Thermally induced fluctuations below the onset of Rayleigh-Bénard convection*, Phys. Rev. Lett. **75**, 1743 (1995).
- [148] B. Meerson, T. Pöschel, P. V. Sasorov, and T. Schwager, *Giant fluctuations at a granular phase separation threshold*, Phys. Rev. E **69**, 021302 (2004).
- [149] L. D. Landau and E. M. Lifshitz, *Statistical Mechanics*, (Pergamon Press, Oxford, U.K., 1980).
- [150] J. J. Brey, A. Domínguez, M. I. García de Soria, and P. Maynar, *Mesoscopic theory of critical fluctuations in isolated granular gases*, Phys. Rev. Lett. **96**, 158002 (2006).
- [151] D. C. Rapaport, *The Art of Molecular Dynamics Simulation*, (Cambridge University Press, Cambridge, U.K., 1995).
- [152] Y. Du, H. Li, and L. P. Kadanoff, *Breakdown of hydrodynamics in a one-dimensional system of inelastic particles*, Phys. Rev. Lett. **74**, 1268 (1995).
- [153] S. E. Esipov and T. Pöschel, *The granular phase diagram*, J. Stat. Phys. **86**, 1385 (1997).
- [154] E. L. Grossman, T. Zhou, and E. Ben-Naim, *Towards granular hydrodynamics in two dimensions*, Phys. Rev. E **55**, 4200 (1997).
- [155] N. V. Brilliantov and T. Pöschel, *Kinetic Theory of Granular Gases*, (Oxford University Press, Oxford, U.K., 2004).

- [156] M. Argentina, M. G. Clerc, and R. Soto, *van der Waals-like transition in fluidized granular matter*, Phys. Rev. Lett. **89**, 044301 (2002).
- [157] E. Livne, B. Meerson, and P. V. Sasorov, *Symmetry breaking and coarsening of clusters in a prototypical driven granular gas*, Phys. Rev. E **66**, 050301(R) (2002).
- [158] J. J. Brey, M. J. Ruiz-Montero, F. Moreno, and R. García-Rojo, *Transversal inhomogeneities in dilute vibrofluidized granular fluids*, Phys. Rev. E **65**, 061302 (2002).
- [159] E. Livne, B. Meerson, and P. V. Sasorov, *Symmetry-breaking instability and strongly peaked periodic clustering states in a driven granular gas*, Phys. Rev. E **65**, 021302 (2002).
- [160] E. Khain, B. Meerson, and P. V. Sasorov, *Phase diagram of van der Waals-like phase separation in a driven granular gas*, Phys. Rev. E **70**, 051310 (2004).
- [161] A. Brahic, *Saturn's rings seen by Cassini: Discoveries, questions and new problems in Traffic and Granular Flows*, (Springer, Berlin, Germany, 2005), in press.
- [162] N. F. Carnahan and K. E. Starling, *Equation of state for nonattracting rigid spheres*, J. Chem. Phys. **51**, 635 (1969).
- [163] M. A. Hopkins and M. Y. Louge, *Inelastic microstructure in rapid granular flows of smooth disks*, Phys. Fluids A **3**, 47 (1991).
- [164] S. Luding, *Global equation of state of two-dimensional hard sphere systems*, Phys. Rev. E **63**, 042201 (2001).
- [165] C. N. Yang and T. D. Lee, *Statistical theory of equations of state and phase transitions, I. Theory of condensation*, Phys. Rev. **87**, 404 (1952); *ibid*, *Statistical theory of equations of state and phase transitions, II. Lattice gas and Ising model*, **87**, 410 (1952).
- [166] P. L. Garrido and M. A. Muñoz, *Continuum description for nonequilibrium competing dynamic models*, Phys. Rev. Lett. **75**, 1875 (1995).
- [167] N. J. A. Sloane, *The sphere packing problem*, Doc. Math. J. DMV 1-1000 (1998).

Resumen en Español

La naturaleza presenta una estructura jerárquica en niveles, con escalas temporales, espaciales y de energía que se extienden desde el mundo *microscópico* al *macroscópico*. Aunque pueda sorprendernos, a menudo es posible tratarlos de forma independiente, e.g., en el caso de gases moleculares. El nivel macroscópico, que no es sino el mundo percibido directamente por nuestros sentidos, se describe hidrodinámicamente. Esto es, es descrito por funciones *continuas* (o continuas a trozos) de sus coordenadas espaciales \mathbf{r} y del tiempo t (*campos hidrodinámicos*). Por consiguiente, las grandes y exitosas disciplinas de la física macroscópica, tales como la mecánica de fluidos, elasticidad, acústica, electromagnetismo, son teorías de campos. Estos campos están determinados por ecuaciones integro-diferenciales que involucran funciones, en principio desconocidas, de \mathbf{r} y t . En cambio, el nivel microscópico describe colecciones de un gran número de constituyentes, típicamente átomos, moléculas o entidades más complejas, los cuales interactúan los unos con los otros de acuerdo con ciertas fuerzas electro-mecánicas. Aunque generalmente, la evolución temporal de cada individuo está dada por las leyes de la mecánica cuántica, en muchas situaciones la aproximación clásica resulta ser excelente. La diferencia entre niveles macroscópico y microscópico es esencialmente relativa: el concepto clave es el número de cuerpos, no su tamaño³.

Si hay una clara separación entre microscópico y macroscópico, aún es posible introducir una nueva escala intermedia: el nivel de descripción *mesoscópico*. Ésta es una representación *gruesa*⁴ que tiene por objeto dar cuenta de la física de los modelos microscópicos a escalas temporales y espaciales más altas, y que, matemáticamente, está caracterizada por ecuaciones diferenciales en derivadas parciales estocásticas [1, 2]. Para ser exactos, la descripción mesoscópica de un sistema dado, cuya dinámica es, en promedio, gobernada por las leyes de evolución temporal macroscópica, es el resultado del recuento y acumulación de fluctuaciones microscópicas. Este enfoque nos facilita el estudio de las propiedades de variación lenta de los sistemas de muchos cuerpos y, por otra parte, conforma el fundamento teórico de los estudios más modernos de fenómenos críticos. Es común encontrar en la literatura trabajos que incluyen

³Por ejemplo, una galaxia es un objeto (macroscópico) compuesto por un gran número de estrellas (microscópicas); del mismo modo, una comunidad de seres vivos es considerada como un conjunto de individuos; un gas como conjunto de moléculas, etc.

⁴O “coarse-grain” (grano grueso) según fuentes bibliográficas en lengua inglesa.

en este nivel intermedio descripciones de teoría cinética de los gases, e.g., la ecuación de Boltzmann. Por ello, este nivel es a veces conocido como *cinético*⁵.

Estos tres niveles de descripción⁶ son, en principio, enfoques equivalentes de la misma realidad física. No obstante, las leyes y simetrías asociadas a cada nivel son tan diferentes entre sí que desde muy pronto surgió en la comunidad científica la necesidad de entender cómo se relacionan, o, dicho de otro modo, cómo las propiedades hidrodinámicas emergen en términos de la dinámica microscópica de los constituyentes subyacentes. Así se desarrolló la *Mecánica Estadística*, disciplina que proporciona esas relaciones. En efecto, la mecánica estadística establece como su propio objetivo el determinar el comportamiento macroscópico de la materia originada en el comportamiento colectivo de entidades (microscópicas) individuales. Algunos de los fenómenos que observamos a alto nivel son consecuencia de simples efectos sinérgicos de las acciones de los constituyentes, por ejemplo, la presión ejercida por un gas molecular en las paredes del recipiente que lo contiene o miles de luciérnagas centelleando al unísono, mientras que otros son ejemplos paradigmáticos de comportamiento colectivo emergente, e.g., el cambio de régimen laminar a flujo turbulento en fluidos o el millón de átomos que forman el programa de la vida: el ácido desoxirribonucleico o ADN. En estos últimos casos, el comportamiento de los constituyentes llega a ser singular y muy diferente del que tendría en ausencia del resto, dando lugar a un comportamiento sin homólogo directo en las propiedades o dinámica de los constituyentes.

El mayor logro de la mecánica estadística es la *Teoría de Colectividades* [3]. Ésta establece formalmente el nexo de unión entre las propiedades macroscópicas de sistemas *en equilibrio* y las leyes que gobiernan las interacciones a nivel microscópico entre partículas individuales. Se dice que un sistema dado se encuentra *en equilibrio* cuando está aislado, no presenta histéresis y se haya en un estado estacionario en el que todas sus propiedades macroscópicas permanecen fijas [4]. En tal caso, las propiedades macroscópicas son expresadas en términos de variables *termodinámicas*. En efecto, la termodinámica es, en este sentido, una descripción hidrodinámica que consiste en leyes y relaciones entre magnitudes termodinámicas, y cuya base teórica microscópica es la mecánica estadística. Desde el punto de vista matemático, la teoría de colectividades se ha axiomatizado por completo. Esto nos proporciona, al menos en principio, expresiones analíticas para estas relaciones termodinámicas, permitiendo obtener toda la información macroscópica relevante del sistema en cuestión⁷,

⁵Aunque ecuaciones diferenciales estocásticas y ecuaciones cinéticas puedan ser clasificadas en un mismo nivel, involucran diferentes escalas (mesoscópicas) tanto espaciales como temporales.

⁶Nos restringiremos a los niveles aquí descritos, aunque existen escalas hidrodinámicas aún más altas, e.g., el así llamado *tren de vórtices* de Karman.

⁷Una vez especificado el Hamiltoniano microscópico del sistema (llamémosle \mathcal{H}), la distribución “canónica” de probabilidad de estados estacionaria \mathcal{P} está dada en términos del factor de Boltzmann $\mathcal{P} = e^{-\mathcal{H}/k_B T}/Z$, donde Z es la función de partición, k_B es la constante de Boltzmann y T la temperatura. A partir de los adecuados promedios sobre ésta, los observables estacionarios pueden ser calculados. El resto de dificultades son “meramente” técnicas.



Figure D.4: La complejidad en la naturaleza se manifiesta a todas las escalas. Algunos ejemplos llamativos son los siguientes. Arriba izquierda: geometrías fractales en cuencas fluviales en El Yemen (fuente NASA). Arriba derecha: modelado eólico franjiforme en las *Great Sand Dunes National Monument*, EE.UU. (fotografiado por Bob Bauer). Abajo izquierda: tornado como un flujo geofísico en rotación. Abajo derecha: *oscilones* en suspensiones coloidales agitadas verticalmente [5].

por ejemplo, la energía libre, la ecuación de estado, la radiancia espectral, etc.

Por contra (¡y afortunadamente!), en la naturaleza los sistemas en equilibrio son la excepción (incluso una idealización) más que la regla: fenómenos *fuera del equilibrio* son, con creces, mucho más abundantes. Galaxias, seres humanos, reacciones químicas, flujos geofísicos, portadores de carga en dispositivos semiconductores, mercados financieros, tráfico en autopistas, por citar unos pocos, son sistemas de muchos cuerpos en condiciones de no-equilibrio⁸. Los sistemas fuera del equilibrio se caracterizan por no estar cerrados, es decir, por intercambiar energía, partículas y/o información con su entorno. En general, el estado de un sistema fuera del equilibrio no es determinado únicamente por ligaduras externas, sino que también depende de su historia (presentan histéresis). Esto da lugar a la enorme complejidad del mundo real, la cual surge a todos los niveles de descripción [6, 7, 8, 9, 10] y se manifiesta en formación de patrones, fractales, sincronización, caos, criticalidad auto-organizada, etc. Toda esta sorprendente y complicada fenomenología es comúnmente asociada a *inestabilidades*⁹, las

⁸Fuera del equilibrio se encuentra también cualquier sistema que se encuentre relajando hacia un estado de equilibrio. No obstante, en la mayoría de estas situaciones su dinámica puede comprenderse adecuadamente a partir de conceptos de equilibrio.

⁹Las inestabilidades presentes en sistemas lejos del equilibrio presentan similitudes a nivel

cuales se describen como cambios de fase [7, 11, 12, 13], bifurcaciones, sinergia, etc. con el propósito de conectar lo microscópico con las estructuras coherentes observadas a alto nivel.

Sin embargo, la mayoría de los estudios de sistemas fuera del equilibrio realizados hasta la fecha adoptan un punto de vista eminentemente fenomenológico (macroscópico). En general, poco se sabe del porqué de tales estructuras o de cómo esta complejidad emerge desde interacciones colectivas a nivel microscópico. Consecuentemente, no existe una teoría apropiada y el desarrollo de sólidos fundamentos matemáticos está sólo en sus primeros pasos comparado con el del equilibrio, donde la teoría de colectividades funciona con éxito.

Una diferencia fundamental entre mecánica estadística del equilibrio y del no-equilibrio es que, mientras en la primera la distribución de probabilidad de estados, de la cual se deriva toda la información macroscópica útil, es conocida, fuera del equilibrio es, a priori, desconocida. Uno debe encontrar una distribución de estados, en este caso dependiente del tiempo, la cual verifica una ecuación general de evolución, a saber, la *ecuación maestra* [1]. Los casos resolubles se limitan a unos pocos, y lo son sólo de forma aproximada. Únicamente es posible ofrecer un enfoque unificado para sistemas que se encuentran *no demasiado lejos*¹⁰ del equilibrio [14], donde el sistema puede ser tratado perturbativamente alrededor del estado del equilibrio empleando las técnicas clásicas de las *teorías de respuesta lineal*. En cualquier caso, nuestra atención se centra precisamente en sistemas lejos del equilibrio, donde tales enfoques dejan de tener utilidad.

En este contexto, el objeto principal de esta tesis reside en el estudio de inestabilidades —a diferentes niveles de descripción— en sistemas forzados, i.e., mantenidos lejos del equilibrio por un agente externo. Nos centraremos en dos importantes clases de sistemas, a saber, fluidos difusivos con arrastre y gases granulares vibrofluidificados.

La primera familia (fluidos difusivos con arrastre) incluye¹¹ sistemas que se encuentran acoplados a dos fuentes de energía constante, de tal modo que se establece un flujo estacionario de energía a través de aquéllos. Esta definición es ciertamente bastante amplia e incluye sistemas de muy diversa índole. Aquí nos restringiremos a sistemas que presentan una corriente de partículas (cuyo número es una magnitud conservada) a su través, anisotropías espaciales asociadas a la acción de un campo externo y en los cuales finalmente se alcanza un estado estacionario de no-equilibrio. Un ejemplo sencillo y prototípico podría

morfológico con las observadas en el equilibrio, descritas éstas de forma mecano-estadística. Por tanto, suelen referirse como *cambios de fase del no-equilibrio*, aunque los cambios de fase fuera del equilibrio, sin las restricciones de éste, son mucho más ricos desde un punto de vista fenomenológico.

¹⁰Como es de suponer, una definición precisa de “no demasiado lejos” es muy difícil de dar y depende en gran medida del sistema estudiado y debe darse *ad hoc*.

¹¹Aquí seguimos la definición dada por Schmittmann & Zia en Ref. [15].

ser el de una impedancia en un circuito eléctrico disipando a la atmósfera la energía suministrada por una batería. Pero incluso en ésta reducida clase de sistemas, la distribución estacionaria de probabilidad es desconocida¹².

La motivación fundamental subyacente tras estudio de fluidos difusivos con arrastre es la necesidad de desentrañar los ingredientes básicos del comportamiento observado en sistemas lejos del equilibrio. Por ello, es justificado, pertinente y necesario el estudio de modelos simplificados que capturen lo esencial del comportamiento microscópico que da lugar a las complicadas estructuras macroscópicas. Estos modelos son a menudo caricaturas de los sistemas reales en los cuales la dinámica de los constituyentes está dada por simples reglas estocásticas. Entre ellos, los *modelos reticulares* [11, 15, 16, 17, 18, 19, 20] han jugado un papel preponderante debido primordialmente al hecho de que, a veces, aportan resultados analíticos exactos y permiten aislar las características esenciales de un cierto sistema. Además, los modelos reticulares nos ayudan a ganar la intuición necesaria para desarrollar teorías y, desde un punto de vista experimental, su implementación en computadores resulta ser muy eficiente. Todo esto ha contribuido al desarrollo y aparición de numerosas y novedosas técnicas, incluyendo la *teoría estadística de campos* lejos del equilibrio. En concreto, modelos reticulares han modelado con éxito algunos aspectos esenciales de organismos con estructura social [21, 22, 23], formación de redes fluviales [24], propagación de epidemias [25], vidrios, circuitos eléctricos, enzimas [28], tráfico [26, 27, 29], coloides y espumas, mercados financieros [30], etc.

Los cambios de fase (de equilibrio) y los fenómenos críticos son actualmente bien entendidos, en muchos aspectos, gracias a la aplicación de los métodos del *grupo de renormalización* [33, 34] a modelos reticulares. El resultado primordial derivado del estudio de fenómenos críticos (en equilibrio, insistimos) es el concepto de *universalidad*: en las cercanías de los puntos críticos el comportamiento de sistemas dispares está determinado únicamente por ciertas características comunes básicas —dimensionalidad, el rango de las interacciones, simetrías, etc.— y no parece depender en gran medida del sistema concreto [33, 35, 36].

La pregunta de si este concepto es también aplicable a cambios de fase lejos del equilibrio está todavía lejos de ser respondida. Por ello, se espera que, al igual que para sistemas en equilibrio, los modelos reticulares jueguen también un importante papel aquí. Trataremos con detalle estos aspectos en el Capítulo 3, en el que estudiaremos un modelo reticular difusivo con arrastre, paradigma de cambios de fase anisotrópicos lejos del equilibrio. Sin embargo, es fácil imaginar que los modelos reticulares, comparados directamente con sistemas reales, presentan la desventaja de que son demasiado “crudos” o simplificados. Esto debe entenderse en el sentido de que los modelos reticulares no capturan todos los detalles, especialmente los morfológicos, del diagrama de fases. Discutiremos éste y otros problemas en el Capítulo 4, donde presentaremos un nuevo modelo más *realista* para simulación de fluidos anisotrópicos.

¹²Es necesario hacer notar que en la literatura estos sistemas son referidos como *sistemas* difusivos con arrastre en vez de *fluidos* difusivos con arrastre, denominación que adoptamos en esta tesis. Como explicaremos con cierto detalle en el Capítulo 3, reservamos aquella denominación para una descripción mesoscópica de campo medio.

La segunda clase de sistemas considerados en esta tesis versa acerca de *gases granulares agitados mecánicamente*. Un medio granular [37] es un conglomerado de muchas partículas de tamaño macroscópico, y por lo tanto, susceptible de ser modelados clásicamente. Hay ejemplos por doquier y se presentan a muy diferentes escalas: desde materiales polvoreados hasta nubes de polvo intergaláctico. Dentro de ese intervalo podemos encontrar arena, hormigón, cereales, flujos volcánicos, los anillos de Saturno y otros muchos ejemplos. Su importancia científica y tecnológica es indudable, con numerosas aplicaciones farmacéuticas, en la construcción e ingeniería civil, químicas, agrarias y alimentarias, y, a mayor escala, en procesos geológicos y astrofísicos. Además, su estudio está correlacionado con otras clases de sistemas como coloides, espumas y vidrios. Así pues la fenomenología mostrada por estos sistemas es amplísima, yendo desde unas pocas micras a miles de kilómetros: formación de patrones en granulados fluidificados [38, 39, 44], agregación [42, 43], flujos y bloqueos en silos y tolvas [45], avalanchas y deslizamientos [46], mezcla y segregación [47], convección [48, 49], erupciones [50, 51], por citar unos pocos. Por todo ello, su importancia está lejos de toda duda y la adecuada comprensión de sus propiedades no es sólo una necesidad industrial urgente, sino que también supone un reto importante para la física.

Puesto que los granos individuales tienen dimensiones macroscópicas, la fricción, deformación, ruptura y las pérdidas energéticas por colisión producen disipación de energía, esto es, la energía cinética es transferida continuamente al medio en forma de calor. Asimismo, la escala de energía típica para, por ejemplo, un grano de arroz de, digamos, longitud $l \approx 5\text{mm}$ y masa m es su energía potencial mgl , donde g es la aceleración gravitatoria. Es para tamaños de grano mucho más pequeños cuando otros tipos de interacción ganan en importancia¹³. De ahí que en los medios granulares, y a diferencia de gases moleculares, la temperatura T no juega ningún papel, es decir, $k_B T \ll mgl$. Los efectos dinámicos pesan más que cualquier tipo de consideraciones entrópicas [37] y, consecuentemente, argumentos mecano-estadísticos o termodinámicos resultan de poca utilidad. Además, dado que cualquier granulado está formado por un número finito de constituyentes¹⁴, frecuentemente el efecto de las fluctuaciones en observables macroscópicos es enorme y, por tanto, su estadística es dominada por los, así llamados, *eventos raros*. Otros efectos también importantes están relacionados con el fluido intersticial, como aire o agua, aunque en muchas situaciones y, en buena aproximación, puede ignorarse considerando únicamente las interacciones de grano con grano. En esta tesis (concretamente en la Parte II) nos restringiremos al estudio de sistemas granulares *secos*, donde la interacción entre partículas predomina sobre la interacción con el posible fluido intersticial.

Sin embargo, y a pesar de la dinámica clásica que los caracteriza, los medios

¹³En granos con $d \approx 0.1$ aparecen cargas electrostáticas superficiales, o para $d \approx 0.01$ los efectos magnéticos y de adhesión superficial comienzan a ser relevantes.

¹⁴A diferencia de gases moleculares, $N \ll N_A$ donde N es el número de partículas y N_A el número de Avogadro. No obstante, si N fuera lo suficientemente grande (a determinar *ad hoc*) aún sería posible emplear un tratamiento estadístico.

granulares se comportan de forma poco convencional: sus fases —sólida, líquida y gaseosa— ponen de manifiesto una compleja fenomenología de carácter colectivo que los distinguen fuertemente de sus homólogos moleculares. El resultado es una paupérrima comprensión de sus propiedades dinámicas y estadísticas. De hecho, desde un punto de vista teórico, sólo existen predicciones de carácter muy general y muchas cuestiones permanecen sin responder. Los sólidos granulares son altamente hysteréticos, muestran indeterminación de tensiones estáticas, y el entramado de granos da lugar a cadenas de fuerzas, tensiones y esfuerzos internos, bloqueos, estrés conducido, dilatación o compresión por cizalladura. Los líquidos son viscosos, presentan avalanchas, segregación por tamaños, bandas de cizalladura, formación de patrones. Los gases, los cuales sólo perduran con un continuo aporte de energía (por ejemplo, agitación mecánica¹⁵), son altamente compresibles y muestran agregados inhomogéneos, colapso inelástico en modelos computacionales, distribuciones de velocidad no maxwellianas, falta de separación entre escalas macroscópica y microscópica.

Toda esta fenomenología hace que resulte muy difícil enmarcarlos dentro de la clasificación tradicional de estados de agregación de la materia, dificultando considerablemente su estudio. En Capítulos 6 y 7 abordamos algunos problemas no resueltos y controversias, a saber: cuáles son las propiedades estadísticas de los medios granulares, cómo y bajo qué condiciones cambian de fase y cuáles son los modelos continuos óptimos y cuándo aplicarlos. Especialmente nos centramos en la descripción hidrodinámica de las inestabilidades de agregación heterogénea y ruptura espontánea de simetría en gases granulares fluidificados.

Perspectiva

A lo largo de esta tesis abordamos el estudio de estas dos familias de sistemas. Nuestro trabajo se divide en cuatro partes. En el Capítulo 1 se presenta una introducción general que describe el objeto principal de esta tesis. Los Capítulos 2, 3 y 4 conforman la Parte I, que está dedicada a *fluidos difusivos con arrastre*. La Parte II trata de *gases granulares* y reúne los Capítulos 5, 6 y 7. La Parte III está formada por los apéndices A, B, C y D. Finalmente la Parte IV cierra con un resumen y las principales conclusiones.

La primera parte comienza en el **Capítulo 2** presentando el Gas Reticular con Arrastre, conocido como *Driven Lattice Gas* [11, 15, 53] —modelo prototípico para el estudio de cambios de fase anisotrópicos lejos del equilibrio. Las partículas que lo forman se mueven en un retículo e interaccionan de acuerdo con ciertas reglas locales de carácter anisotrópico. Éstas inducen un flujo de partículas en una dirección de tal modo que, si las condiciones de contorno así lo permiten, se establece una corriente. Este modelo es considerado una simplificación de ciertos problemas de tráfico y fluidos. Presentamos algunas de sus ya conocidas propiedades y también controversias, así como los fundamentos de los métodos teóricos y computacionales empleados en los Capítulos 3 y 4.

¹⁵Se habla entonces de gases fluidificados o vibrofluidificados

Una de las preguntas que cabe plantearse sobre cualquier modelo físico es si el comportamiento que manifiesta es universal. En el **Capítulo 3** abordamos esta importante cuestión estudiando la segregación anisotrópica de fases en el modelo prototípico introducido en el Capítulo 2. El énfasis de nuestro estudio está puesto en la influencia de los detalles de la dinámica microscópica en el estado estacionario del no-equilibrio resultante, aunque también se presta cierta atención a aspectos cinéticos. En especial trataremos, tanto desde un punto de vista computacional como teórico, las similitudes y diferencias entre el *driven lattice gas* y otros modelos reticulares y no reticulares relacionados con aquél. La comparativa nos permite discutir ciertas propiedades excepcionales y poco realistas del modelo reticular original. Además, ponemos a prueba la validez de dos teorías mesoscópicas actuales que pretenden dar cuenta del comportamiento crítico de esta clase de sistemas.

En el **Capítulo 4** introducimos un novedoso modelo computacional de fluido no reticular y de no-equilibrio diseñado para el estudio de fenómenos anisotrópicos. Su dinámica e interacciones son más realistas que en, por ejemplo, el *driven lattice gas*. Se trata de un modelo muy accesible desde el punto de vista computacional, que exhibe una corriente neta de partículas y estructuras franjiformes a bajas temperaturas orientadas según la dirección de un campo externo, asemejándose a muchas situaciones reales. Describiremos tanto las propiedades cinéticas a tiempos cortos (nucleación) como las estacionarias del modelo; en especial nos centraremos en su diagrama de fases: identificamos y caracterizamos sus fases sólida (mono- y policristalina), líquida y gaseosa, todas ellas altamente anisotrópicas. El cálculo preciso de sus parámetros críticos nos lleva a discutir el papel de las simetrías en el modelado de fluidos fuera del equilibrio con teorías de campos y simulaciones. Además se esbozan algunas comparaciones con experimentos reales.

El **Capítulo 5** sirve de introducción a la Parte II de esta memoria; parte que es dedicada a los gases granulares agitados mecánicamente o vibrofluidificados. Perfilamos el estado del arte con respecto a la investigación en gases granulares. Concretamente discutiremos la aplicabilidad de las teorías hidrodinámicas al estudio de flujos granulares. También proporcionamos brevemente los ingredientes básicos de los modelos estudiados en los capítulos siguientes y los métodos de simulación.

En el **Capítulo 6** empleamos una descripción hidrodinámica granular para estudiar la fenomenología observada en un gas inelástico confinado en un recipiente anular sin gravedad. Nuestro principal propósito es caracterizar apropiadamente sus estados estacionarios (de no-equilibrio) y establecer de forma precisa un diagrama de fases mediante la descripción hidrodinámica y la computacional. Empleamos relaciones constitutivas de tipo Chapman-Enskog, derivadas éstas de primeros principios. Prestamos especial atención a las inestabilidades observadas, a saber, separación de fases, agregación heterogénea de partículas y

ruptura de simetría. Ésta última constituye una prueba precisa para modelos de flujos granulares y fomenta el estudio de formación de patrones lejos del equilibrio. Con este estudio pretendemos motivar experimentos en inestabilidades de separación de fases en gases granulares, que podrían ser fáciles de implementar en esta geometría. Hasta ahora este tipo de estudios ha empleado geometrías planas en vez de radiales.

El objeto del **Capítulo 7** es el estudio de hidrodinámica granular y fluctuaciones en un gas granular bidimensional a densidades elevadas, condición ésta que impide la aplicabilidad de descripciones hidrodinámicas derivadas de primeros principios. Estudiamos un modelo de discos rígidos cuasielásticos interactuando en un recipiente circular y ganando energía del contorno. Mediante enfriamiento por colisión entre partículas se forma en la región central un granulado de alta densidad, el cual se comporta como una *macropartícula*. Algunas características de esta macropartícula son bien descritas por la solución numérica de un conjunto de ecuaciones hidrostáticas granulares, las cuales hacen uso de relaciones constitutivas más fenomenológicas. Las predicciones hidrostáticas se comparan de forma excelente con simulaciones de *dinámica molecular por eventos*. Además desarrollamos una descripción mesoscópica (tipo Langevin) para la macropartícula, confinada por un potencial armónico de naturaleza hidrodinámica y forzada por un ruido blanco de número finito.

La Parte III está compuesta de cuatro apéndices: en el **Apéndice A** se compendian las propiedades más relevantes del *Gas Reticular* (o *Lattice Gas*¹⁶), el cual es el homólogo de equilibrio del *driven lattice gas* tratado en el Capítulo 3; en el **Apéndice B** introducimos un modelo cuyo propósito es caracterizar la estabilidad de la interfase en modelos reticulares con arrastre; **Apéndice C** detalla las derivaciones de teoría estadística de campos desarrolladas en el Capítulo 3 concernientes a ecuaciones de tipo Langevin; y finalmente en el **Apéndice D** proponemos un conjunto de relaciones constitutivas para la descripción hidrodinámica de gases granulares tridimensionales.

Finalmente, tras los apéndices, se incluye un amplio resumen (que adjuntamos a continuación) de las principales conclusiones, resaltando las contribuciones originales de ésta tesis y señalando las líneas maestras a seguir en trabajos futuros.

Conclusiones

Desafortunadamente, y a pesar de los muchos esfuerzos científicos realizados, la descripción mecano-estadística rigurosa de inestabilidades lejos del equilibrio sigue siendo esquivada. Los trabajos presentados en esta tesis suponen un nuevo

¹⁶Modelo de Ising conservado.

paso adelante para entender los cambios de fase lejos del equilibrio. En efecto, el estudio de *fluidos difusivos con arrastre y gases granulares vibrofluidizados*, aparte de su importancia tecnológica, ahonda en este aspecto y contribuye a la racionalización de los fenómenos del no-equilibrio. Se ha hecho especial énfasis en el estudio y caracterización de las inestabilidades —en la mayoría de los casos a distintos niveles de descripción, a saber, macroscópico, mesoscópico y microscópico— que tienen lugar en aquellos sistemas. Esta labor ha sido llevada a cabo empleando modernas y novedosas técnicas en el ámbito de la física estadística.

Capítulo 1. Se presenta una introducción que incluye una descripción general de los sistemas estudiados, su lugar en la física y en la técnica, fenomenología y problemática. Asimismo se resaltan las motivaciones y el objeto principal de esta tesis.

Capítulo 2. En este capítulo presentamos el modelo considerado hasta la fecha prototipo de fluido difusivo con arrastre: el Gas Reticular con Arrastre o *Driven Lattice Gas* (DLG). Repasamos tanto sus propiedades más relevantes como las más controvertidas. Asimismo, se proporcionaron las bases teóricas y computacionales necesarias para los subsiguientes estudios de los Capítulos 3 y 4; éstas son modernas técnicas computacionales y teorías estadísticas de campos.

Capítulo 3. Describimos simulaciones tipo *Monte Carlo* y desarrollos analíticos de teoría de campos que pretenden ilustrar cómo, a diferencia de lo que ocurre en equilibrio, ligeras modificaciones en la dinámica microscópica pueden influenciar, incluso cuantitativamente, tanto los estados estacionarios como la cinética de relajación. Con este propósito, se tomó como referencia el DLG introducido en el capítulo anterior. Presentamos modelos reticulares y no reticulares relativos al DLG en los cuales las partículas, al igual que en el DLG, interactúan de acuerdo con ciertas reglas locales anisotrópicas. Estas reglas facilitan el movimiento preferente en una dirección espacial, de tal modo que se establece una corriente a través del sistema si así lo permiten las condiciones de contorno. En concreto, se discutió las similitudes y diferencias entre el DLG y su “análogo” no-reticular, a saber, un modelo en el cual las coordenadas de las partículas varían de forma continua y en el que éstas interactúan entre sí con un potencial atractivo de tipo Lennard-Jones 12-6 (también conocido como potencial Weeks-Chandler-Andersen). La detallada comparación de la morfología observada nos llevó a considerar ciertas propiedades del DLG como poco realistas y excepcionales, a pesar de haber sido considerado prototípico. Concluimos:

- El modelo continuo no-reticular presenta, al igual que su análogo el DLG, una corriente neta no nula de partículas, una interfase fluido-vapor altamente anisotrópica (franjiforme) y un cambio de fase de segundo orden (continuo).
- Sin embargo, estos difieren en algunas propiedades de carácter esencial. Contrariamente a lo que ocurre en el DLG, su análogo no-reticular exhibe

una temperatura crítica que decrece con la intensidad del campo externo. Es más, a diferencia del DLG, no existe ningún cambio de fase en el límite de campo externo saturante. En lo concerniente a los procesos cinéticos de formación de estructuras macroscópicas u ordenación (nucleación), se observaron agregaciones de partículas con forma triangular apuntando en el sentido del campo externo, justamente al contrario que en el modelo discreto.

- Estas observaciones sugieren una falta de universalidad en el modelo reticular originario. Demostramos así que el comportamiento del DLG está condicionado en gran medida por la geometría del retículo. Éste es el agente que favorece la ordenación, y no el campo en sí mismo. Por tanto, la característica sorprendente y contraintuitiva de que en el DLG “el campo externo” eleva la temperatura crítica respecto a la del equilibrio no es sino un efecto geométrico o topológico y no dinámico.
- De aquí se deriva, en concreto, que el DLG no tiene un homólogo no-reticular (más “realista”) inmediato.
- Para profundizar en esta situación, se estudió el DLG bajo la acción de un campo externo saturante a la vez que se aumentó el rango de las interacciones a nuevos vecinos. El modelo resultante, definido como NDLG¹⁷, se asemeja más al del caso no-reticular: la temperatura crítica decrece con el campo y las anisotropías triangulares observadas en el proceso de nucleación a tiempos cortos se orientan en el sentido del campo.
- No obstante, mostramos que, aún ampliando el radio de interacción entre partículas, tanto el decaimiento potencial de las correlaciones espaciales como la criticalidad permanecen invariantes. Las primeras fueron monitorizadas por la función de correlación a dos cuerpos y por el factor de estructura, mientras que las propiedades críticas se determinaron empleando técnicas estándar de análisis de tamaño finito y corroboradas por la teoría mesoscópica de campos conocida como *anisotropic driven system* (ADS).
- Por consiguiente, al extender la dinámica en el DLG se modifica de forma esencial el diagrama de fases —el cual no puede ser determinado por crudos argumentos de simetrías— pero no las propiedades intrínsecas relacionadas con la naturaleza de no-equilibrio del fenómeno —como el decaimiento de las correlaciones.

Las conclusiones de este capítulo están complementadas apropiadamente por los resultados de criticalidad del modelo afín expuesto en el Capítulo 4. Una posible y recomendable continuación del trabajo desarrollado en éste capítulo es el estudio de la segregación de fases en el modelo NDLG desde el punto de vista de la teoría de campos empleando el enfoque de la teoría ADS. Otros problemas son

¹⁷DLG con interacción a *vecinos siguientes* o *next-nearest-neighbors* DLG.

el estudio detallado de la estabilidad de la interfase bajo campos intensos (véase Apéndice B) y la extensión de nuestros métodos a otros modelos reticulares como, por ejemplo al *Time Asymmetric Exclusion Process* (TASEP) [16, 57].

Capítulo 4. Puesto que, como fue demostrado en el capítulo anterior, el DLG es poco realista en ciertos aspectos esenciales, presentamos aquí un modelo novedoso y más realista de fluido con arrastre, ideal para el estudio de fenómenos anisotrópicos. Se trata de un modelo no-reticular lejos del equilibrio en el que las partículas, que interactúan entre sí vía un potencial tipo Lennard-Jones 12-6, son conducidas por la acción de un campo externo, cuya energía se disipa en un baño térmico. Estudiamos la cinética de separación de fases a tiempos cortos y sus diferentes fases estacionarias (altamente anisotrópicas), a saber, sólido (mono- y policristalino), líquido y gas. En concreto, describimos los procesos de nucleación, monitorizados por el exceso de energía, el cual da cuenta de la energía interfacial; las propiedades estructurales de las diferentes fases en el estado estacionario, caracterizadas por las funciones de distribución radial y azimutal y el grado de anisotropía; y propiedades de transporte. Elaboramos también una precisa estimación de la curva de coexistencia líquido-vapor y de los parámetros críticos asociados. Las principales conclusiones son:

- El modelo propuesto parece contener la física esencial y necesaria para resultar útil como un modelo prototípico destinado a describir fenómenos anisotrópicos observados en la naturaleza.
- Este modelo es más conveniente para propósitos simulacionales en fluidos con arrastre que otros, como, por ejemplo, simulaciones estándar de dinámica molecular, que son más costosas.
- El modelo es la extensión natural a casos anisotrópicos lejos del equilibrio del conocido fluido de Lennard-Jones, que describe acertadamente el comportamiento de gases reales como el Ar. En efecto, nuestro modelo se reduce a éste para campo cero. De otro modo, exhibe una corriente neta de partículas y estructuras macroscópicas franjeadas por debajo de un punto crítico.
- En cuanto a las propiedades cinéticas, y a pesar de la anisotropía inherente del modelo en las etapas tardías de la descomposición espinodal, la nucleación se produce por coagulación tipo Smoluchowski y agregación de Ostwald, las cuales son conocidas por describir los procesos de nucleación de fluidos reales en equilibrio.
- Inesperadamente, encontramos que el comportamiento crítico del modelo es consistente con la clase de universalidad de Ising (equilibrio), pero no con la del DLG. La principal razón de este aparente desacuerdo y de otros detallados en este capítulo, podría ser la falta de simetría partícula-hueco en el modelo Lennard-Jones con arrastre.

- De ahí inferimos que la discretización espacial puede cambiar de forma significativa no sólo las propiedades morfológicas y cinéticas sino también las propiedades críticas. Esto contrasta fuertemente con el concepto de universalidad en sistemas en equilibrio, donde el comportamiento de estos cerca de los puntos críticos es independiente de los detalles microscópicos.
- Finalmente, creemos que este modelo motivará nuevos experimentos de descomposición espinodal anisotrópica, además de nuevos trabajos teóricos. De hecho, nuestras observaciones, por ejemplo, en las propiedades estructurales y en las primeras etapas de la cinética de segregación de fases, son fácilmente accesibles por experimentos de espectroscopía y microcalorimétricos, respectivamente.

Muchas cuestiones quedan aún por desarrollar. Investigaciones adicionales, las cuales están siendo elaboradas actualmente, involucran estudios detallados de las propiedades interfaciales y de los efectos de tamaño finito. Otros problemas que sería conveniente abordar en un futuro son dilucidar de forma precisa el papel de la simetría hueco-partícula y de la forma del potencial de interacción en las propiedades críticas; analizar las etapas tardías del proceso de segregación de fases, ya estudiadas en otros sistemas en y fuera del equilibrio, [107, 108] y [103, 109], respectivamente; y estudiar, desde el punto de vista de la teoría de vidrios las características morfológicas y estructurales de las fases sólida y vidriática (sólido policristalino) que presenta nuestro modelo.

Capítulo 5. En éste capítulo proporcionamos la base adecuada para nuestro estudio de gases granulares desarrollada en los Capítulos 6 y 7. Discutimos algunas controversias, problemas abiertos y avances recientes en fluidos granulares, en particular, de la aplicabilidad de teorías hidrodinámicas. También presentamos los ingredientes básicos de los métodos computacionales implementados en los siguientes capítulos.

Capítulo 6. Se presentaron cálculos analíticos, además de simulaciones de dinámica molecular por eventos, para un granulado monodisperso confinado en un recipiente anular sin gravedad y forzado por una pared “termalizada”. Consideramos el límite cuasielástico en una descripción hidrodinámica que emplea coeficientes de transporte tipo Chapman-Enskog [135], derivables de primeros principios. Desarrollamos un estudio exhaustivo de las inestabilidades de agregación heterogénea de partículas, ruptura de simetría y separación de fases que aparecen en el modelo, y que nos permiten determinar con exactitud su diagrama de fases. Para comprobar y complementar las predicciones teóricas implementamos simulaciones de dinámica molecular por eventos para este sistema. Nuestro estudio nos lleva a desarrollar algunas consideraciones sobre la física de las inestabilidades que tienen lugar el modelo. De éste capítulo concluimos:

- El enfoque hidrostático quedó completamente determinado por tres parámetros adimensionales: el de disipación de energía, la fracción de área ocupada por los granos y la razón de aspecto del sistema.

- Nuestras simulaciones de dinámica molecular mostraron (más claramente para un número suficientemente elevado de partículas) la formación de estados agregados con simetría azimutal alejados de la pared térmica que fuerza al granulado. A pesar del (relativamente) escueto número de partículas empleado, estos estados anulares fueron descritos de forma precisa y para densidades moderadas por la solución numérica de las ecuaciones hidrostáticas propuestas, las cuales emplean relaciones constitutivas tipo Enskog.
- Mediante un análisis de estabilidad marginal se obtuvieron soluciones que bifurcan del estado más básico (el estado anular). Dicho de otro modo, estas soluciones predicen la ruptura espontánea de simetría de aquellos estados con simetría azimutal (inestables respecto de pequeñas perturbaciones), hecho que ocurre sólo en un determinado rango de parámetros. Determinamos las curvas de estabilidad marginal y las comparamos con las fronteras de la región espinodal (de compresibilidad negativa) del sistema.
- Se concluye que el mecanismo físico de la inestabilidad de separación de fases es la compresibilidad negativa del granulado en la dirección azimutal, causada por las pérdidas de energía en las colisiones. Matemáticamente, la separación de fases se manifiesta en la existencia de soluciones adicionales en cierta región del espacio de parámetros a la ecuación de densidad.
- También las simulaciones mostraron la existencia de separación de fases, predichas por la descripción hidrodinámica, pero enmascaradas por grandes fluctuaciones espacio-temporales. Midiendo la distribución de probabilidad para la amplitud del modo de fundamental del desarrollo de Fourier del espectro azimutal de la densidad de partículas, identificamos con claridad el cambio de estados simétricos a estados con separación de fases.
- Además encontramos que la región del espacio de parámetros asociada a la inestabilidad, predicha por la descripción hidrodinámica, se localiza dentro de la región de separación de fases observada en nuestras simulaciones. Esto implica la presencia de una región binodal (de coexistencia de fases) donde el estado anular es metaestable.
- Esperamos que las inestabilidades de agregación, ruptura de simetría y separación de fases sean fácilmente observables en experimentos. De hecho, el modelo aquí propuesto es experimentalmente accesible, de modo que podría motivar nuevos experimentos en estas inestabilidades si atraese la atención de la comunidad pertinente.

Es claro que la comparación de las predicciones de nuestra teoría y simulaciones con experimentos sería altamente interesante. Al proponer la geometría anular esperamos motivar estudios experimentales de estas inestabilidades que podrían resultar ventajosos en esta geometría. Un dispositivo experimental anular no

presenta paredes laterales (como en una geometría rectangular) y por tanto evitaría las innecesarias, e inevitables por otro lado, pérdidas por colisión con las partículas. Un posible experimento podría emplear esferas metálicas deslizando sobre una superficie cuasi-plana (ligeramente cóncava). La pared térmica podría ser implementada por un anillo ligeramente excéntrico (y quizás rugoso) rotando rápidamente. Igualmente interesante para estudios subsiguientes sería determinar la naturaleza de las soluciones que se bifurcan (¿sub- o supercríticamente?) del estado agregado con simetría azimutal. Otros estudios podrían explotar las similitudes entre la fenomenología observada en nuestro modelo y la de los anillos planetarios, en los cuales, también se observan inestabilidades de agregación y de ruptura de simetría, entre otras.

Capítulo 7. En este capítulo tratamos con hidrodinámica granular y fluctuaciones en un sencillo gas granular bidimensional donde, debido a densidades elevadas (y no a inelasticidad elevada), descripciones continuas basadas en primeros principios dejan de tener validez. Los enfoques hidrodinámicos fueron puestos a prueba en un caso extremo empleando simulaciones de dinámica molecular por eventos: cuando se forman agregados granulares cuya densidad es próxima al valor de empaquetamiento máximo (denominados macropartículas). El sistema modelo considerado está formado por discos rígidos inelásticos encerrados en un recipiente circular cuya pared está termalizada forzando al granulado y llevándolo lejos del equilibrio. Las principales conclusiones se resumen en:

- Simulaciones de dinámica molecular mostraron, a causa del enfriamiento por colisiones, un agregado fuertemente empaquetado de partículas, con una interfase cuasicircular abrupta, con fluctuaciones espaciales y aislado de la pared térmica por un gas muy diluido. La formación de la macropartícula requiere un cierto número de partículas y la transición, en función de la densidad, desde un estado (cuasi) homogéneo a la macropartícula es abrupta pero continua.
- Se resolvió numéricamente un conjunto de ecuaciones granulares hidrostáticas que emplean como relaciones constitutivas las fenomenológicas de Grossman *et al.* [154]. Encontramos que, en un amplio rango de parámetros, el ajuste —incluyendo la parte de máximo empaquetamiento— con la solución con simetría azimutal de las ecuaciones hidrostáticas es casi perfecto. También demostramos que, para el mismo sistema, el empleo de relaciones constitutivas tipo Enskog [135], derivables de primeros principios, no describe adecuadamente —mediante comparación directa con los resultados de simulación— la región de mayor densidad del granulado.
- Estos resultados, que están de acuerdo con resultados previos en geometrías planas con y sin gravedad, extienden la aplicabilidad de las relaciones constitutivas de Grossman *et al.* a coeficientes de restitución ligeramente menores y a geometrías no planas.
- Un análisis de estabilidad marginal demostró —independientemente de las relaciones constitutivas empleadas— que no hay soluciones estacionarias

que bifurquen linealmente de la de simetría azimutal, esto es, no hay estados que manifiesten ruptura de simetría alguna. Esto está de acuerdo con la persistencia de macropartículas circulares y cuasicirculares que se observan en nuestras simulaciones.

- Estudiamos, por primera vez, las fluctuaciones de las macropartículas, midiendo la distribución de probabilidad radial del centro de masas del sistema. Las fluctuaciones resultan ser gaussianas.
- Las fluctuaciones gaussianas observadas del centro de masas sugieren una descripción mesoscópica tipo Langevin en términos de una macropartícula confinada un potencial atractivo de naturaleza hidrodinámica y forzada por ruido de número finito —queremos decir que el agregado efectúa un movimiento browniano dentro del sistema. Se determinó la correspondiente ecuación de Langevin.
- En contra de lo que ocurre en sistemas en equilibrio —y en muchos lejos del equilibrio—, en los cuales la magnitud relativa de las fluctuaciones decrece al incrementar el número de partículas¹⁸, encontramos que las fluctuaciones persisten al incrementar el número de partículas.

Aún quedan algunos problemas en nuestro modelo circular. Una cuestión que debería ser tratada es si existen inestabilidades adicionales en este sistema modelo. Algo de intuición podría obtenerse, por ejemplo, mediante medidas de orden posicional y orientacional del agregado, siguiendo la analogía con la teoría KTHNY [119] para fusión o licuefacción en sistemas en equilibrio. Concretamente, éstas podrían llevarse a cabo monitorizando las respectivas funciones de correlación. Es posible que tanto una solución general dependiente del tiempo como un estudio de estabilidad no-lineal contribuyan a la búsqueda. Otros posibles trabajos futuros son el estudio de inestabilidades en modelos tridimensionales relacionados (en el Apéndice D se incluye una primera aproximación a este tema) y de la fenomenología mostrada por gases granulares polidispersos en este tipo de sistemas.

A pesar de que comúnmente los apéndices se relegan a un segundo plano, creemos que nuestros Apéndices B y D merecen sus propias conclusiones.

Apéndice B. Recordamos que en este apéndice presentamos un modelo difusivo y con arrastre cuyo propósito es comprender mejor el balance entre campo externo y baño térmico que ocurre en el DLG y en otros modelos relacionados (concretamente, los modelos reticulares estudiados en el Capítulo 3). Los principales resultados son:

- Estudiamos la estabilidad de la interfase (orientada según la dirección del campo) en el límite de campos saturantes, encontrando un cambio de fase

¹⁸Para un gas ideal en equilibrio: $\sigma \sim \mathcal{O}(N^{-1/2})$, donde σ es la magnitud relativa de las fluctuaciones y N es el número de partículas.

de segundo orden *geométrico* o *topológico* en función de la conectividad de los sitios del retículo. Para bajas conectividades existe orden, dominan los efectos térmicos y la interfase es estable, mientras que al incrementar la conectividad (por encima de un valor crítico) el orden desaparece, domina el campo externo y la interfase se vuelve inestable.

- Este cambio de fase *geométrico* confirma que el balance campo–temperatura no es tan sencillo como la dinámica microscópica sugiere, es decir, no es una mera superposición lineal de ambos. Este hecho es una manifestación clara de una dinámica colectiva emergente.
- Además se determinaron los parámetros críticos del cambio de fase.

Apéndice D. En este apéndice desarrollamos una serie de estudios teóricos para mostrar la existencia de inestabilidades de agregación y ruptura de simetría en flujos granulares tridimensionales. De hecho, se trata de una sencilla extensión a tres dimensiones de la geometría circular estudiada en el Capítulo 7. Así, el modelo es el de un gas de esferas rígidas colisionando inelásticamente en el interior de un cilindro cuya pared curva está termalizada. Para este estudio, se hizo necesario proponer un nuevo conjunto de relaciones constitutivas.

- Derivamos relaciones constitutivas para gases granulares tridimensionales empleando argumentos de *volumen libre* en la vecindad de la densidad de máximo empaquetamiento, y sugerimos una interpolación entre el límite de máxima densidad y las relaciones usuales en el límite diluido. Para ello nos basamos en la estrategia seguida por Grossman *et al.* [154] en dos dimensiones, que emplea técnicas de volumen excluido para determinar las relaciones constitutivas.
- Mediante los métodos desarrollados en los Capítulos 6 y 7 pronosticamos y caracterizamos las inestabilidades de agregación y ruptura de simetría en un recipiente cilíndrico. La presencia de esta última supone una gran diferencia con lo observado en el Capítulo 7, donde su homólogo bidimensional no presentaba ruptura de simetría alguna.

Publicaciones

Los estudios descritos en esta tesis han dado lugar a las siguientes publicaciones:

- Manuel Díez-Minguito, Pedro L. Garrido, and Joaquín Marro, *Lennard-Jones and lattice models of driven fluids*, Phys. Rev. E **72**, 026103 (2005).
- Joaquín Marro, Pedro L. Garrido, and Manuel Díez-Minguito, *Nonequilibrium anisotropic phases, nucleation and critical behavior in a driven Lennard-Jones fluid*, Phys. Rev. B **73**, 184115 (2006).
- Manuel Díez-Minguito, Pedro L. Garrido, and Joaquín Marro, *Lattice versus Lennard-Jones models with a net particle flow in Traffic and Granular Flows '05*, in press (Springer, Berlin, 2006).

- Baruch Meerson, Manuel Díez-Minguito, Thomas Schwager, and Thorsten Pöschel, *Close-packed granular clusters: hydrostatics and persistent Gaussian fluctuations*, submitted to Europhys. Lett. (2006)
- Manuel Díez-Minguito and Baruch Meerson, *Phase separation of a driven granular gas in annular geometry*, submitted to Phys. Rev. E (2006).
- Manuel Díez-Minguito, Pedro L. Garrido, Joaquín Marro, and Francisco de los Santos, *Driven two-dimensional Lennard-Jones fluid* in *Modeling Cooperative Behavior in the Social Sciences*, P. L. Garrido, J. Marro, M. A. Muñoz (eds.), AIP Conference Proceedings **779**, 199 (2005).
- Manuel Díez-Minguito, Pedro L. Garrido, Joaquín Marro, and Francisco de los Santos, *Simple computational Lennard-Jones fluid driven out-of-equilibrium*, in *XIII Congreso de Física Estadística' FISES'05*, Abstract Book (2005).
- Manuel Díez-Minguito, J. Marro, and P. L. Garrido, *On the similarities and differences between lattice and off-lattice models of driven fluids* in *Workshop on Complex Systems: New Trends and Expectations*, to be published in Euro. Phys. J.-Special Topics (2006).
- Manuel Díez-Minguito and Baruch Meerson, *Phase separation of a driven granular gas in annular geometry*, in *XIV Congreso de Física Estadística FISES'06*, Abstract Book (2006).

Los siguientes trabajos se encuentran en preparación:

- Manuel Díez-Minguito, A. Achahbar, Pedro L. Garrido, and Joaquín Marro, *Langevin-type description for the driven lattice gas with next-nearest-neighbor dynamics* (2006).
- Manuel Díez-Minguito and Thorsten Poeschel, *On the validity of global equations of state for driven granular gases* (2006).
- Manuel Díez-Minguito, Pedro L. Garrido, and Joaquín Marro, *Interfacial properties in a nonequilibrium microfluidic system* (2006).

Este trabajo ha sido financiado parcialmente por el Ministerio de Educación y Ciencia (MEC) de España y fondos FEDER (proyecto FIS2005-00791).

